Stony Brook University

A Multiscale Model of the Thick Ascending Limb

A Dissertation Presented

by

Aniel Nieves-González

to

The Graduate School

in partial fulfillment of the

Requirements for the degree of

Doctor of Philosophy

in

Applied Mathematics and Statistics

Stony Brook University

December 2010

Stony Brook University

The Graduate School

Aniel Nieves González

We, the dissertation committee for the above candidate for the

Doctor of Philosophy degree, hereby recommend

acceptance of this dissertation.

Dr. Leon C. Moore, Dissertation Advisor
Professor, Physiology & Biophysics

Dr. David Green, Dissertation Advisor
Assistant Professor, Applied Mathematics & Statistics

Dr. Robert Rizzo, Chairperson of Defense
Associate Professor, Applied Mathematics & Statistics

Dr. Wei Zhu
Professor, Applied Mathematics & Statistics

Dr. Chris Clausen
Associate Professor, Physiology & Biophysics

This dissertation is accepted by the Graduate School

Lawrence Martin
Dean of the Graduate School

Abstract of the Dissertation

A Multiscale Model of the Thick Ascending Limb

by

Aniel Nieves-González

Doctor of Philosophy

in

Applied Mathematics and Statistics

Stony Brook University

2010

A multiscale, cell-based mathematical model of the thick ascending limb (TAL) was implemented and used to estimate the efficiency of Na^+ transport along the TAL, to examine what determines transport efficiency, and to study the dynamical properties of the TAL. The TAL model consists of epithelial cell models that represent all major solutes and transport pathways. The model equations are based on mass conservation and electroneutrality constraints. Empirical descriptions of cell volume regulation (CVR), pH control, and tubuloglomerular feedback (TGF) system are implemented in the model. Transport efficiency was calculated as the ratio of total net Na^+ transport to transcellular Na^+ transport. The results show that: 1) Because the function of the TAL segment is to generate dilute tubular fluid, the transepithelial [Na^+] gradient that is created substantially reduces transport efficiency. This factor calls into question the widely-held notion that a substantial fraction of TAL Na^+ reabsorption occurs by passive paracellular diffusion secondary to apical membrane K^+ cycling. 2) CVR responses in individual autonomous TAL cells limits Na^+ transport by each cell such that the workload distribution along the TAL segment is sufficiently uniform to result in more efficient transport. In essence, a self-organization process that raises transport efficiency emerges from the CVR responses in the ensemble of TAL cells. 3) At the segmental level, the TGF system acts synergistically with the CVR mechanism to increase transport efficiency by regulating tubular fluid inflow such that the

outflow Na^+ and Cl^- concentrations are maintained well above the limiting static-head values where there is no net transport and zero efficiency. Further, TGF restrains tubular fluid inflow to levels that are consistent with the reabsorptive capacity of the TAL, thereby ensuring that the effluent is adequately dilute for the operation of the urine concentrating mechanism. 4) Together, the CVR responses and the regulation of TAL flow by TGF result in a quasi-uniform distribution of NaCl transport and an axial [Cl] gradient sufficiently steep to yield a TGF system gain consistent with experimental data. This suggests that TGF is a self-optimizing feedback system, in that it drives the TAL towards a state that ensures a high feedback gain. 5) The apical membrane cycling of NH_4^+ through K^+ channels, the NKCC2 transporter, and the NHE exchanger prevents luminal potassium depletion and substantially increases Na^+ uptake into the TAL cells. Without NH_4^+ cycling, the TAL model predicts that the dilutional capacity of the TAL will be severely compromised. 6) When TAL inflow oscillates, the TAL segment acts as a nonlinear low-pass filter with a characteristic harmonic structure that reflects the establishment of standing waves of Na^+ and Cl^- in the lumen of the TAL. This finding is consistent with both earlier modeling efforts and experimental data. In addition, the TAL cells themselves are predicted to act as multi-input/multi-output nonlinear filters. 7) When the TGF system is active and its gain exceeds a critical value, limit cycle oscillations in tubular fluid flow emerge, a behavior that is consistent with experimental observations.

Contents

List of Tables

List of Figures

Acknowledgments

The list of people that I would like to acknowledge is extensive. Hence, rather than enumerating them I will just say thanks to my family and friends.

Chapter 1

Introduction and background

The kidneys play a major role in regulating body content of sodium, potassium, chloride, and other electrolytes, the plasma concentrations of which must be kept within ranges compatible with life. Also, the kidney is a long term regulator of body fluid pH, and has endocrine functions like secretion of erythropoietin, which controls red blood cell production, secretion of renin, which triggers a cascade of biochemical events that ends up increasing circulating levels of angiotensin II, a powerful vasoconstrictor, and aldosterone, which regulates renal sodium excretion. The removal of metabolic end products is also an important kidney function. Last but not least is the role of the kidney in water balance, in that the kidneys retain or excrete water as needed to maintain constant body fluid osmolarity. Due to its role in water and sodium balance, the kidney plays an important part in the mechanism for regulation of extracellular volume and, therefore, blood pressure. In that regard the ADH (antidiuretic hormone), which is secreted by the posterior pituitary gland, signals

the kidney to retain water, while aldosterone and atrial natriuretic peptide signal the kidney to either conserve or excrete Na^+. One of the consequences of water and sodium retention is increased blood pressure, while the effect of enhanced water and sodium excretion is reduced blood pressure.

The functional unit of the kidney is the nephron (see Figure 1.1), in that the nephron is the smallest anatomical unit that performs the four main kidney processes: filtration, reabsorption, secretion, and excretion. Each human kidney has about a million nephrons each of which is in close contact with a network of capillaries that take up solutes and water transported by the epithelial cells that form the wall of the tubular portion of the nephron. The composition of the renal interstitium is influenced by the process of tubular reabsorption, especially in the medulla where the interstitial osmolarity is much higher than in plasma.

The nephrons have different lengths, and can be subdivided into segments with distinct differences in function. For illustrative purposes observe Figure 1.1 and imagine a fluid particle in the blood vessel (afferent arteriole) just about to enter the nephron. The interface of nephron's lumen and blood vessels is called the glomerulus. It is enclosed by the Bowmans capsule, and is the place where filtration occurs. The physical structures of the capillary wall in the glomerulus prevent the passage of red blood cells and plasma proteins like albumin, while small solutes and water are driven into the nephrons lumen by the high hydrostatic pressure in the capillaries. Once the fluid particle is inside the lumen (there it is called filtrate), the first segment it encounters is the proximal convoluted tubule (PCT) which is responsible for reabsorbing the majority of the filtrate. In this segment,

there is avid reabsorption of essential substances that must be conserved, including Na^+ and glucose (via the Na^+-Glucose transporter) and amino acids. The PCT also plays an important role in pH control, by secreting H^+ via the sodium-hydrogen exchanger (NHE), recovering filtered bicarbonate, and producing ammonia which buffers secreted protons. After exiting the PCT, the fluid particle enters the Loop of Henle which has two parts with

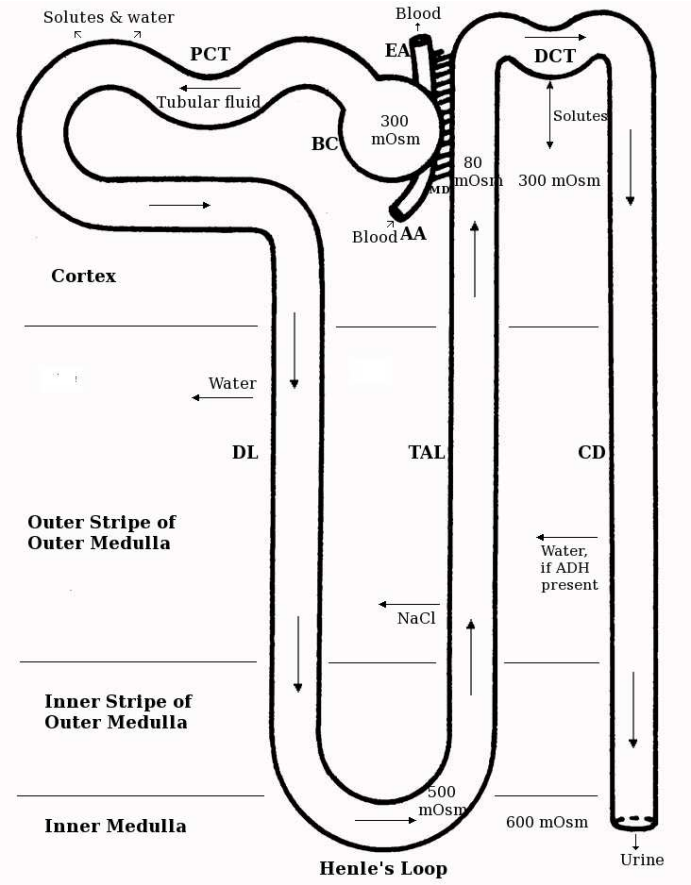

Figure 1.1: Nephron schematic

different functions. The descending limb (DL) is the site of osmotic water reabsorption driven by the high osmolarity of the medullary interstitium. In contrast, the ascending part or thick ascending limb (TAL) is impermeable to water but is a major site for Na^+ and Cl^- reabsorption. The TAL, which is the focus of this work, is able to reduce the osmolarity

of the filtrate from 300 to $\sim$70 mOsm by a transport process that involves the Na^+-$2Cl^-$-K^+ (NKCC2) cotransporter. This segment also transduces changes in tubular fluid flow rate into changes in outflow ionic composition that are sensed by specialized cells (macula densa, MD) at the end of the TAL that trigger adjustments in nephron blood flow. This important reflex is termed tubuloglomerular feedback (see below). Through tubular fluid dilution, the TAL establishes an osmolarity gradient in the interstitial fluid that drives osmotic water transport from the collecting ducts, and this permits the kidney to retain water by excreting highly concentrated urine.

Once the filtrate exits the TAL, it enters the distal convoluted tube (DCT). In this segment, as well as in the collecting ducts, there is hormone dependent Na^+ reabsorption and K^+ secretion (controlled by aldosterone), variable water reabsorption (controlled by ADH), and fine pH regulation. Finally, the tubular fluid enters the collecting duct (CD) which is also involved in pH regulation and, importantly, in water reabsorption. Cells in the CD are directly affected by ADH, in that in its presence, water channels (aquaporins) are inserted into the apical membrane of CD cells leading to enhanced osmotic water reabsorption. The osmosis is driven by the hyperosmolarity of the interstitial space, which was built up by the Na^+ and Cl^- reabsorption in the TAL. It is important not to lose sight of the fact that in the medulla, the nephrons and blood vessels that surround them (vasa recta) form an intricate system in which solutes and water are exchanged between them by means of a countercurrent mechanism. This mechanism is crucial since it not only allows the delivery of nutrients to cells along the nephron but also prevents the osmolarity gradient in the medullary interstitial fluid from being washed away by water reabsorption and vasa recta

blood flow.

The focus of this work is the TAL segment of the nephron, and our interest is examining how different systems both at the cellular level, like cell volume regulation (CVR), and at the segmental level, like the tubuloglomerular feedback system (TGF), act in concert such that workload is distributed quasi-uniformly along the TAL. We define an efficiency index as the ratio of total transepithelial to transcellular Na^+ transport, and use that index to show the relative efficiency of solute transport along the TAL and how CVR and other properties of individual cells affect that efficiency. A cell-based model of the TAL segment is developed and used to elucidate the inner workings in such a segment. The term cell-based model means that the tubule walls of the segment are represented by epithelial cell models rather than by a single barrier. This permits us to include a detailed representation of the transport processes that are characteristic of TAL cells, as well as of important subsystems like CVR or pH regulation, that make it possible for a TAL cell to maintain homeostasis even in under the harsh conditions that characterize some regions of the kidney (see below).

Other investigators have modeled TAL cells as well as different segments of the nephron, including models of the proximal convoluted tubule used to study its water and electrolyte reabsorption properties [1, 2], and models of the distal nephron (i.e. distal convoluted tubule and collecting duct) [3, 4, 5, 6]. These models have been used to study the function of various cotransporters, including those associated with acid/base, and cell volume regulation. For the TAL, Fernandes and Ferreira [7] implemented a cortical TAL cell model based on the experimental work of Greger and coworkers [8]. For use in studies of the TGF system, Layton and coworkers have developed a minimal model of the TAL where only one

solute is included and the wall of the TAL segment is represented as a single barrier with a passive permeability and active transport with Michaelis-Menten-like kinetics [9]. Recently, Weinstein [10, 11] presented a model for TAL epithelium as well as tubule models for medullary and cortical TAL tubules. This was done with the purpose of elucidating how the presence of NH_4^+ affects solute transport in the TAL, which is particularly important due to the significant concentrations of NH_4^+ in the luminal and serosal compartments and to the complicated and intertwined transport pathways that couple NH_4^+ and other solutes, in particular Na^+ and K^+. One such pathway involves the cycling of ammonium in the luminal side, that is, NH_4^+ uptake through the NKCC2 and extrusion via NHE. Weinstein also used his model to try to capture the pathophysiolgy associated with transport defects in the TAL. Of particular interest was Bartter's syndrome, which refers to a number of salt wasting diseases caused by genetic defect in a number of key transport proteins, including the NKCC2 transporter [12].

The fundamental differences between the work presented here and the above mentioned TAL modeling studies are as follows: first, the implementation of a detailed cell-based TAL model coupled with a TGF model; second, the implementation of a cell volume regulation mechanism that controls solute transport, and therefore short-term cell volume changes by regulating the activities of the NKCC2 and KCC4 membrane transporters; third, the focus on transport efficiency and how it is linked to cell volume regulation, a property of individual cells, and to TGF, a feature of the nephron as a whole. In general, this is a complex and detailed work in which a truly multiscale model is developed and used to explore the function of a segment of the nephron whose inner workings are not completely

known. The main difficulty encountered in the course of working on this project are the sparse data sets owing to the inacessibility of the TAL in vivo, and the nonhomogeneity of the TAL cells because their environment is very different between cortex and inner medulla.

1.1 Specific Aims

The overall goal of the project is to construct and implement a model for the thick ascending limb (TAL) at the cellular level. The model must include not only the membrane transporters that characterize a TAL cell, but also some of the signaling elements that regulate the behavior of key transport proteins in the cell. We will employ inverse methods and direct simulations to test the hypothesis that the tubuloglomerular feedback (TGF) system and cell volume regulation responses act in concert to distribute the reabsorptive work among all of the individual TAL cells; that this ensures efficient TAL energy utilization at a rate that avoids ischemia; and establish an axial Cl concentration gradient along the length of the TAL, a variable that is a key determinant of the gain of the TGF system. Together, these actions will demonstrate that the TGF is self optimizing, in that maintains an optimal balance of system gain, energy usage, and TAL salt reabsorption. The specific aims are:

1. To use inverse problem formulations to optimize medullary TAL (mTAL) and cortical TAL (cTAL) cell transport consistent with published experimental measurements of fluxes in vivo and in vitro, and dilutional ability in vivo.

2. To characterize the relationship between luminal ion concentrations and mTAL and cTAL cell energy consumption to estimate the marginal energy costs of tubular fluid

dilution (ATP utilization per mOsm additional dilution) over a range of interstitial ion concentrations typical of the outer medulla and cortex. The effects of TAL cell volume regulation on energy consumption and transport will be investigated, as will changes in NKCC2 function in water diuresis.

3. To test the hypothesis that TGF regulates TAL flow such that the work load presented to the TAL cells is consistent with efficient energy utilization, and that this coincides with the establishment of a concentration gradient within the TAL sufficient to account for the measured gain of the TGF system.

4. To investigate the dynamic properties of the TAL, which often is forced by periodic oscillations in fluid inflow when the TGF system becomes unstable.

These studies will provide new insights into the TGF system, TAL transport and energy consumption, and the how to formulate inverse problems to study renal tubular function.

1.2 Background

Sodium transport in the thick ascending limb (TAL) is an important determinant of renal sodium excretion and is essential for elaboration of hypertonic and hypotonic urine. This segment also plays a key role in renal autoregulation through its involvement in the tubuloglomerular feedback (TGF) system. In this context, the TAL transduces variations in tubular fluid flow into changes in ion concentration that are sensed by the macula densa (MD) cells. TGF is an intra-nephron reflex that acts to balance the load of

fluid filtered at the glomerulus with the reabsorptive capacity of the nephron [13]. The sensed signal is a flow dependent rise in [Na^+] and [Cl^-] of the effluent of the TAL. The sensors are macula densa cells, which are located at the end of the TAL segment, and are the initiators of an adenosine-mediated constriction of the afferent arteriole [14, 15]. The steady-state characteristics of the TGF system are illustrated in Figure 1.2. In some respects, TGF is a typical negative-feedback regulator where the response, a reduction in nephron glomerular filtration rate (GFR), is proportional to the perturbation in nephron flow, but in this case the feedback response also shows both threshold and saturation nonlinearities. The TGF system indirectly regulates TAL NaCl reabsorption. TGF senses deviations from the normal low NaCl levels in the TAL effluent, and readjusts nephron filtration rate and, hence, the load of NaCl entering the TAL to a rate appropriate for its reabsorptive capacity. Regulation of TAL NaCl load is important because TAL transport capacity is metabolically limited by low rates of medullary blood flow [16]. By limiting the TAL workload, TGF both prevents local ischemia and ensures appropriate tubular fluid dilution. Figure 1.2 panel B shows that the TAL does not maximally reduce tubular fluid (TF) [Na^+]. Rather, at its normal operating point, the TGF system regulates

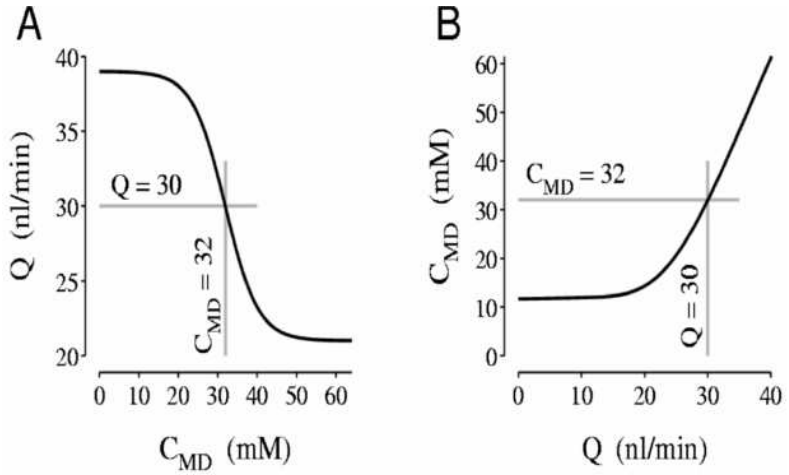

Figure 1.2: (A) Feedback function: effect of MD [Cl^-] (C_{MD}) on nephron glomerular filtration rate (Q). The gray lines show values for a typical operating point. (B) Tubular function: this relationship generates the sensed error signal. Curves are from modeling studies in [9], and used with permission of the Am Physiol Soc.

outflow TF [Na^+] to a level near the point at which the slope of the curve of concentration as function of flow goes to zero because of Na^+ back leak (flux toward the lumen). As further dilution below this level requires a marked increase in energy consumption by the TAL cells, TGF appears to regulate outflow [Na^+] at a level appropriate for effective urine concentration and dilution without undue energy expenditure by the cortical TAL cells. It is interesting that the TGF operating point has been found to be where the relationship between TAL outflow [Na^+] and tubular fluid flow has a high slope, which results in a high open-loop gain for the TGF system [17]. If the system operating point were located further down on the curve where net Na^+ backleak is higher, energy would be wasted in the just maintaining the transepithelial concentration gradient. These observations are the basis of the hypothesis that interactions between the TGF system and the TAL may optimize energy utilization by the TAL cells and maintain TGF system gain at a high level.

TAL cells are thought to be capable of high-efficiency Na^+ reabsorption. In the most basic, textbook model of TAL cell transport [18], apical Na^+ uptake is principally mediated by the electroneutral NKCC2 cotransporter which moves one K^+, one Na^+, and two Cl^- ions into the cell. Back diffusion of K^+ through apical K^+ channels produces a lumen positive transepithelial potential, which drives passive Na^+ reabsorption through cation-permeable tight junctions. The net result is that ATP utilization is substantially lower than what would be required if both Na^+ ions were reabsorbed transcellularly. However, several factors greatly complicate, or perhaps impair this attractive scheme.

First, NH_4^+ is taken up by the NKCC transporter, and can permeate K^+ channels and the TAL tight junctions [19, 20, 21]. While substantial amounts of NH_4^+ are reabsorbed into

the outer medullary interstitium, there is also significant NH_4^+ secretion by the sodium-hydrogen exchanger (NHE) [22, 23] which increases transcellular Na^+ transport. Hence, while NH_4^+ cycling [10] will facilitate TAL cell Na^+ transport, it does so at the cost of increased energy expenditure and a pH perturbation challenge.

Second, TAL luminal Na^+ concentration varies from $\sim$250-300 mM at the bend of Henle's loop, to $\sim$25 mM at the end of the cortical TAL (cTAL) [24, 25, 26]. While energy usage in cTAL cells may be regulated by TGF (see above) such that energy is not wasted on futile Na^+ cycling, the medullary TAL (mTAL) cells face the problem of balancing apical Na^+ uptake with the basolateral Na^+ transport capacity, which may be metabolically limited by the low rates of blood flow in the outer medulla [16]. Recent evidence in non-epithelial cells and non-renal secretory epithelial cells indicates that, in such cells, reciprocal regulation of NKCC1 (a KCl loading pathway) and the potassium chloride cotransporter (KCC) (a KCl exit pathway) stabilizes cell volume and intracellular chloride, and is mediated by a Cl^- sensitive signaling pathway that likely involves WNK (With No K with K referring to lysine) and Ste20-type serine/threonine kinases [27, 28]. This mechanism may also mediate apical/basolateral balancing in mTAL cells, as WNK-3 has been shown to enhance phosphorylation of the renal NKCC2 isoforms [29]. Regardless of the mechanism, apical/basolateral flux balancing permits TAL cells to adapt to variations in local availability of metabolic substrates and luminal ion concentrations. This would not only protect the cells from ischemia, but also distribute the reabsorptive workload along the length of the TAL, an effect that is needed to generate an axial tubular fluid gradient in Na^+ concentration along the length of the TAL. There is indirect evidence that such a

gradient is present. The well-known flow dependency of TAL effluent [Na^+] (see Figure 1.2B) requires an axial TAL concentration gradient, and the gain of the TGF system is strongly influenced by the magnitude of the gradient [17].

Third, another factor that influences TAL cell function is the differential expression of three different isoforms of the NKCC2 transporter (A-, B-, and F-isoforms). These three isoform exhibit marked differences in Cl^- binding affinity (B>A>F) and the pattern of expression along the TAL is such that the F isoform predominates in the inner stripe of the outer medulla, A is found in outer stripe of the outer medulla and cortex, while the B isoform is localized in the distal cTAL and macula densa where tubular fluid [Cl^-] is the lowest [30, 31].

Fourth, mouse TAL cells also express splice variants of the NKCC2 isoforms, and there is evidence that they can function as K^+-independent NaCl co-transporters [32, 33, 34]. These shorter isoforms are inhibited by cAMP, activated by hypoosmolarity, and exert a dominant negative effect on the full length NKCC2 protein. These observations lead Plata et al. [34] to suggest that the stochiometry of TAL apical Na^+ uptake switches between K^+, Na^+, $2Cl^-$ in antidiuresis and Na^+, Cl^- during water diuresis. If so, this could have a major impact of TAL cell workload, as it would greatly increase transcellular sodium flux. However, it is known that TAL reabsorption is reduced in the absence of ADH, but whether this could fully mitigate the effects of the mode switching is unknown at present.

Finally, the TGF system has long time delays and a gain that is sufficently high to trigger limit cycle oscillations. When this occurs, the fluid inflow into the TAL is oscillatory.

It is not known how such periodic flow, which leads to oscillations in tubular fluid ion concentrations, influences TAL cell Na^+ transport.

The above illustrates that the TAL is a complex dynamic structure that consists of cells that are capable of independent regulation of their reabsorptive rate. We had implemented a model of a TAL cell, and began to study the effects of NH_4^+ on cTAL Na^+ transport. One of the major difficulties in the evaluation of such models is that there are scores of parameters that must be specified, many of which are unknown. This is why we include an inverse problem formulation in our studies of TAL cell model, which provides a systematic way to obtain parameter sets consistent with known behaviors and measured data. These studies provide new insight into the function of TAL cells, how these are regulated by the TGF system, and what factors determine energy usage by the TAL.

1.3 Key findings

The major results of this modeling study are:

1. Because the function of the TAL segment is to generate dilute tubular fluid, the transepithelial [Na^+] gradient that is created substantially reduces transport efficiency. This factor calls into question the widely-held notion that a substantial fraction of TAL Na^+ reabsorption occurs by passive paracellular diffusion secondary to apical membrane K^+ cycling.

2. CVR responses in individual autonomous TAL cells limits Na^+ transport by each cell such that the workload distribution along the TAL segment is sufficiently uniform to result in more efficient transport. In essence, a self-organization process that raises transport efficiency emerges from the CVR responses in the ensemble of TAL cells.

3. At the segmental level, the TGF system acts synergistically with the CVR mechanism to increase transport efficiency by regulating tubular fluid inflow such that the outflow Na^+ and Cl^- concentrations are maintained well above the limiting static-head values where there is no net transport and zero efficiency. Further, TGF restrains tubular fluid inflow to levels that are consistent with the reabsorptive capacity of the TAL, thereby ensuring that the effluent is adequately dilute for the operation of the urine concentrating mechanism.

4. Together, the CVR responses and the regulation of TAL flow by TGF result in a quasi-uniform distribution of NaCl transport and an axial [Cl] gradient sufficiently steep to yield a TGF system gain consistent with experimental data. This suggests that TGF is a self-optimizing feedback system, in that it drives the TAL towards a state that ensures a high feedback gain.

5. The apical membrane cycling of NH_4^+ through K^+ channels, the NKCC2 transporter, and the NHE exchanger prevents luminal potassium depletion and substantially increases Na^+ uptake into the TAL cells. Without NH_4^+ cycling, the TAL model predicts that the dilutional capacity of the TAL will be severely compromised.

6. When TAL inflow oscillates, the TAL segment acts as a nonlinear low-pass filter with

a characteristic harmonic structure that reflects the establishment of standing waves of Na^+ and Cl^- in the lumen of the TAL. This finding is consistent with both earlier modeling efforts and experimental data. In addition, the TAL cells themselves are predicted to act as multi-input/multi-output nonlinear filters.

7. When the TGF system is active and its gain exceeds a critical value, limit cycle oscillations in tubular fluid flow emerge, a behavior that is consistent with experimental observations.

Chapter 2

Mathematical model and methods

The cell-based model of the thick ascending limb (TAL) consists of an ensemble of N cells that make up the walls of the TAL tubule (see Figure 2.1). Mathematically, it is a system of partial differential equations (PDE) in which the time evolution of cell volume, cytosolic, and luminal concentrations at different locations along the tubule axis are tracked. The solutes tracked are Na^+, K^+, Cl^-, X^-, Y, Z^+, H^+, NH_4^+, NH_3, H_2CO_3, HCO_3^-, $H_2PO_4^-$, and HPO_4^{2-}, where X^-, Y, Z^+ represent charged and uncharged impermeants.

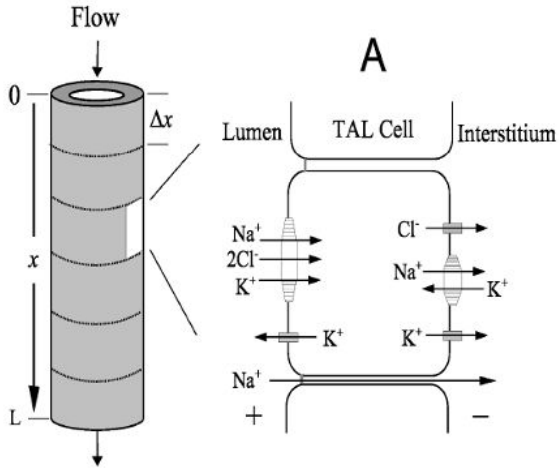

Figure 2.1: TAL tubule model

2.1 Conservation laws and auxiliary equations

As was done in [35, 36], if we assume mass and water conservation, a water impermeable TAL on its luminal (apical) side, a well-stirred and dilute cytosol, fixed serosal (basolateral) concentrations, and a constant electric field across each cell membrane, then the following system of conservation laws (PDE system) can be derived,

$$\frac{\partial}{\partial x}F_w(x,t) = 0 \tag{2.1}$$

$$\frac{\partial}{\partial t}C_i^a(x,t) + \frac{F_w(t)}{A}\frac{\partial}{\partial x}C_i^a(x,t) = \frac{2\pi r}{A}\left(J_i^a(\mathbf{C}^c,\mathbf{C}^a) - J_i^p(\mathbf{C}^a,\mathbf{C}^b)\right) \tag{2.2}$$

$$\frac{d}{dt}C_{ij}^c(t) = (C_{ij}^c(t)A^bJ_w^b(\mathbf{C}^c,\mathbf{C}^b) - (A^aJ_i^a(\mathbf{C}^c,\mathbf{C}^a) + A^bJ_i^b(\mathbf{C}^c,\mathbf{C}^b)))V_j^{-1}(t) \tag{2.3}$$

$$\frac{d}{dt}V_j(t) = -A^bJ_w^b(\mathbf{C}^c,\mathbf{C}^b) \tag{2.4}$$

where x is the axial coordinate along the tubule; t is time; $C_i^a(x,t)$ is the luminal concentration of solute i; $C_{ij}^c(t)$ is the concentration of solute i in a cell at the jth position along the tubule axis; V_j is the volume of a cell the jth position along tubule axis; r is tubule radius, A is the tubule cross-sectional area; $A^{a,b}$ are the apical and basolateral membrane area respectively; and C_i^b is the serosal concentration of solute i. $F_w(x,t)$ is the water flow entering the tubule. Observe that equation (2.1) holds because of the water impermeability of the TAL, and that makes F_w a function of time only. The transmural solute fluxes are denoted by $J_{i,w}^{a,b,p}(\cdot,\cdot)$ where the superscripts a,b,p mean apical, basolateral, or paracellular pathway, the subscripts i,w denote either the i^{th} solute or water (w) and the vector argument, $\mathbf{C}^{a,b,}$, in the flux functions emphasizes the fact that the flux of a solute depends on its own intra/extracellular concentration as well as in the intra/extracellular concentration of other solutes (see below).

The solute fluxes have two components: the electrodiffusive part given by the Goldman-Hodgkin-Katz constant-field flux equation, and the carrier mediated contribution (denoted as J_i^{carrier}), which for a TAL cell, includes the Na^+-K^+/NH_4^+-2Cl^- cotransporter (NKCC2), K^+/NH_4^+-Cl^- cotransporter (KCC4), Na^+-K^+-ATPase (pump), Na^+-H^+/NH_4^+ exchanger (NHE), and HCO_3^--Cl^- exchanger (BCE) transport. The expression for the solute flux is

$$J_i^k(\mathbf{C}^c, \mathbf{C}^k) = \frac{z_i P_i^k u^k (C_i^c \exp(u^k z_i) - C_i^k)}{\exp(u^k z_i) - 1} + J_i^{\text{carrier}}(\mathbf{C}^c, \mathbf{C}^k) \tag{2.5}$$

where $u^k = \frac{FE^k}{RT}$, E^k $(k = a, b, p)$ is the apical, basolateral or transepithelial E^p membrane potential, z_i is the valence of the ith solute, P_i^k $(k = a, b, p)$ is the apical, basolateral or paracellular permeability of the ith solute, and F/RT is the ratio of Faraday's constant to gas constant times absolute temperature. Note that a straight-forward circuit analysis shows that $E^p = E^b - E^a$. The carrier mediated fluxes are computed from steady-state expressions of kinetic models that describe the transporter in question. The kinetic model and the steady-state expression for NKCC2 can be found in [37, 38], KCC4 is based on data from [39, 38], NHE is in [23], BCE in [40], and the model for the Na^+/K^+ pump is in [41]. Moreover, as seen in Figure 2.2 not all carriers are expressed in both cell membranes. The apical (or luminal) side has NKCC2, NHE, and BCE, while in the basolateral (or serosal) side has KCC4, Na^+/K^+ pump, NHE, and BCE. For the sake of completeness, section A.1 of the appendix shows the kinetic models for NKCC2 and KCC4 (Figures A.1 and A.2). Section A.2 shows a slight addition to the Lou and Rudy [41] model for the Na^+/K^+ pump that allow NH_4^+ transport.

Water flow is given by osmosis

$$J_w^b(\mathbf{C}^c, \mathbf{C}^b) = P_w^b \sum_{i=1}^{n} \sigma_i^b (C_i^b - C_i^c) \tag{2.6}$$

where $P_w^{a,b}$ is the water permeability and $\sigma_i^{a,b}$ is the reflection coefficient for solute i^{th} in the apical or basolateral membrane.

In order to enforce electroneutrality in the cytosol and in the outside solutions the following equation must hold

$$\begin{pmatrix} I^a + I^b \\ \\ I^a + I^p \end{pmatrix} = \begin{pmatrix} \sum_{i=1}^{n} (A^a J_i^a(\mathbf{C}^c, \mathbf{C}^a) + A^b J_i^b(\mathbf{C}^c, \mathbf{C}^b)) z_i \\ \\ A^a \sum_{i=1}^{n} (J_i^a(\mathbf{C}^c, \mathbf{C}^a) + J_i^p(\mathbf{C}^a, \mathbf{C}^b)) z_i \end{pmatrix} = \begin{pmatrix} 0 \\ \\ 0 \end{pmatrix}. \tag{2.7}$$

System (2.7) must be solved for the membrane potentials E^a and E^b at each time that the solution of system of differential equations is computed.

Two things are important to point out. First, if we assume that the cell is immersed in infinite baths in both the apical and serosal sides, we end up with a TAL cell model that consists solely of equations (2.3) and (2.4) with auxiliary equation (2.7), see Figure 2.2. Second, equations (2.2) to (2.4) can be written in matrix-vector form $\mathbf{u}_t + M\mathbf{u}_x = \mathbf{F}(\mathbf{u}, \mathbf{x}, \mathbf{t})$ where $\mathbf{u} = (\mathbf{C}^a, \mathbf{C}^c, \mathbf{V})^T$, which is the standard way form for an hyperbolic PDE system. This force us to take the proper precautions when numerically solving the system of equations that describe our model.

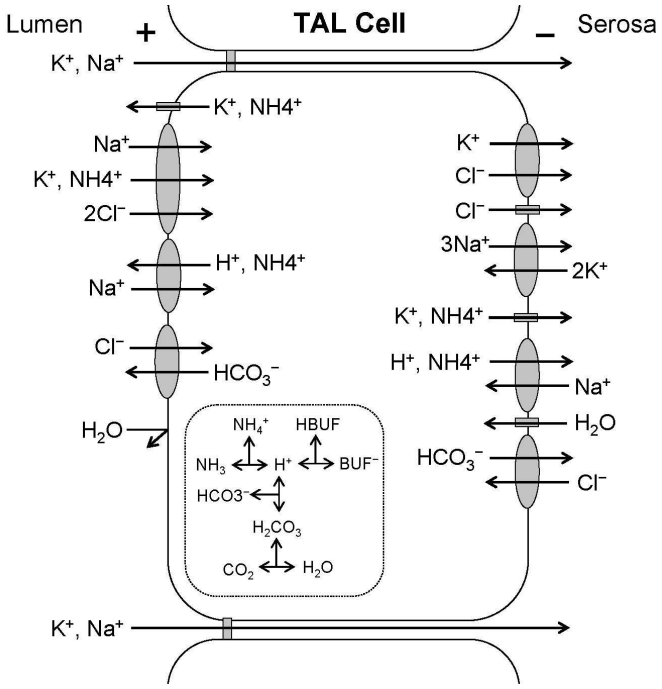

Figure 2.2: TAL cell model

2.2 Boundary and initial conditions

To solve TAL tubule model a mixed boundary condition (BC) is required

$$\mathbf{C}^a(t,0) = \bar{\bar{\mathbf{C}}}^a, \quad \text{constant} \tag{2.8}$$

$$\left.\frac{\partial}{\partial x}\mathbf{C}^a(t,x)\right|_{x>L} = 0, \tag{2.9}$$

where L is the length of the TAL tubule. The initial conditions are

$$\mathbf{C}^a(0,x) = \bar{\mathbf{C}}^a(x) \quad \text{constant} \tag{2.10}$$

$$\mathbf{C}^c(0) = \bar{\mathbf{C}}^c \quad \text{constant} \tag{2.11}$$

$$V_k(0) = \bar{V}_k \quad \text{constant, for all cells.} \tag{2.12}$$

Table 2.2 gives the numeric values of the constants.

2.3 pH homeostasis

The acid-base solutes H^+, NH_4^+, NH_3, H_2CO_3, HCO_3^-, $H_2PO_4^-$, and HPO_4^{2-} constitute three buffer systems, and special care must be taken since the concentrations of those solutes depend on transmural fluxes and on their ionization reactions. If we denote the three buffer systems as

$$\begin{gathered} B_1 = [\mathrm{NH_4^+}] + [\mathrm{NH_3}], \quad B_2 = [\mathrm{H_2CO_3}] + [\mathrm{HCO_3^-}] \quad B_3 = [\mathrm{H_2PO_4^-}] + [\mathrm{HPO_4^{2-}}] \\ H_t = [\mathrm{H^+}] + [\mathrm{NH_4^+}] + [\mathrm{H_2CO_3}] + [\mathrm{H_2PO_4^-}], \end{gathered} \tag{2.13}$$

and assume the isohydric principle, and that the buffers are in equilibrium we get

$$[\mathrm{H^+}] + \sum_{k=1}^{3} \frac{B_k[\mathrm{H^+}]}{[\mathrm{H^+}] + K_k} - H_t = 0, \tag{2.14}$$

where K_k is the corresponding equilibrium constant. This equation is solved for $[H^+]$ and from (2.13) the buffer constituents are recovered. Additionally, it is important to take into account the hydration/dehydration of CO_2. Since it is slow compared to the ionization of carbonic acid, a chemical "flux" or source must be added to the conservation law involving H_2CO_3 (that is B_2). That chemical source is given by

$$J^{\mathrm{chem}}_{\mathrm{H_2CO_3}} = \left(k_d C_{\mathrm{H_2CO_3}} - k_h C_{\mathrm{CO_2}}\right) V_{\mathrm{cell,lum}}, \tag{2.15}$$

where k_d and k_h are the hydration and dehydration constants for CO_2. All of this allows us to solve for the total buffers (B_1, B_2, B_3, H_t) in (2.2) and (2.3) and, therefore, to have an appropriate representation of the acid buffering system in the cytosol as well as in the lumen.

2.4 Cell volume regulation

TAL cells swell because of an increase in luminal solute uptake or a decrease in serosal bath osmolarity with respect of that of the cytosol. Cells respond to swelling with a regulatory volume decrease (RVD). Such a response can be a long term one by the release of uncharged impermeant solutes, or a short term one by regulation of solute transport. The long term response was simulated by initially setting the concentration of impermeant solutes high enough to match the osmolarity in the serosal bath, particularly in the outer medullary regions of the TAL where serosal osmolarity reaches values of about 500 mOsm. The short term response was modeled by defining functions that map cell volume to the total activity (or enzyme or transporter density) of the NKCC and KCC transporters. The functions are based on observations by Kahle [27] and they are

$$g_{NKCC}(V_j) = \begin{cases} E^{NKCC}_{\max}, & \text{if} \quad V_j \le V_{set} - \delta_1^{NKCC} \\ m_{NKCC}V_j + b_{NKCC}, & V_{set} - \delta_1^{NKCC} < V_j < V_{set} + \delta_2^{NKCC} \\ E^{NKCC}_{\min}, & V_{set} + \delta_2^{NKCC} \le V_j \end{cases} \tag{2.16}$$

$$g_{KCC}(V_j) = \begin{cases} E^{KCC}_{\min}, & \text{if} \quad V_j \le V_{set} - \delta_1^{KCC} \\ m_{KCC}V_j + b_{NKCC}, & V_{set} - \delta_1^{KCC} < V_j < V_{set} + \delta_2^{KCC} \\ E^{KCC}_{\max}, & V_{set} + \delta_2^{KCC} \le V_j \end{cases}, \tag{2.17}$$

where

$$m_{NKCC} = \frac{E^{NKCC}_{\min} - E^{NKCC}_{\max}}{\delta_2^{NKCC} + \delta_1^{NKCC}}, \quad b_{NKCC} = E^{NKCC}_{\min} - m_{NKCC}(V_{\text{set}} + \delta_2^{NKCC}),$$
$$m_{KCC} = \frac{E^{KCC}_{\max} - E^{KCC}_{\min}}{\delta_1^{KCC} + \delta_2^{KCC}}, \quad \text{and} \quad b_{KCC} = E^{KCC}_{\min} - m_{KCC}(V_{\text{set}} - \delta_1^{KCC}).$$

The above piecewise linear functions are depicted in Figure 2.3, and they can be smoothed by a piecewise Hermite polynomial interpolation to enforce monotonicity.

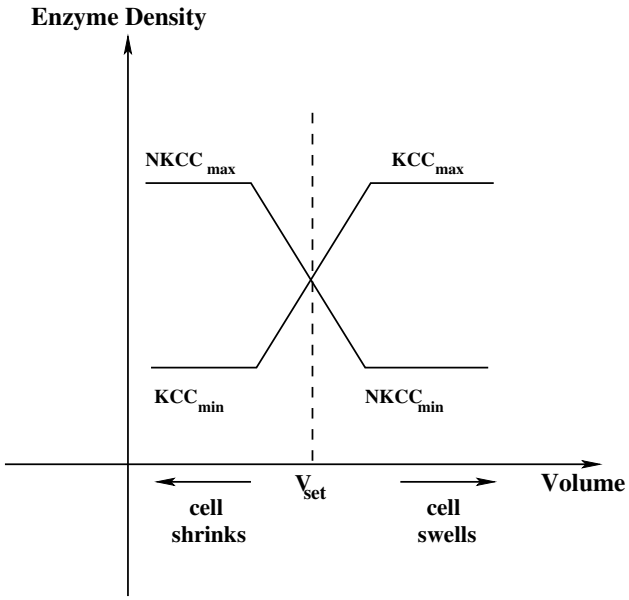

Figure 2.3: Cell volume regulation functions

2.5 Tubular Water Flow

The function $F_w(t)$ in (2.2) determines the water flow into the TAL tubule, and the specific requirements of a simulation will determine how $F_w(t)$ is defined. The simplest case is constant inflow

$$F_w(t) = \alpha Q, \quad \text{constant} \tag{2.18}$$

where Q is the steady-state single nephron glomerular filtration rate (SNGFR) and α is the fraction of SNGFR reaching the TAL. Simulations that involve sinusoidal forcing use:

$$F_w(t) = \alpha Q(1 + \eta \sin(2\pi f t)) \tag{2.19}$$

where η will determine the amplitude of the forcing, and f its frequency. A square-wave forcing is:

$$F_w(t) = \alpha Q(1 + \eta \text{sgn}(\sin(2\pi f t))). \tag{2.20}$$

In simulations that require a broad-band forcing, we defined the water inflow to be:

$$F_w(t) = \alpha Q \left(1 + \sum_{k=1}^{6000} \eta_k \sin(2\pi f_k t - \phi_k)\right) \tag{2.21}$$

where $f_k \in (0, (2\Delta t)^{-1}]$, ϕ_k are random numbers uniformly distributed in $[0, 2\pi]$, and Δt is time a step as determined by the stability condition of the numerical scheme used to solve (2.1)- (2.4) (see below). Notice that the frequencies are not chosen to be equal to the frequency discretization that comes from the discrete Fourier transform (DFT) necessary for the analysis of the system in the frequency domain.

Some simulations require coupling of the TAL model with the tubuloglomerular feedback system (TGF). Following the work in [9], we define

$$F_w(t) = \alpha(Q_{op} + 0.5\Delta Q \tanh(0.5k(C_{op} - C_{\text{MD}}(t)))) \tag{2.22}$$

$$C_{\text{MD}}(t) = \int_{\infty}^{t} \Psi(t - s - 0.5\tau_d) C^a_{\text{Cl}^-}(L, s - \tau) ds \tag{2.23}$$

$$\Psi(u) = \begin{cases} (1 + \cos(\frac{2\pi u}{\tau_d}))\tau_d^{-1} & \text{if} \quad |u| \leq 0.5\tau_d \\ 0 & \text{otherwise} \end{cases} \tag{2.24}$$

where equation (2.22) is the phenomenological representation of TGF on water flow, equation (2.23) represents the delays between changes in luminal Cl^- at the end of the tubule ($x = L$) and effective Cl^- concentration at the macula densa. The delays are composed of a pure delay τ that represents the elapsed time from the stimulus until muscle tension in the afferent arteriole changes, and τ_d is the total time over which the effect (change in afferent

arteriole diameter) is distributed. Equation (2.24) is the kernel function that characterizes the distributed delay. As discussed in [42], since the delay caused by the distributed delay is much shorter than a fluid particle's transit time (see below), the specific functional form chosen in (2.24) is unimportant as long as it meets the physiological criterion of being sigmoidal, and has the mathematical properties of being continuous in the real line, non-negative in the delay interval, and with a weight of one in the delay interval in order to enforce the condition that a nonchanging concentration goes through the delay unchanged.

2.6 Numerical solution

Equations (2.1) to (2.4) are solved numerically using a parallelized simple splitting min-mod flux limiter. The splitting procedure, as explained in [43], involves doing a time-step for the conservation law (the left-hand side of (2.2)), using the min-mod flux limiter, and combining it with a time-step for the source term (the right-hand side of (2.2) to (2.4)). The flux limiter does an upwind, or a Lax-Wendroff, or a combination of both according to the steepness of the derivative of the function; see [44] for details. The time-step for the source term involves solving a system of ordinary differential equations (ODE), using an order-two Backward Differentiation Formula (BDF). To ensure stability we enforce the upwind (forward time backward step) stability condition

$$0 \leq R = \frac{\max\{F_w\}}{\min\{A\}} \frac{\Delta t}{\Delta x} \leq 1.$$

Hence, a given number of cells leads to a space discretization ($\Delta x = L/N$) and then a time discretization (Δt) follows from the stability condition.

As mentioned above, the time-step for the source term involves solving an ODE system at each space discretization. Since the ODE systems are not explicitly dependent on each other, that part of the problem is embarrassingly parallel (no inter-problem communication). In practice we end up assigning an equal number of subproblems to each of the available computing cores. This gave us a linear speedup in the number of processor cores compared to the serial version. Also, to verify our approach, we solved the PDE system problem using the method of lines (MOL) [45]. The idea of that method is to discretize the space operator of (2.2) with a backward step and afterward solve the whole problem as an ODE system. As expected, this yielded the same results, albeit the method slower than with the parallelized simple-splitting flux limiter.

The electroneutrality constraint given in equation (2.7) is solved with a generalized secant with Broyden update method. Although this has a lower order of convergence than Newton's method, it requires less function evaluations owing to the fact that only one finite difference approximation of the Jacobian matrix is required per call. For our problem, that decreases significantly the total amount of time needed to solve the model.

Equation (2.14), the pH homeostasis equation, can be written as a fourth degree polynomial in $[H^+]$ and its roots computed by constructing the companion matrix and finding its eigenvalues.

The implementation of the numerical methods was done in MATLAB®. For the BDF, we used the implementation that is part of the MATLAB® suite of ODE solvers. The computing resource used was a Linux box with 8GB of memory and two Intel® quad-core Xeon® X5473 3GHz CPUs. The amount of time required to solve the system of

conservation laws (equations (2.1)-(2.4)), with initial and boundary conditions as given in section 2.2 and constant inflow rate of 6 nL/min is $\sim$3 minutes for 60 s of simulation. This is obtained, using the parallelized simple-spitting flux limiter scheme described above with 7 computing cores. Solving the problem in serial takes 21 minutes. In general, we noticed a linear speedup when going from the serial to the parallelized approach to solving this problem.

2.7 Model parameters

The next step in the development of the model is the identification of sets of parameters that yield model behaviors consistent with experimental data. In this chapter, we present the parameter values and discuss how they were found. In chapter 3, we will present the simulation studies which demonstrate that, with these parameter sets, our model's behavior is, indeed, consistent with a variety of experimental data.

Table 2.1 contains the physical dimensions of the TAL, its chemical properties, and the value for baseline flow into the TAL. Figure 2.4 shows the chemical composition of the serosal bath or the interstitium along the length of the TAL. Notice the high osmolarity ($\sim$500mOsm) in the deepest part of the TAL (outer medulla), and that halfway along the tubule is the cortico-medullary junction. The values for this set of concentrations, in particular Na^+, are close to what is reported in [35].

Table 2.2 gives the values used as initial and boundary conditions to solve the model. Is important to remark that while we use the same boundary conditions in all simulations

Table 2.1: Basic physico-chemical parameters

	description	value	reference
N	number of cells	70	N/A
L	TAL length (cm)	0.6	[46]
r	TAL radius (μm)	10	[46]
V_{lum}	TAL tubule volume (cm^3)	1.885×10^{-6}	calculated[a]
A^a	apical memb. area per unit length (cm^2/cm)	0.01515	[47]
A^b	basolateral memb. area per unit length (cm^2/cm)	0.0944	[47]
α	fraction of SNGFR reaching TAL	0.2	[48]
Q	steady-state SNGFR (nL/min)	30	[49]
pK_1	pK for NH_4^+/NH_3 buffer	9.15	[50]
pK_2	pK for H_2CO_3/HCO_3^- buffer	3.57	[50]
pK_3	pK for $H_2PO_4^{2-}/HPO_4^-$ buffer	6.8	[50]
k_h	CO_2 hydration constant (s^{-1})	1450	[11]
k_d	CO_2 dehydration constant (s^{-1})	496000	[11]
p_{CO_2}	partial pressure of CO_2 (mmHg)	55	[51]
F	Faraday's constant (coul·mol^{-1})	96500	[50]
R	gas constant (JK^{-1}mol^{-1})	8.314472	[50]
T	average human body temperature (K)	310.15	N/A

[a] We assumed a cylindrical geometry for the tubule: $\pi r^2 \Delta x$. This is luminal volume, so walls are not included.

described in this work, that is not the case for the initial conditions. The initial conditions in Table 2.2 is simply uniform luminal concentrations along the TAL. Whenever we use an initial condition different from the value in Table 2.2, it will be clearly stated in the text.

Figure 2.5 shows the ranges for apical, basolateral, and paracellular permeabilities chosen for the electrodiffusion of each solute across the TAL epithelium. The parameters for the membrane embedded carriers and the specification of which membrane contains what carrier is in Table 2.3. Now, those parameter sets are not arbitrary. In [37, 38] we sought sets of rate constants for the NKCC and KCC cotransporters. We did that by posing an inverse problem, that is, we minimized the euclidean distance between the fluxes computed with NKCC and KCC kinetic model and the experimental fluxes. That minimization, or

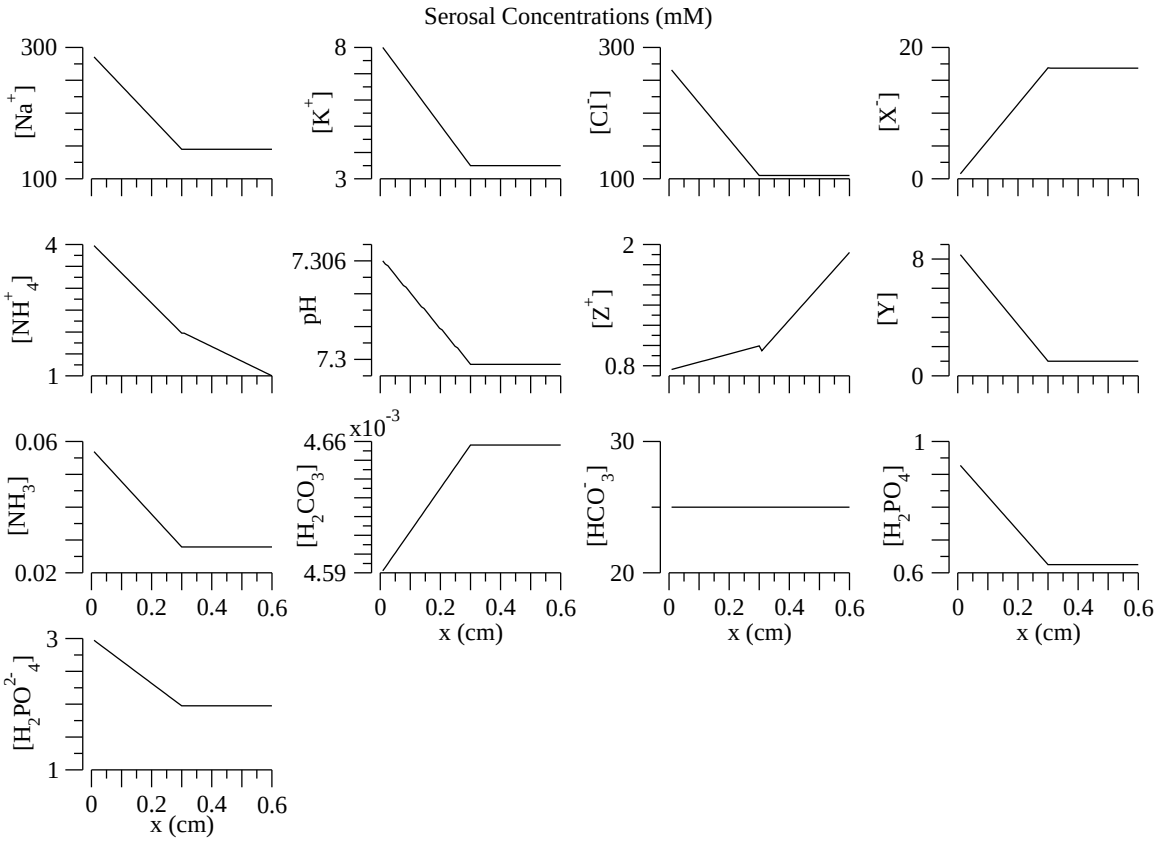

Figure 2.4: Serosal concentration profile. Based on [35].

least-squares problem, was solved using a deterministic locally convergent, trust-region method that was fed with a random population of initial guesses to avoid getting stuck in a local optimum. We apply a similar strategy in this work when trying to find parameter sets for the TAL cell and segmental model. In Figures 2.5 and 2.6, permeabilities and max/min NKCC/KCC activities were chosen such that outflow and luminal concentration profiles, and transepithelial electrical and chemical gradients computed by the model are close (in the 2-norm sense) to experimental values [52, 26].

A word of caution is in order. Finding a parameter set that solves the least-squares problem between a cell model (equations (2.3) and (2.4)) generated output and a particular experimental output is no guarantee that the same set will give satisfactory results when the

Table 2.2: Values for initial & boundary conditions[a]

	initial in		
	lumen[b]	cytosol	boundary
$[Na^+]$	252.00	7.0000	252.00
$[K^+]$	8.0000	136.0000	8.0000
$[Cl^-]$	236.25	4.4000	236.25
$[X^-]$	27.709	112.51	27.709
$[Y]$	0.30000	[6.0000, 306.10][c]	0.30000
$[Z^+]$	33.709	0.90754	33.709
pH	7.266	7.284	7.266
$[NH_4^+]$	3.9748	5.0118	3.9748
$[NH_3]$	0.051875	0.068228	0.051875
$[H_2CO_3]$	0.0050385	0.0048303	0.0050385
$[HCO_3^-]$	25.000	25.000	25.000
$[H_2PO_4^-]$	1.2750	0.98822	1.2750
$[HPO_4^{2-}]$	3.7250	3.0118	3.7250
V_{cell}[d]	N/A	8.1955×10^{-8}	N/A

[a] Concentrations in mM & volume in cm^3.
[b] Uniform along the length of the tubule.
[c] Range from cTAL to mTAL.
[d] Computed by assuming the TAL radius including the walls is $2r$ (see Table 2.1) and then $V_{\text{cell}} = \pi(2r)^2\Delta x - V_{\text{lum}}$.

cell is part of the tubule model (equations (2.1) to (2.4)). We attribute this to the fact that when the optimization problem is solved for an isolated cell, we have to simulate a scenario akin to the one in which the measurements were taken. If that scenario is not the same as the ambient environment in which the cell "lives" when embedded in the tubule model, then we are changing parameters that might had been considered as fixed when solving the original least-squares problem. An effect of that parameter change is that the segmental model would not yield results in total agreement with experimental observations, and we have to again pose and solve a new least-square problem to readjust the parameters. A work-around could be to solve one inverse problem composed of the different least-squares

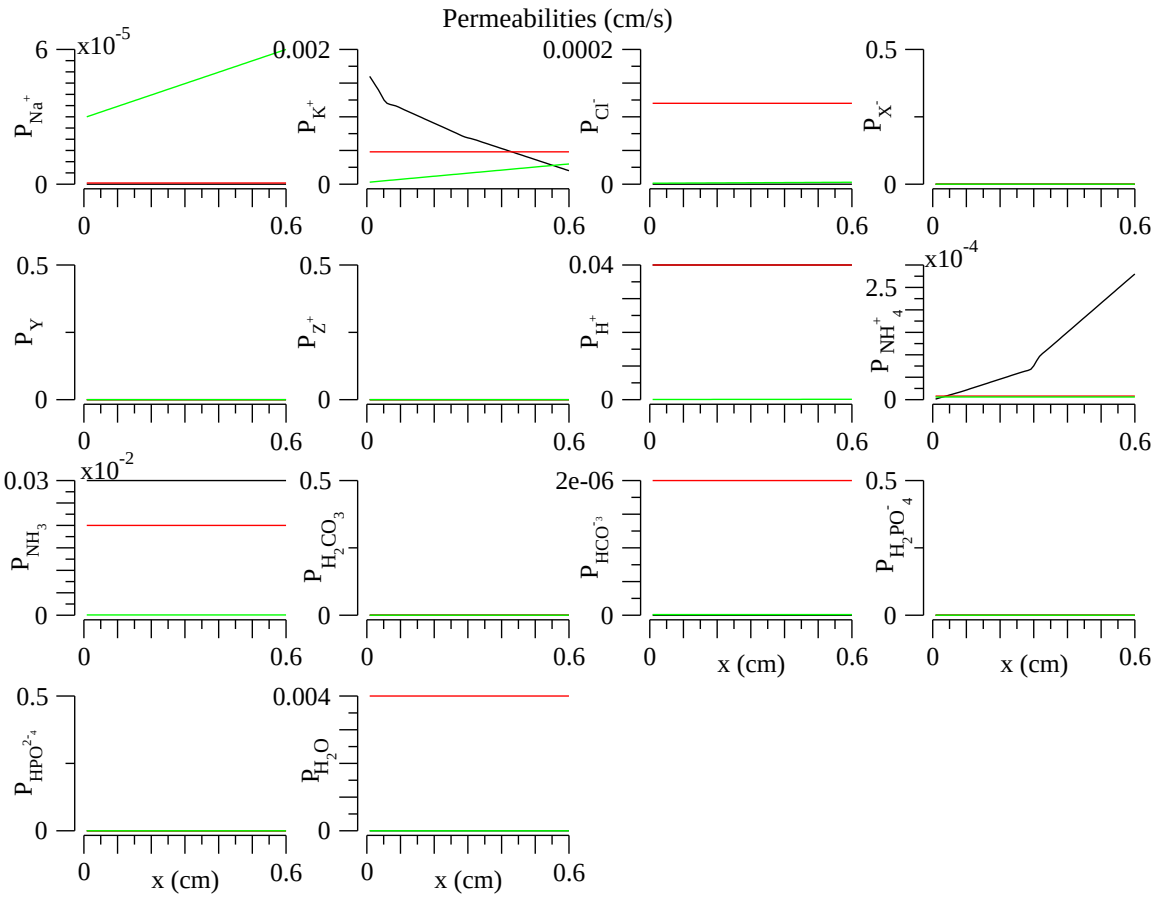

Figure 2.5: Permeabilities along the TAL. Black is apical, red is basolateral, and green is junctional. When only one curve is seen, it means that it overlaps the others.

between the whole tubule model and different experimental outputs. Mathematically this can be expressed as:

$$\min_{\mathbf{p}_l \leq \mathbf{p} \leq \mathbf{p}_u} \|\mathbf{F}_{\text{model}}(\mathbf{p}) - \mathbf{F}_{\text{expe}}\|_2^2 , \tag{2.25}$$

$$\text{subject to} \quad \mathbf{G}(\mathbf{p}) \leq \mathbf{0}$$

where $\mathbf{p}$ is the vector of parameters, $\mathbf{p}_l$ and $\mathbf{p}_u$ are lower and upper bounds on the parameters, $\mathbf{F}_{\text{model}}$ and $\mathbf{F}_{\text{expe}}$ are model and experimental outputs respectively, and $\mathbf{G}$ represent the whole list of physiological constraints given by the different experimental preparations. The inequalities are read componentwise. A drawback of solving the problem as expressed in (2.25) is that scores of parameter have to be changed at once, and that for each pertur-

Table 2.3: Carrier mediated transport parameters[1]

carrier	apical	basolateral	reference
NKCC2 isoform A	⋆		[38]
NKCC2 isoform B	⋆		[38]
NKCC2 isoform F	⋆		[38]
KCC4		⋆	[39, 38]
NHE3	⋆	⋆	[23]
BCE		⋆	[40]
Na-K pump		⋆	[41]

[1] Star means carrier is embedded in the cell membrane.

bation on the parameter set a PDE system (equations (2.1) to (2.4)) has to be solved. Even with an optimization method that does not require approximation of the Jacobian matrix of the objective function, like simulated annealing, this would be a computationally intensive problem. Another drawback, which is potentially more damaging, is that the physiological constraints of different experimental setups might be exclusionary of one another. An example of this is an experimental setup involving TAL cells in Ringer's solution (like [53]), and a TAL cell in the outer medulla, where the interstitium contains much more Na^+, K^+, Cl^-, and NH_4^+.

Table 2.4: Tubuloglomerular feedback parameters

	description[a]	value	reference
k	sensitivity of TGF response (mM^{-1})	0.1625	N/A
C_{op}	SS $[Cl^-]_{MD}$ (mM)	28.44	N/A
Q_{op}	SS SNGFR (nL/min)	30	[49]
ΔQ	TGF-mediated range of SNGFR (nL/min)	18	[54, 9]
τ	pure delay interval at JGA (s)	2	[14, 42]
τ_d	distributed delay interval at JGA (s)	3	[14, 42]
γ	gain[b]	249.49	N/A

[a] SS means steady-state, SNGFR stands for single nephron glomerular filtration rate, and JGA is juxtaglomerular apparatus.

[b] γ is a composite nondimensional parameter defined as $\gamma = (\frac{\Delta Q}{\alpha Q_{op}})(\frac{kC_{bnd}}{2})(\frac{L}{C_{\text{bnd}}})(\frac{dC}{dx})$ where $C_{bnd} = C_{Cl^-}(x = 0)$ and $\frac{dC}{dx}$ is at SS and evaluated at $x = L$

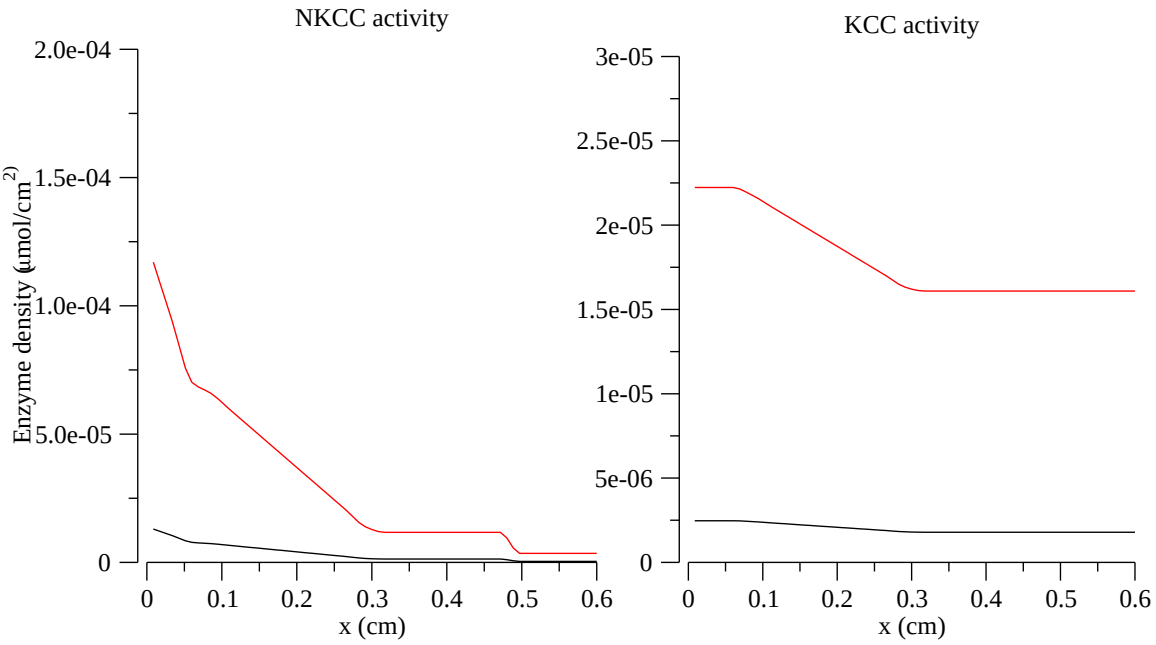

Figure 2.6: NKCC & KCC maximum and minimum enzyme density for cell volume regulation function defined in (2.16) and (2.17) and depicted in Figure 2.3. Red is maximum, and black is minimum.

Chapter 3

Results

3.1 TAL cell model

In this section, we present simulations using the TAL cell model. Our goals are 1) to show that our model's behavior is consistent with experimental data, and 2) to evaluate the efficiency of Na^+ transport by the cells.

3.1.1 Electrophysiological properties

To verify that the cortical TAL (cTAL) cell model, composed of equations (2.3) and (2.4) with auxiliary equation (2.7), can behave like a TAL cell, we calculated electrophysiological properties for comparison with published data. The calculation consisted of running the cell model to steady-state, injecting a $100\mu A/cm^2$ current for a brief period of time,

and then computing the membrane potential deflections and the corresponding resistances. Figure 3.1 illustrate the above described protocol. Table 3.1 shows the experimental and

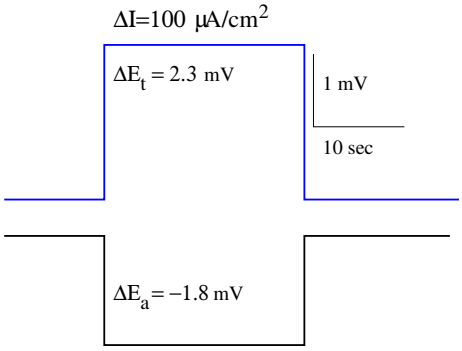

Figure 3.1: Current pulse simulation

computed short-circuit current (I_{sc}) or current when there is no transepithelial electrochemical gradient; apical, basolateral, and transepithelial membrane resistance (R_a, R_b, R_t); and the voltage divider ratio (R_a/R_b). From the table, we conclude that our cell model with the chosen set of parameters has electrophysiological properties similar to a TAL cell. However, it is important to mention that this result exhibits a marked dependency on apical and basolateral membrane area.

Table 3.1: Electrophysiological properties of a model cTAL cell[a]

	I_{sc} (μAcm^{-2})	R_a (Ωcm^2)	R_b (Ωcm^2)	R_t (Ωcm^2)	R_a/R_b
Computed	260.8	69.4	22.0	23.3	3.16
Experimental	285±33	30-87	20-47	10-35	2.8±0.5

[a] Experimental I_{sc} and R_a/R_b are from [55]; the other values from [52].

Greger and coworkers [55] measured short-circuit current (I_{sc}) as a function of parallel, isotonic increases in luminal and serosal Cl^- concentration. Figure 3.2 shows short-circuit current simulations done according to Greger's protocol in [55]; panel A shows simulation results done with a cell model "extracted" from different locations along the length of the TAL, while panel B displays results from a cell with and without cell volume regulation

(CVR). We observe in panel A as well as in Table 3.2 that, depending on the cell's location along the tubule, the fit to Greger's data improves or worsens. This follows from the fact

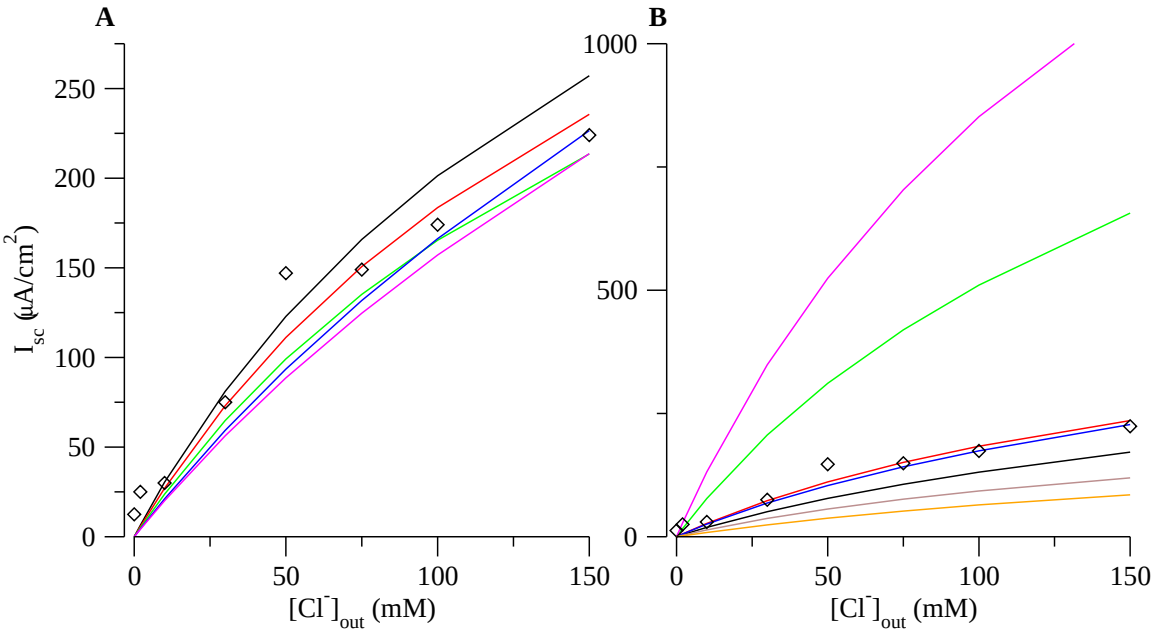

Figure 3.2: Panel A is Na^+ I_{sc} for cells at different locations along TAL where the start of the tubule is at the OM: black is a cell at 19% from the start of the TAL tubule, red is a cell at 21% of the TAL, green is a cell at 24% (at OM), blue is a cell at 50% (cortico-medullary junction), magenta is a cell at 79% (cortex), and diamonds are Greger's data [55]. Cells on this case have CVR. Panel B is Na^+ I_{sc} under a variety of CVR regimes: red is with CVR, black is no CVR with down regulation of NKCC and KCC, green is no CVR with uniform NKCC and KCC activities, blue is no CVR with NKCC and KCC activities that yield the optimal R^2 value, magenta is no CVR with up regulation of NKCC and KCC, brown is no CVR with KCC dominant, orange is with CVR and KCC dominant, and diamonds are Greger's data.

that certain parameters from the cell model, like permeabilities or transporter activity, are not uniform for all cells (see Figure 2.5 and 2.6). Also, from the biological standpoint, cells have to adapt to the environment in which they developed; hence short-circuit current and other electrophysiological properties will show variation among cells along the TAL tubule. It is also noteworthy that, since Greger's data is from cTAL cells, the departure from the data of the cell model at the chosen locations, as determined by the R^2 value, is not huge (only 8% relative difference between the best and worst in Table 3.2). But if we

Table 3.2: R^2 values for short-circuit current simulations[a]

TAL location[b]	TAL region	R^2
at 19% of TAL	OM	0.9263
at 21% of TAL	OM	0.9534
at 24% of TAL	OM	0.9238
at 50% of TAL	Cort-Med	0.9140
at 79% of TAL	Cortex	0.8769

[a] Data are from [55].
[b] Location is ratio of cell number to N, where cell one is at the TAL entrance.

pick cells at the very beginning of the OM, the departure from data increases markedly. In panel B we note that cell volume regulation has an impact in the goodness of fit and in the transport properties of the cell as embodied by the short circuit current measure. This was expected because NKCC and KCC are major players in transepithelial Na^+ transport and their activities are determined by cell volume through the CVR function defined in equations (2.16) and (2.17). Panel B also shows that for the cases of KCC dominance (brown and orange curves), which is defined here as maximum and minimum activity of KCC is greater than that of NKCC, the short-circuit current from the cell model is below Greger's measurements. This underlines the importance of NKCC as an Na^+ uptake pathway for TAL cells.

Together, these results show that our TAL cell model predicts behaviors consistent with key measurements of Na^+ and Cl^- transport. Importantly, these results demonstrate that the adjustments in TAL cell Na^+ transport secondary to CVR responses are essential in simulating the effect of increasing external Cl^- concentration on TAL cell transport.

3.1.2 Cell Volume Regulation

Figure 3.3 shows normalized cell volume (V/V_{set}) obtained from the short-circuit current simulations. Panel A shows cells at different locations along the TAL and panel B is for a cell at 21% from the start of the TAL but with different cell volume regulation regimes. From panel A we observe that all cells along the tubule exhibit a linear swelling trend as outside concentration increases, but for cells deeper in the OM, the trend has a slightly greater slope. The cell at 19% of the TAL shrinks when going from the third to the fourth concentration step, but afterwards the swelling trend is restablished. Is also seen in panel A that, as we move deeper in the OM, the cell volume is greater than the CVR set volume (V_{set}); this implies, by definition of the CVR function, that the NKCC activity and therefore transcellular solute transport will tend to be reduced. Panel B shows that with a CVR (black circle) mechanism in place, although cell volume is still increasing, it is below the cases without volume regulation schemes, with the exception of the cases in which KCC activity dominates that of NKCC (orange plus sign and magenta left triangle). The cause for this is that the cases with KCC dominant, the transporter activity yields a diminished solute uptake (see Figure 3.2) coupled with maximum extrusion through KCC and therefore less cell swelling. The case of no CVR but NKCC and KCC activity adjusted to yield a short-circuit current close to Greger's measurements (blue triangle) show conspicuous increase in volume at 50 mM. The reason in this case, is that NKCC has to be up-regulated and KCC down-regulated substantially. Hence the KCC, which provides an important extrusion pathway, cannot keep up with the uptake from NKCC, thereby causing an increase in internal osmolarity which increases water flow through the basolateral side,

resulting in an increase in cell volume.

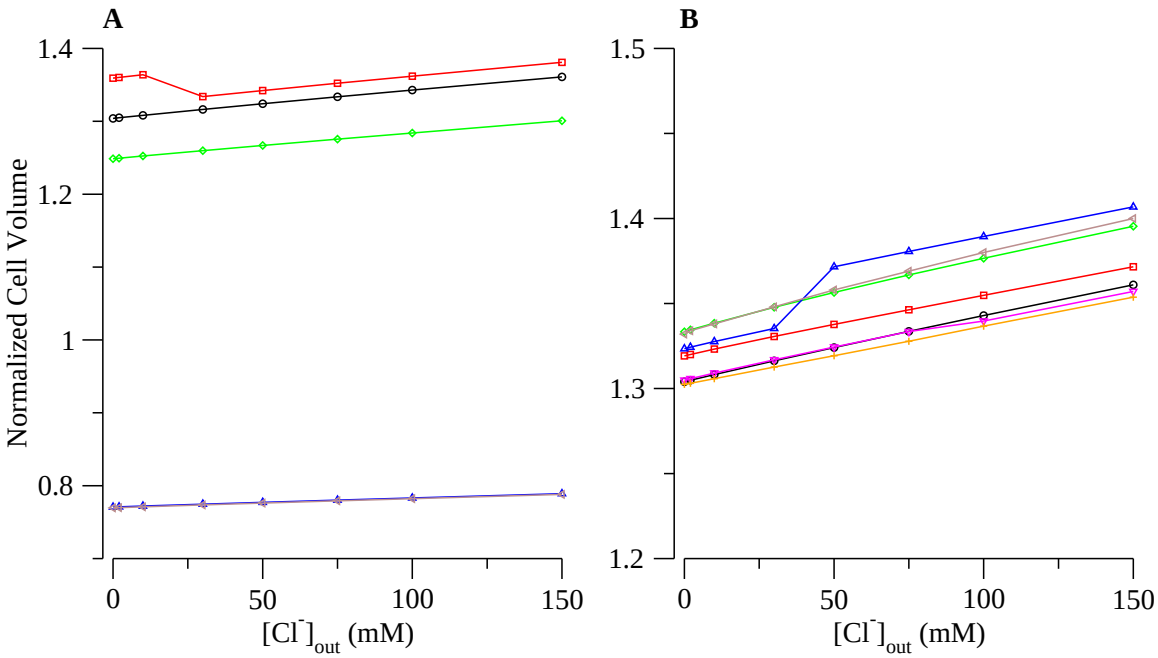

Figure 3.3: Normalized cell volume (V/V_{set}). Panel A is cell volume at different locations along TAL where the start of the tubule is at the OM: red square is a cell at 19% of the TAL tubule, black circle is a cell at 21% of TAL, green diamond is a cell at 24% (at OM), upward blue triangle is a cell at 50% (cortico-medullary junction), and left brown triangle is a cell at 79% (cortex). Note that the brown and blue curve overlap one another. Panel B is a cell volume for a cell at 21% of the TAL under a variety of CVR regimes: black circle is with CVR, red square is no CVR with down regulation of NKCC and KCC, green diamond is no CVR with uniform NKCC and KCC activities, blue upward triangle is no CVR with NKCC and KCC activities that yield optimal R^2 value (i.e. best fit to data), magenta downward triangle is no CVR with KCC dominant, brown left triangle is no CVR with up regulation of NKCC and KCC, and orange plus sign is CVR with KCC dominant.

Figure 3.4 shows cytosolic Na^+, K^+, and Cl^- concentrations for short-circuit current simulations where different CVR modes were enforced. Note that without CVR and either uniform or up regulation of NKCC & KCC activity, the rate of change of cytosolic concentration as a function of outside Cl^- is higher compared to the cases with CVR or down regulation of the transporters, whereas with no CVR or with down regulation of NKCC reduces transcellular transport, it is expected that changes in cytosolic concentration are also reduced. This is seen in Figure 3.4, but it is also seen that CVR responses diminish

swings in cytosolic concentrations though not at the expense of solute reabsorption (Figure 3.2). Also noteworthy is the swing in K^+ for the case of no CVR with up regulation of NKCC and KCC (left magenta triangles), and for the case of no CVR with NKCC and KCC adjusted for optimal R^2 (blue up triangle). The downward swing for the no CVR and optimal R^2 case (i.e. best fit to data), is explained by the increase in volume mentioned in Figure 3.3 for precisely that case. The upward swing for the no CVR and maximum NKCC and KCC activity cases can be explained by increased K^+ uptake by NKCC when it is up regulated. These results highlight the importance of CVR in the stabilization of cytosolic composition as well as cell volume.

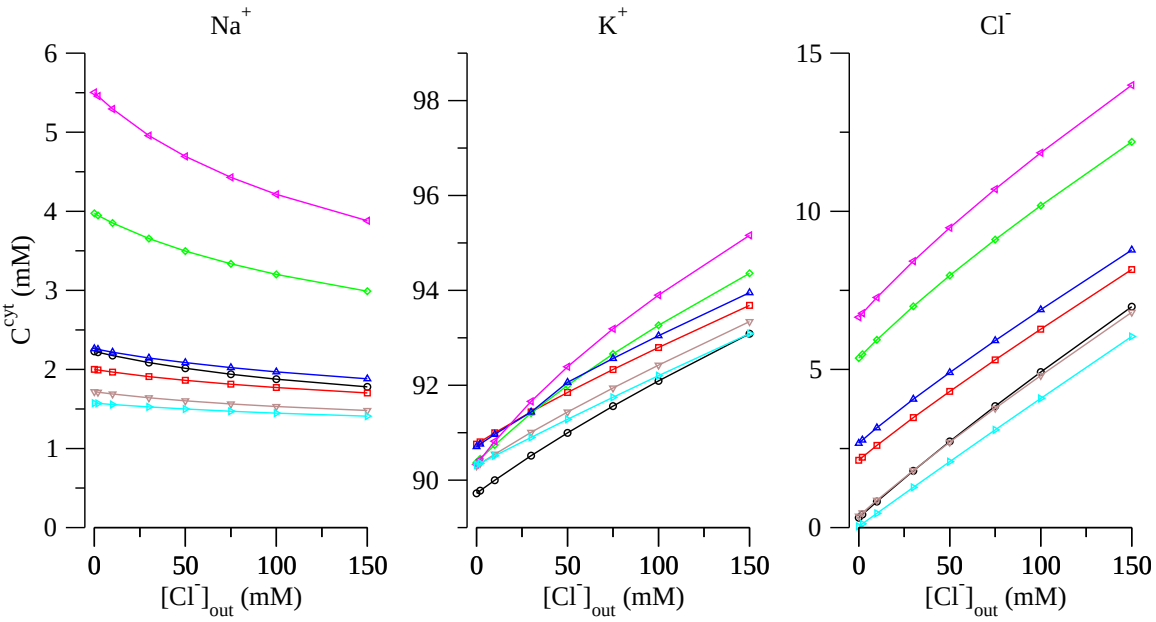

Figure 3.4: Cytosolic concentrations as function of isotonic increases in luminal and serosal concentrations. This is for a cell at 21% of the start of the TAL. Black circles is cell with CVR, red square is no CVR with down regulation of NKCC and KCC, green diamond is no CVR with uniform NKCC and KCC activities, blue upward triangle is no CVR with NKCC and KCC activities that yield optimal R^2 value, left magenta triangle is no CVR with up regulation of NKCC and KCC, brown down triangle is no CVR with KCC dominant, and right cyan triangle is CVR with KCC dominant.

3.1.3 Ammonium transport

In contrast to most systems of the human body, NH_4^+ is present in the kidneys in non-neglectible amounts. It is produced by the proximal tubular cells from the buffering of a free proton by NH_3. Furthermore, as shown by Watts and Good [21], the expression of NKCC2 in mTAL cells gives ammonium ion another entry pathway into the cytosol, and that yields a cytosolic acidification when the cell is submitted to an NH_4^+ pulse perturbation. Following Watts' procedure in [21], we simulate a luminal NH_4^+ pulse perturbation and record the time course of the change in cytosolic pH. The results of those simulations are shown in Figure 3.5 and these are similar to what Watts and Good reported [21] (the pH time course from [21] is shown in Figure 3.6). As shown experimentally, NKCC2 is the major uptake pathway for ammonium, though it is not the only one since it can also permeate K^+ channels. Figure 3.5 panel A shows the cytosolic acidification that follows an ammonium perturbation on the luminal side. Panel B also shows a pH drop, but of lower magnitude since NKCC2 activity was diminished to simulate the presence of the diuretic furosemide. Panel C shows similar drop to the one on panel B, but in this case it is the NH_4^+ and K^+ permeabilities that are reduced to simulate channel blockage due to the presence of Ba^{2+}. Panel D show a much smaller cytosolic acidification than in the other cases, and this is due to inhibition of both NKCC2 and the electrodiffusive pathway for NH_4^+ entry into the cell. It is important to mention that the pH drop shown in Figure 3.5 can be diminished or augmented by up-regulation or down-regulation of NH3 activity. In particular, we have observed that increasing NH3 activity on the basolateral side substantially reduces the pH drop under all of the above mentioned simulation protocols. The reason is that

NH3 extrudes NH_4^+ and H^+, which dampens the pH drop, and absorbs Na^+, which will increase cytosolic Na^+ and therefore reduce the concentration gradient that drives uptake by NKCC2 on the apical side.

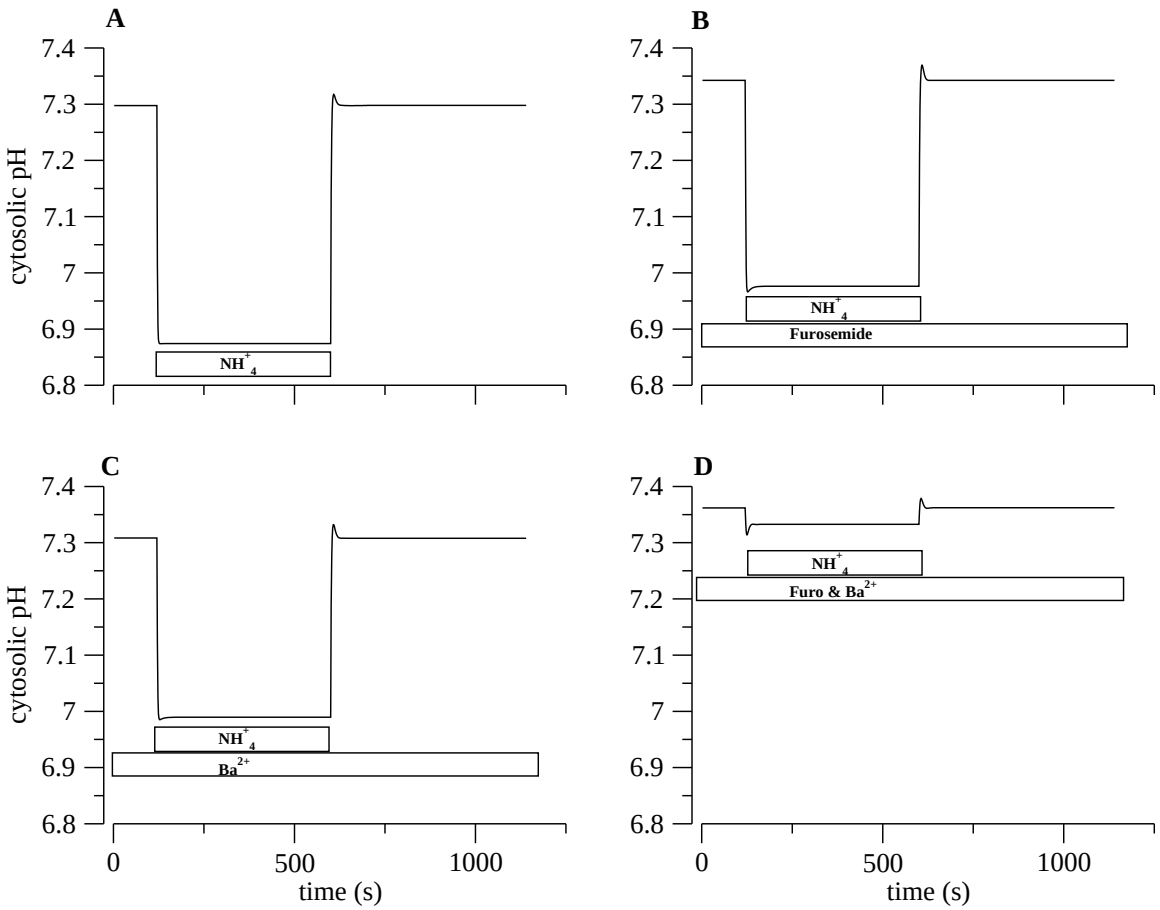

Figure 3.5: Simulations, based on experiments by Watts and Good [21]. In all panels luminal [NH_4^+] was increased from 1.6 mM to 20 mM for 8 minutes. Panel A is control. In panel B the cell was washed in Furosemide to inhibit NKCC. In panel C, the solution in the luminal side contain Ba^{2+} to inhibit the apical K^+/NH_4^+ channels. In panel D the luminal side solution have Barium and Furosemide.

3.1.4 Ammonium recycling

A prominent phenomenon observed in simulations that mimic the Watts and Good experiments [21] is ammonium cycling across the apical membrane. This was also observed

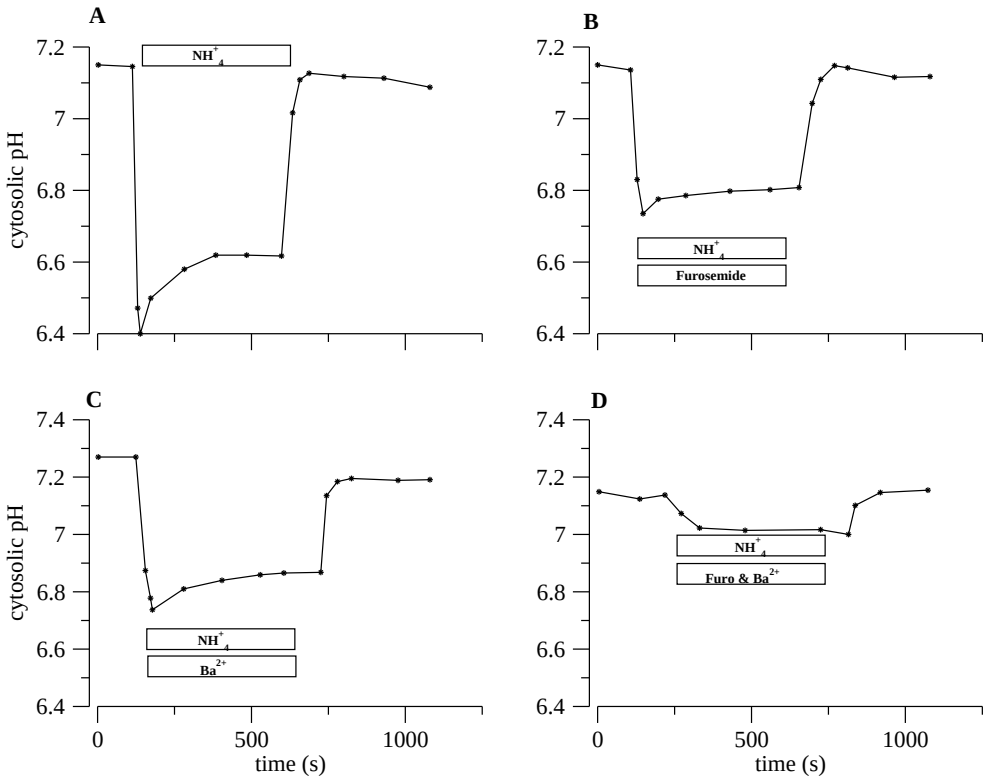

Figure 3.6: Data from Watts' mTAL NH_4^+ perturbation experiments. Data points were extracted from the article [21]

by Weinstein in [10], and consists of NH_4^+ uptake into the cell by NKCC2 and the apical channels, and extrusion via NH3 on the apical side. Since NH_4^+ and K^+ compete for a binding site on NKCC2 [10, 38], NH_4^+ loading implies a reduction in K^+ loading through the NKCC2. Figure 3.7 shows the NKCC2, apical NH3, and apical ammonium electrodiffusion fluxes that correspond to the NH_4^+ pulse simulation in Figure 3.5 panel A. The NH_4^+ cycling is clearly seen in the flux plots (Figure 3.7). NH_4^+ enters the cell via NKCC2 and the apical NH_4^+ channel and exits through the apical NHE3 (positive flux is efflux). The ammonium cycling phenomenon is one of the features of TAL cells that enhances Na^+ transport, since it is a mechanism that prevents K^+ depletion in the lumen. If luminal K^+ depletion were to occur, then NaCl transport would be impaired since the NKCC transporter requires binding by either K^+ or NH_4^+. In a later section, we will use the TAL segment model to

evaluate the effect of NH_4^+ cycling on TAL Na^+ transport.

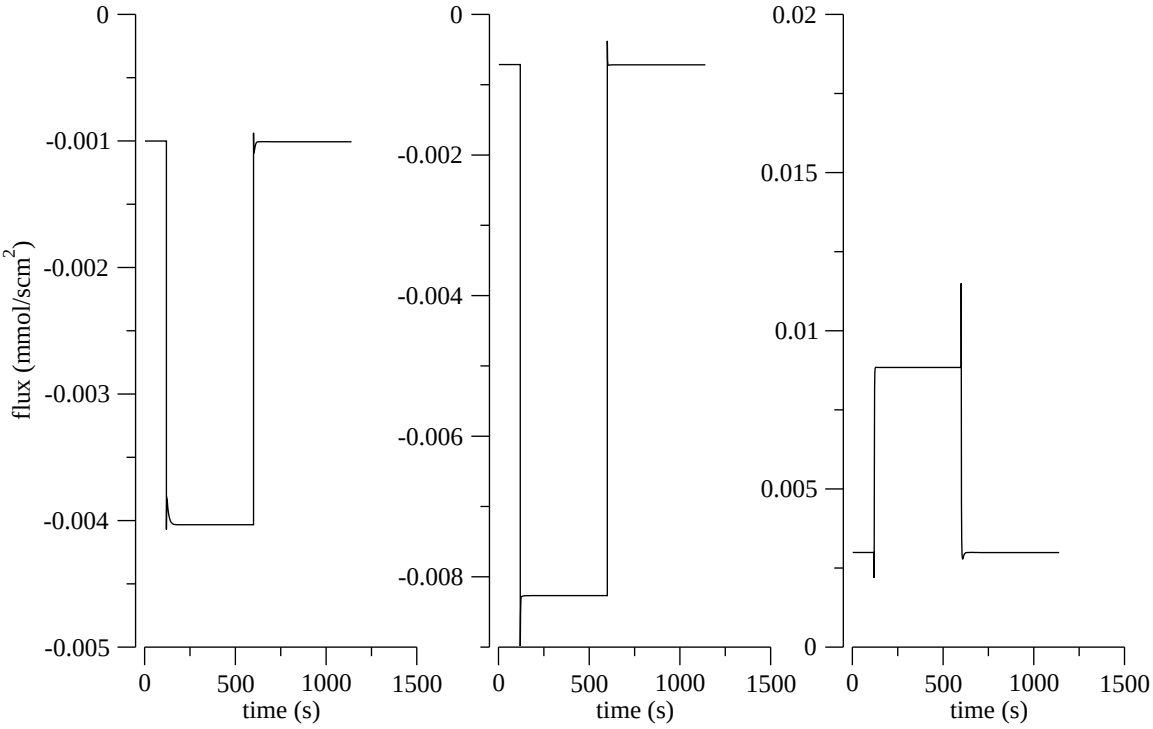

Figure 3.7: NH_4^+ fluxes for simulations, based on experiments by Watts and Good [21]. In all panels luminal [NH_4^+] was increased from 1.6 mM to 20 mM for 8 minutes, and a negative flux is an influx. Panel A is NKCC2 flux. Panel B is apical electrodiffusive flux, and panel C is the apical NH3 flux.

3.1.5 Cell Volume Regulation (CVR)

The main task of TAL cells is to dilute the tubular fluid by solute transport to the interstitium (see Figure 2.2). The chemical composition of the interstitium, as seen in Figure 2.4, presents a varied environment in terms of osmolarity. Ergo, TAL cells face unique challenges to cell volume (CV). Evidence obtained by Kolmosi [56] indicates that rabbit cTAL cells are capable of a regulatory volume decrease (RVD) of up to $\sim$50% in response to cell swelling induced by increased apical Na^+ and Cl^- uptake. In Figure 3.8 we show results from a sequence of luminal [NaCl] step perturbations done to a cell model (equations

(2.3) and (2.4)) configured to be a cTAL cell (86% from the TAL entry). Those perturbations simulate Kolmosi's experiments in cTAL cells, [56]. The normalized cell volume defined for Figure 3.8 is the ratio of cell volume to the steady state cell volume (V_{ss}) of the cell under consideration. The CVR was delayed with a first-order delay in order to relax the assumption that the CVR mechanism of equations (2.16) and (2.17) acts instantaneously. From the figure, we observe that the cell model with CVR mechanism, regardless how much it is delayed (black and blue curve), is able to diminish swelling by $\sim$50% when compared with the cell model without CVR and activities set to match Greger's previously mentioned short-circuit current experiments (green curve). When compared with a cell with no CVR but with NKCC and KCC up regulated (red curve) the swelling is reduced by up to 24%. Such cell volume regulation responses is within Kolmosi's observations in [56] (Kolmosi's data are displayed in Figure 3.8b), and ensures that the CVR mechanism as defined in (2.16) and (2.17) provides reasonable protection against cell swelling. The effect of delaying the CVR response is evident in Figure 3.8. The black curve is the CVR response delayed by 10s while in the blue curve the delay is of 30s. As expected the volume regulation effect is retarded for the blue curve compared with the black curve. Also conspicuous in the figure are the overshoots and undershoots for the CVR cases. The overshoot is the regulatory volume decrease (RVD) produced by CVR, while the undershoot is the cell shrinkage caused by the solute extrusion that happened in the course of the RVD. Those dynamic features, even though they are not as pronounced in Kolmosi's data [56], show that the response is similar to that measured.

Up to this point we have seen that given the appropriate set of parameters, the cell model

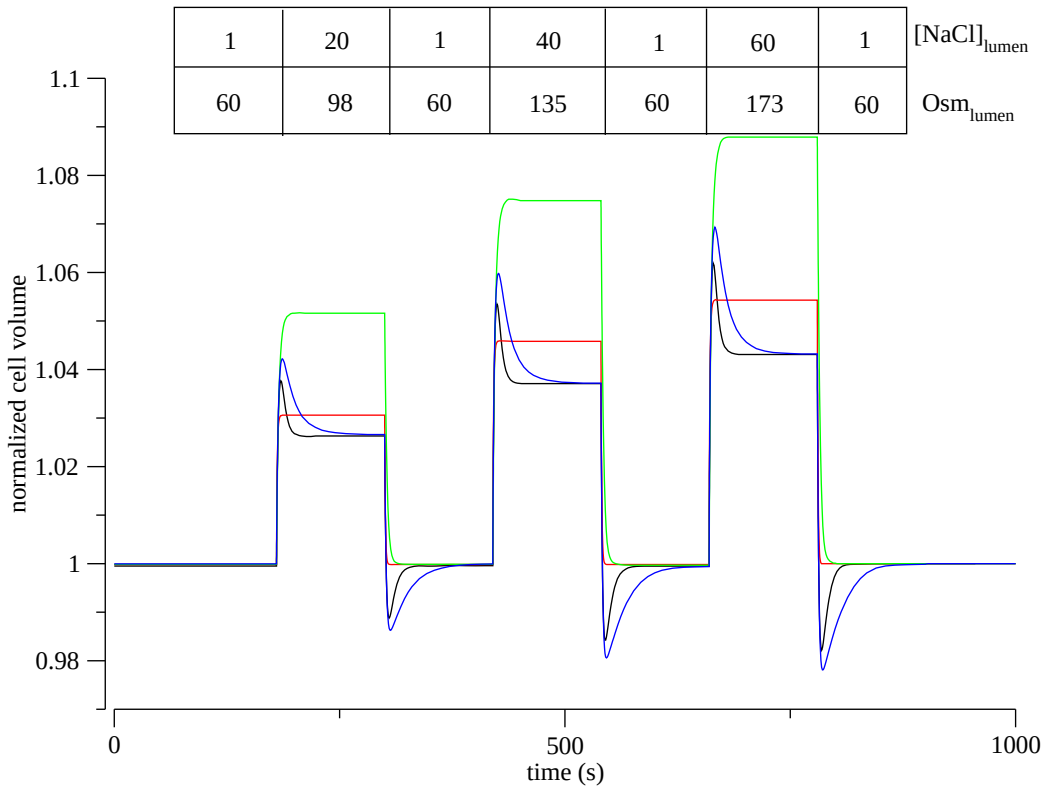

(a) Simulation

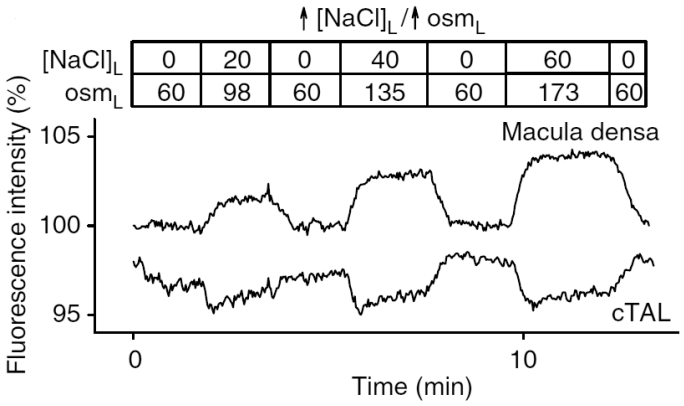

(b) Data from [56]

Figure 3.8: Figure 3.8a is time course of normalized cell volume (V/V_{ss}, where V_{ss} is the steady state volume) after luminal NaCl perturbations, based on experiments by Kolmosi [56]. Simulations were done with a cTAL cell. Black is cell with CVR delayed by 10s; blue is cell with CVR delayed by 30s; red is without CVR but NKCC and KCC up regulated; and green is also without CVR but with NKCC and KCC activities set to yield a short-circuit current close to values measured by Greger's (see Figure 3.2). Figure 3.8b show the results from [56] (reproduced with permission). Note that fluorescense intensity is inversely proportional to cell volume.

as embodied by equations (2.3)-(2.4) and (2.7) with the defined pH buffer representation and cell volume regulation mechanism exhibit the basic electrophysiological properties, the Na^+ transport properties, the NH_4^+ related properties, and the regulatory volume behavior of a living TAL cell. This gives us confidence to examine the transport efficiency issues that are at the core of this work.

3.1.6 Transport efficiency

Transport efficiency is an important issue for TAL cells because they have to transport significant amounts of solute in order to dilute the tubular fluid, and that transport has a transcellular component that involves energy consumption (via Na^+-K^+-ATPase). This is particularly important in the outer medulla of the TAL where O_2 availability is limited by low blood flow. It is thought that TAL cells transport very efficiently owing to paracellular electrodiffusive transport through cation-selective junctions. This depends on the transepithelial chemical gradient, and on the establishment of a positive transepithelial potential. Now, it is also expected that solute transport will reduce or reverse the transepithelial chemical gradient while increasing the electrical driving force for paracellular transport, thus resulting in reduced efficiency. Transport efficiency is defined with the following index:

$$\epsilon \equiv \frac{J^a_{\mathrm{Na}^+} + J^p_{\mathrm{Na}^+}}{J^a_{\mathrm{Na}^+}} = \frac{\text{Net transepithelial Na flux}}{\text{Net transcellular Na flux}}. \tag{3.1}$$

This index ranges from 0 to 2 where 0 means complete backleak (serosa to lumen) through the paracellular pathway while 2 means that for each Na^+ that goes transcellularly, one is positively transported paracellularly from lumen to serosa.

Figure 3.9 shows the results of simulations done with the cell model in which we examine the influence of luminal Na^+ concentration on TAL efficiency. In those simulations,

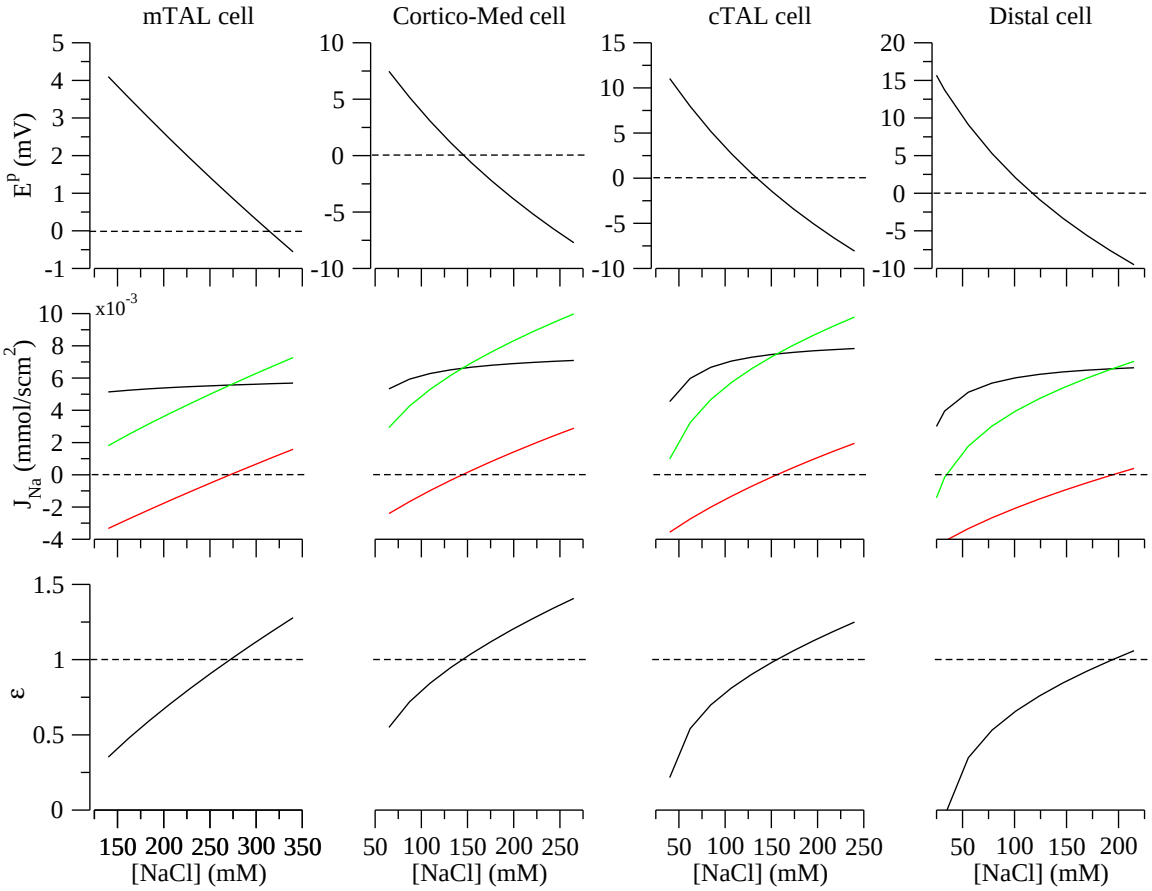

Figure 3.9: First row is transepithelial membrane potential (E^p). Second row has fluxes (J_{Na}), where apical flux is black, paracellular is red, and transepithelial is green with positive flux meaning reabsorption. The third row is the efficiency index (ϵ). All rows are given as a function of NaCl changes in the luminal side of cells at different locations along the TAL segment.

we vary the NaCl concentration on the luminal side of cells at different locations along the TAL. In first row of the figure, we observe the expected decrease in transepithelial potential difference (E^p) as [NaCl] increases. It is notable that E^p changes from positive to negative only at luminal concentrations that the given cell is unlikely to face when embedded in the tubule model. The second row shows net apical, paracellular, and transepithelial Na^+ fluxes. Here positive paracellular flux is from lumen to serosa, and positive apical flux is

from cytosol to the lumen (efflux). Then, for high luminal NaCl, both fluxes favor Na^+ reabsorption (removal from lumen). The third row shows the efficiency indices, and we observe the following: First, under the given conditions, the cell model will not exhibit an efficiency index close to two unless the luminal [NaCl] is increased to a level greater than 350 mM; second, the efficiency index will reach a maximum in the medullary or cortico-medullary region, and afterward the efficiency decreases as we move toward the cortical and distal cortical regions. These results also underline the necessity of using the cell-based tubule model (equations (2.1) to (2.4)) to study transport efficiency issues in the TAL.

3.2 TAL tubule model

Before elucidating efficiency and workload distribution issues at the segmental level, we must verify that the TAL model (equations (2.1)-(2.4) with (2.7)) exhibits the well-known properties of that segment. Taking as initial and boundary conditions the values shown in Table 2.2 and a constant tubular inflow of 6 nL/min (αQ in Table 2.1) we solved the TAL model equations to obtain the steady-state values for the system. Computing the steady-state values shown in Figures 3.10 and 3.11 presents its own computational challenges. The main difficulty is that the Jacobian matrix for the cell model (equations (2.3)-(2.4)) is ill-conditioned. Such ill-conditioning can be shown formally by calculating the Jacobian matrix, evaluating it at an arbitrary stationary point (derivatives are zero), and observing that the column that takes the derivative with respect of volume will have zeros in the majority of its entries with the exception of the entries associated with solutes

affected by cell volume regulation. Moreover, without cell volume regulation that column will be zero and the Jacobian will be singular. Informally, the ill-conditioning is expected since at a stationary point the right-hand side of the cell model does not explicitly show the volume variable. Therefore, the ill-condition of the Jacobian matrix makes the problem of solving for a steady-state of the cell model troublesome for Newton-like methods for solving nonlinear system of equations. This in turn makes finding a steady-state of the tubule model (equations (2.1)-(2.4)) a complicated task. Finding the steady-state of the tubule model implies solving a differential-algebraic system of equations, and in this case, the algebraic part (cell model) is ill-conditioned. The mathematical details of the above arguments are given in appendix B.1.

To work around these issues without resorting to ad hoc rescaling or other techniques [57] or recasting a simplified but less detailed model, we computed the steady-state of the tubule model by solving the model for a "long" interval of time. Here the term "long" time can be estimated with a quantity named steady-state transit time, which is determined by the physical properties of the TAL tubule. In [58] the steady-state transit time is defined as the amount of time that a fluid particle takes to travel the length of the tubule, expresed mathematically as

$$t_{tt} = \frac{\pi r^2 L}{F_w^{\text{typ}}}, \tag{3.2}$$

where F_w^{typ} is the typical water flow into the tubule. For a $F_w^{\text{typ}} = 6$ nL/min, t_{tt} is 18.85 seconds. Having that information, we solve the tubule model for a time span greater than t_{tt} in order to get the steady-state values for the model, including the cellular components which take slightly more time to reach steady-state.

3.2.1 Segmental function

The results of the steady-state computation are in Figures 3.10 and 3.11 for luminal and cytosolic concentrations respectively. In Figure 3.10, a noticeable feature is that a descending gradient of all major solutes is established along the tubule length, with the exception of $H_2PO_4^-$ which increases because of buffering of secreted H^+ by HPO_4^-. Likewise, in spite of the NaCl concentration gradient favoring paracellular backleak, Na^+ is diluted from 250 mM to about 28 mM (see below for details). The pH decreases along the tubule and gets to be slightly acidic when it reaches the end of the TAL owing to the presence of NH_4^+. Also noteworthy are the slight "jumps" in the K^+ and NH_4^+ profiles at certain locations along the tubule. The reasons for the jumps are threefold: first, there is a sharp change in slope of the serosal concentration profile that occurs at the cortico-medullary junction ($x = 0.3$ cm) for most of the tracked solutes (see Figure 2.4) in particular Na^+, K^+, Cl^-, and NH_4^+; second, the change from NKCC2 isoform A to isoform B in the distal cTAL ($x = 0.5$ cm); third, the competition between K^+ and NH_4^+ for loading onto the NKCC2 transporter.

Figure 3.11 shows the steady-state cytosolic concentrations and membrane potentials. We observe the low-Na^+/high-K^+ regime typical of all eukaryotic cells and a pH that is within reasonable bounds. A sharp change in monotonicity is observed for some solutes, in particular H^+. This is attributed to the sharp change in the slope of the interstitial pH at the cortico medullary junction ($x = 0.3$ cm and see Figure 2.4). The apical and basolateral membrane potentials go from $\sim$-75 mV for both at the OM to $\sim$-100 mV and -120 mV respectively at the late cortex. Hence, the transepithelial membrane potential is always positive and increases up to a value of 20 mV at the late cortex. This is important because a

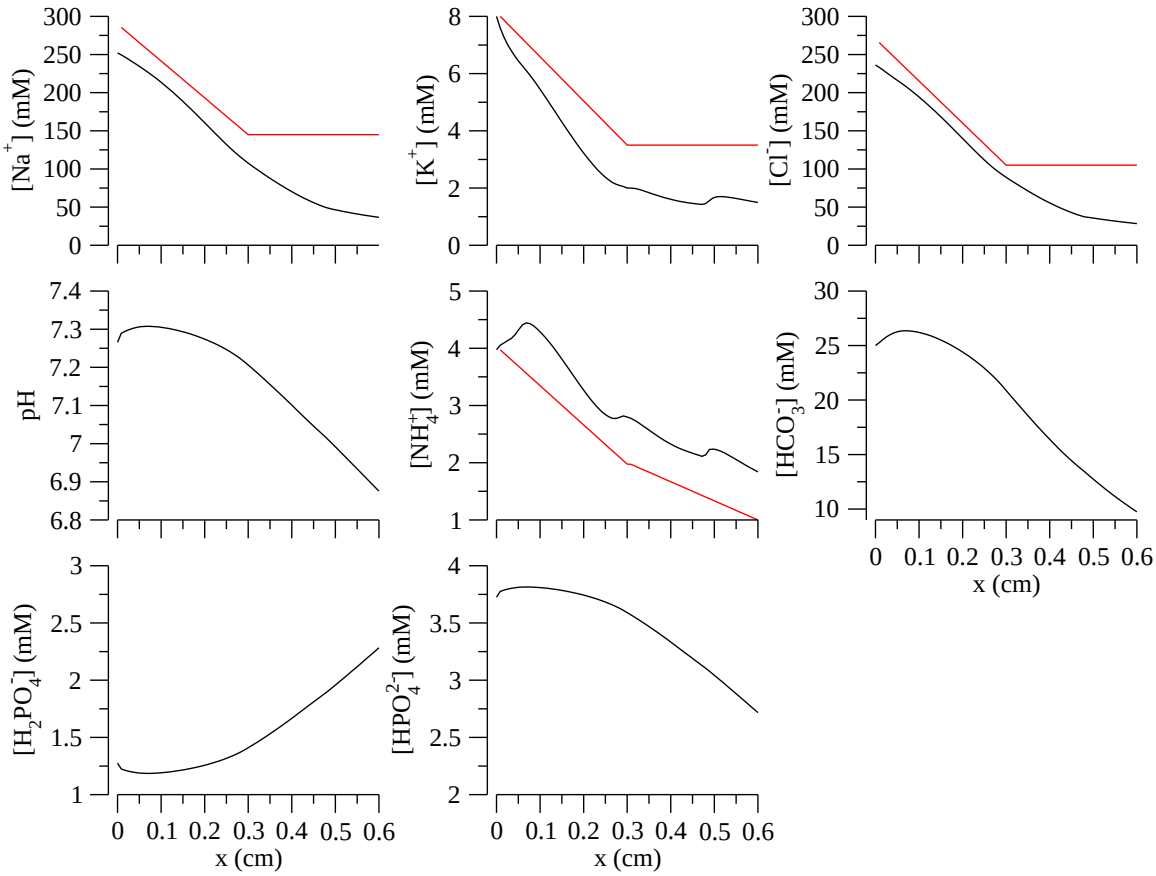

Figure 3.10: Steady-state luminal concentration for major solutes, computed by solving the TAL model (equations (2.1)-(2.4)) with a constant tubular inflow of 6 nL/min. The red line is the interstitial concentration profile.

positive transepithelial potential will favor Na^+ reabsorption, and counteracts the chemical gradient for Na^+ that favors backleak through the tight junctions.

3.2.2 Influence of CVR on TAL function

We assessed the impact of cell volume regulation (CVR) on transport efficiency and workload distribution along the TAL. In all runs, the model's steady-state values were computed at various tubular fluid flow rates with and without CVR. For the case without CVR, the NKCC and KCC activities were fixed at their maximum values. Alternative

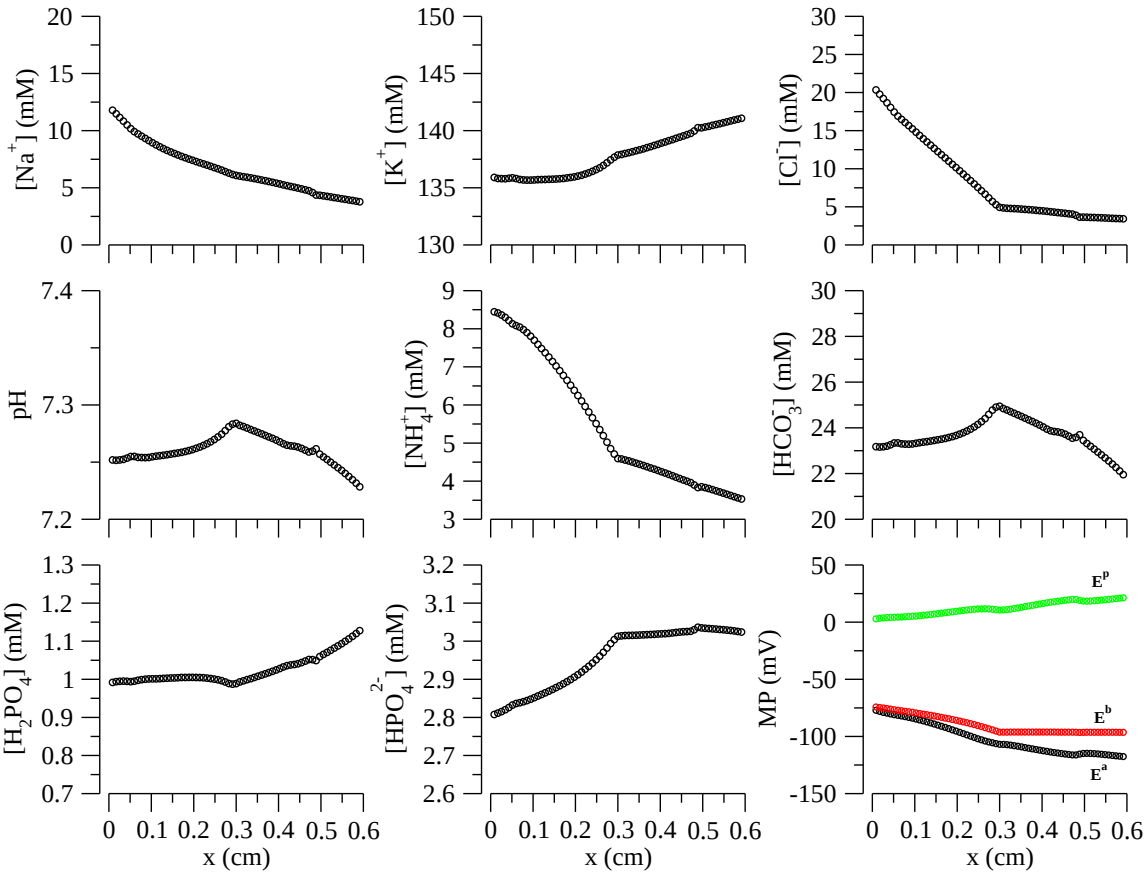

Figure 3.11: Steady-state cytosolic concentration for major solutes, computed by solving the TAL model (equations (2.1)-(2.4)) with a constant tubular inflow of 6 nL/min. Membrane potentials (MP) are shown in the bottom-right corner panel where the apical, basolateral, and transepithelial membrane potentials are the black, red, and green curve respectively.

strategies were tried, with results similar to those shown below, though in some cases either the changes were more subtle or led to failure in diluting the tubular fluid.

Figure 3.12 shows the concentration profiles for Na^+, Cl^-, and K^+ at three flows; the blue dotted line is the corresponding fixed interstitium concentration profile. At baseline flow (6 nL/min), the TAL model with CVR predicts concentration profiles for Na^+ and Cl^- that indicate that reabsorption is distributed such that there is substantial dilution in the cortex, while at low flow the majority of the transport occurs in the medulla and luminal concentrations approach static head, that is, when net transport is zero. At high flows, the

Na^+ and Cl^- profiles rise all along the TAL. Most of the K^+ is reabsorbed in the medulla, and the same holds for the NH_4^+. Without CVR, most of the transport shifts to the medulla and the concentration profiles are relatively flat in the cortex, except at the highest flow. Therefore the figure illustrates that CVR responses, in fact, distributes work among all of the individual TAL cells, and helps establish an axial Cl^- gradient consistent with measured TGF gain values [59, 60, 61].

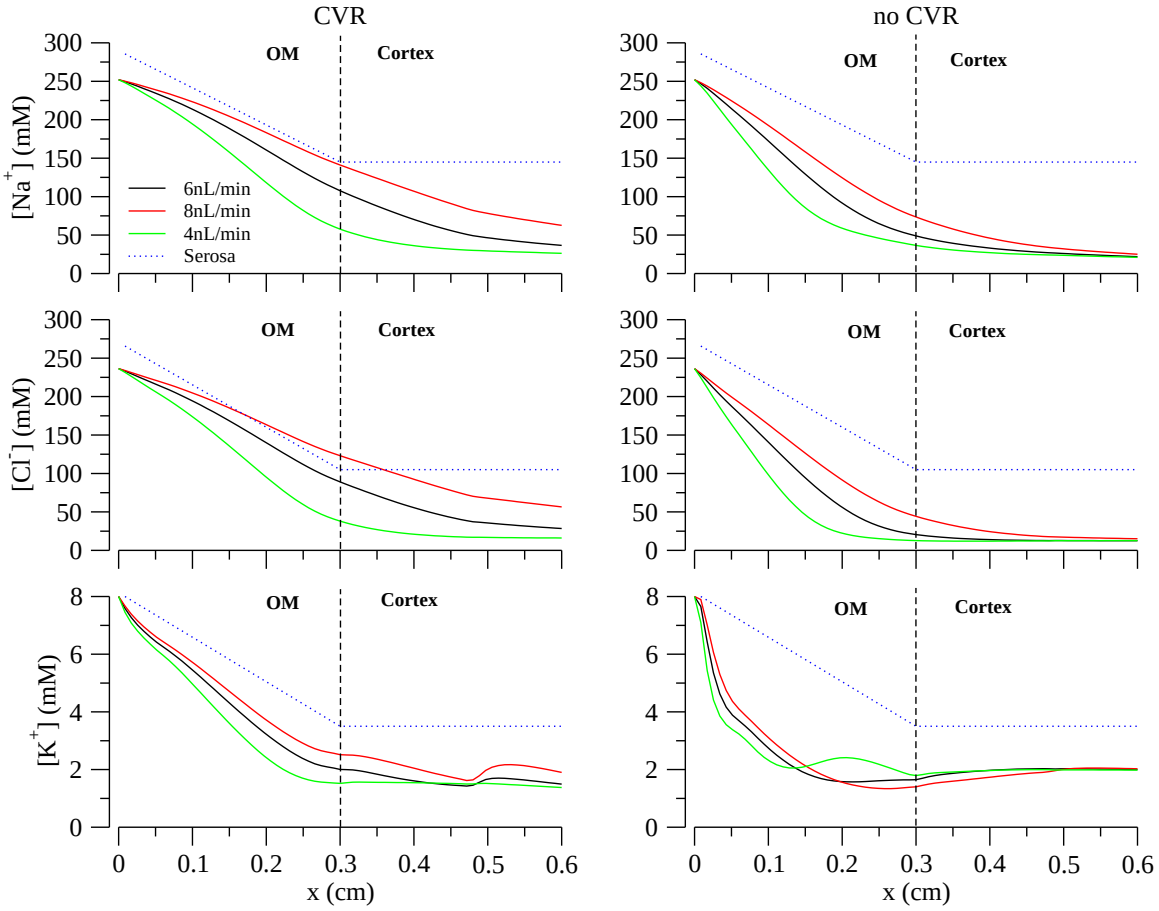

Figure 3.12: Steady-state luminal concentration for major solutes, computed by solving the TAL model (equations (2.1)-(2.4)) with a constant tubular inflow. The black solid curve denotes an inflow of 6 nL/min, the red an inflow of 8 nL/min, the green an inflow of 4nL/min, and the blue dotted line is the fixed serosal concentration profile.

The graphs at Figure 3.13 illustrate the influence of cell volume regulation on TAL effluent ion composition. With CVR, the flow-dependence of Na^+, Cl^-, and K^+ is compa-

rable to measurements by Vallon and coworkers in [26]. Without CVR, the slopes of the outflow curves are reduced because the slopes of the concentration profiles in the cTAL (see Figure 3.12) are small in magnitude. Hence, CVR responses in part explain the observed dependency of effluent ion composition on tubular fluid inflow. It is noteworthy that, in essence, a self-organization process that raises transport efficiency emerges from the CVR responses in the ensemble of TAL cells. In addition it also ensures that the TGF system gain is high.

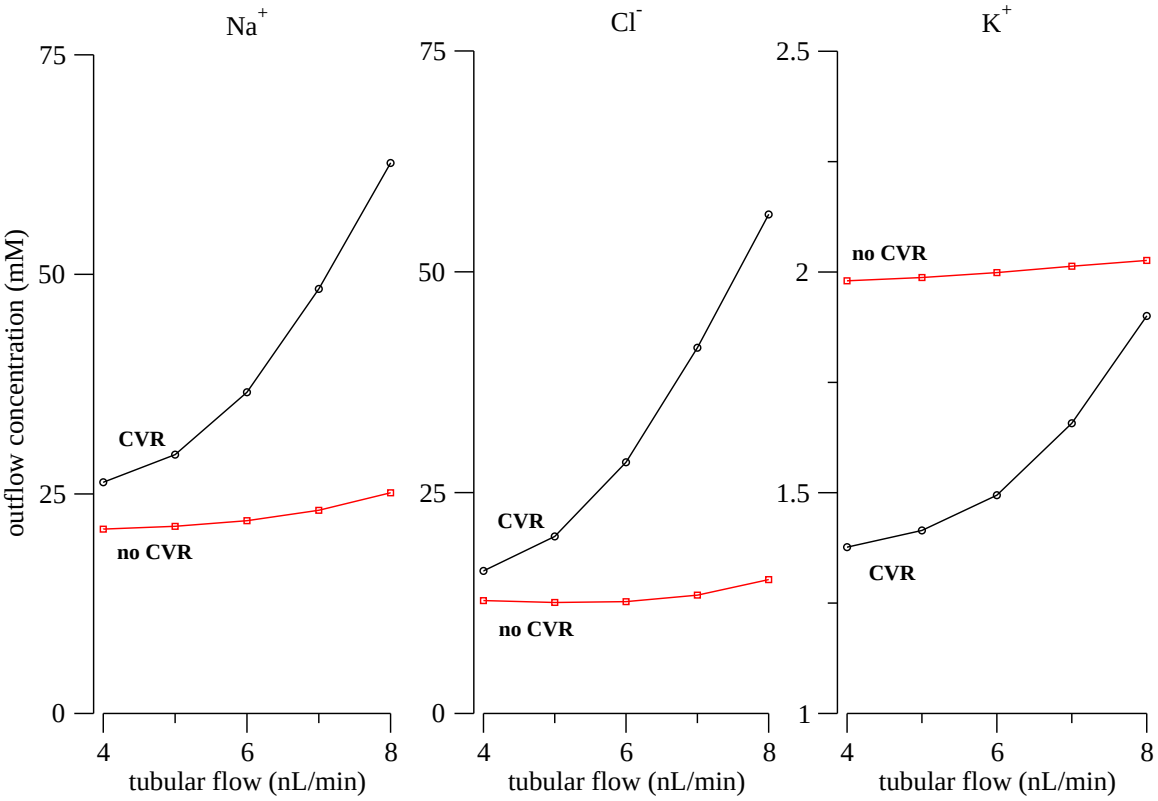

Figure 3.13: Steady-state outflow for major solutes, computed by solving the TAL model (equations (2.1)-(2.4)) with a constant tubular inflow. The black circles denote CVR, and red squares no CVR enabled.

Figure 3.14 displays cell volume for a baseline flow of 6 nL/min. Cell volume is well controlled except for the distal part of the cTAL where the luminal fluid becomes very dilute. Without CVR, cell volume falls along the TAL segment, owing to the lower luminal

Na^+ and Cl^- concentrations.

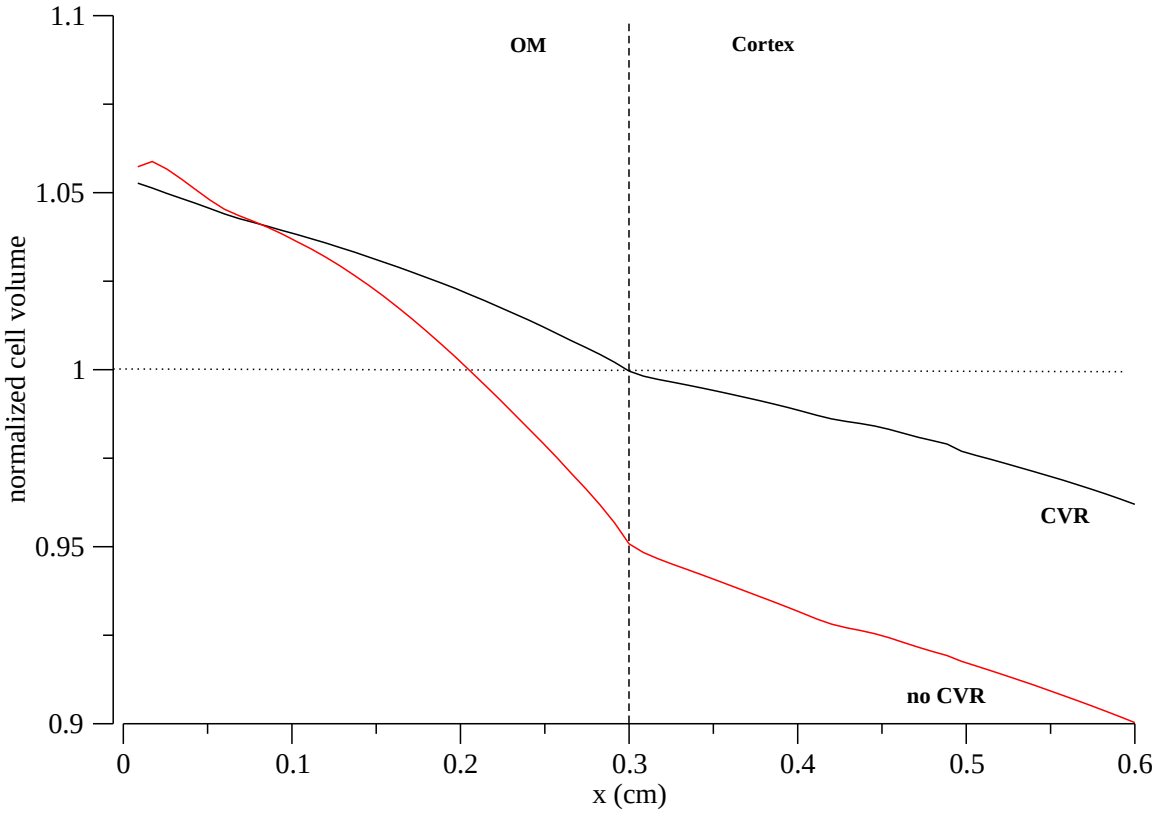

Figure 3.14: Steady-state volume, computed by solving the TAL model (equations (2.1)-(2.4)) with a constant tubular inflow of 6 nL/min. The black line denote CVR, and red line is for no CVR enabled.

3.2.3 Cell volume regulation & transport efficiency

Figure 3.15 illustrates how the efficiency of sodium transport varies along the TAL. After reaching its peak in the outer medulla, the efficiency falls as paracellular transport reverses. The lower efficiency in the absence of CVR is a consequence of the greater dilution of the tubular fluid. Also the jumps in the curves at the cortex results from the transition from isoform A to B of the NKCC2 transporter. Three things are noteworthy: First, as anticipated by the efficiency results on Figure 3.9, the efficiency does not monotonically

decrease from the outer medullary region to the late cortex, but it reaches a maximum before crossing the cortico-medullary junction. The location of the maximum is determined by the location of maximum paracellular flux which depends on the transepithelial concentration and membrane potential differences as well as the tubular flow rate. Second, the efficiency with no CVR rises to a greater value than the CVR case, but only for a fraction of the outer medullary part of the tubule. This is caused by an increase in paracellular transport driven by the rise in transepithelial potential difference that is a consequence of the increased NKCC2 uptake, since it is set to its maximum, and passive apical K^+ and NH_4^+ backleak. Third, the efficiency does not rise to the maximum permitted value, of 2. This means that either the system is not as efficient as suspected or, that although CVR as defined in this work increases the efficiency, it needs to act in conjunction with other intracellular or intranephron regulatory systems in order to increase the driving force for paracellular electrodiffusion (positive membrane potential) and thereby increase the efficiency even more. A regulatory system that might act synergystically with cell volume regulation to improve the efficiency index along the TAL is the tubuloglomerular feedback system (TGF). This possibility is explored below.

In the previous section, using the cell model, we showed how the presence of ammonium in the TAL lumen coupled with the expression of the NKCC2 gives rise to NH_4^+ cycling. To determine the impact of NH_4^+ cycling on efficiency and on the dilution capacity of the TAL, we computed the steady-state concentration profiles and the efficiency index for the tubule model with and without NH_4^+ cycling impaired. In Figure 3.16, black represents the baseline case in terms of NH_4^+ levels and NKCC2 as already shown in Figure 3.10;

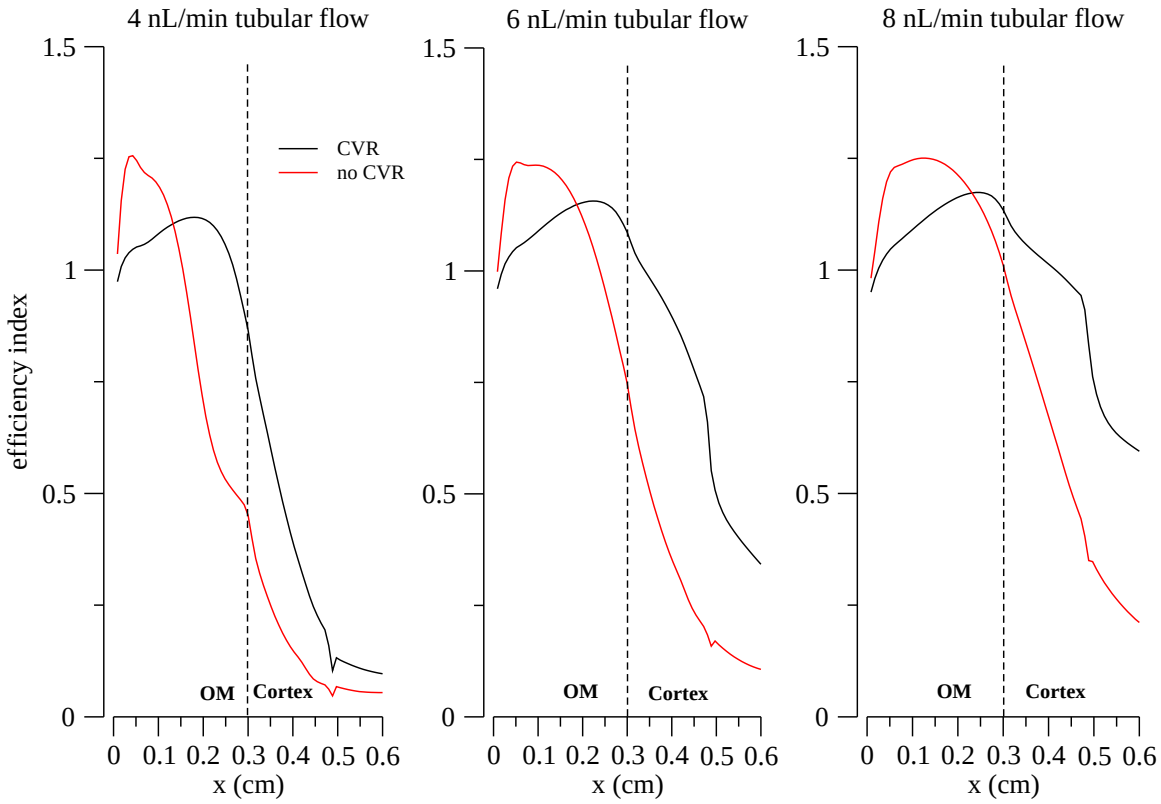

Figure 3.15: Efficiency index as defined in 3.1. It was computed by solving the TAL model (equations (2.1)-(2.4)) with different constant tubular inflows. The black line denote CVR, and red line is for no CVR enabled.

red represents usage of NKCC1, instead of NKCC2 hence hampering, but not completely abolishing NH_4^+ cycling (see Figure 3.7); and green represent the case in which NH_4^+ in all compartments was reduced to low levels (10^{-6} mM). We learn from Figure 3.16 panel A that, with low NH_4^+ in the lumen, cytosol, and serosa the diluting ability of the TAL is greatly diminished. In this case the Na^+ profile (green line) stays above 125 mM. Eliminating NKCC as an NH_4^+ uptake pathway (red line) also reduces the dilution but not as dramatically as in the previous case (outflow just above 50 mM). Panel B shows that the reward for poor diluting ability is higher efficiency which just reflects the higher luminal Na^+ concentration. There, although we observe the same trend for efficiency that were pointed out before (Figure 3.15), the cases in which NH_4^+ cycling was impaired have a higher effi-

ciency in the OM. This result was unexpected at first, but its origin is revealed in panel C. Panel C shows Na^+ fluxes along the tubule with the solid lines representing apical fluxes, and asterisked lines are paracellular fluxes with positive flux meaning reabsorption (lumen to serosa). From this panel and from the definition of the efficiency index (equation (3.1)), the higher efficiency for the diminished NH_4^+ cycling cases is explained by a reduction of the net apical flux. In other words, when the cycling is reduced, the transcellular and paracellular fluxes are closer to one another (in the norm-2 sense). This increases the efficiency, but at the expense of reducing the transcellular transport rather than increasing paracellular transport, and this ultimately leads to poor tubular fluid dilution. The possibility that this presents is that it may not be feasible to have an highly efficient TAL, in terms of paracellular versus transcellular transport, without sacrificing diluting ability. That is, unless other TAL control systems, like TGF, play a role increasing the paracellular reabsorption.

3.3 Dynamic properties of the TAL

Before elucidating the impact of the TGF system on workload distribution and efficiency of transport, it is important to verify that our TAL model exhibits filtering properties similar to observations by other investigators [42]. To accomplish this, we use a sinusoidal forcing as the tubular water flow function, equation (2.19), and compare the impact of the predicted concentrations profiles along the TAL with those obtained by Layton, et al. [42]. Applying an oscillatory forcing is a useful means to examine the dynamical features of the TAL because the TGF system (see below), which controls the tubular fluid inflow into the

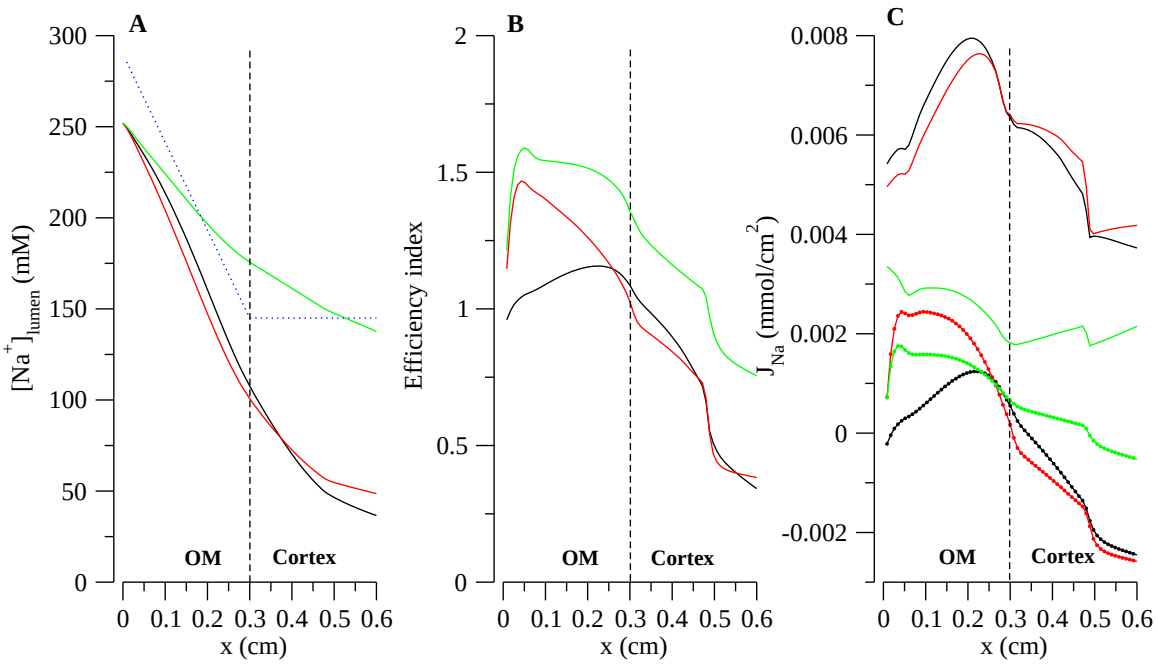

Figure 3.16: In panel A, the blue dotted line is the serosal concentration profile. In all panels: black is for the case with NKCC2 and normal NH_4^+ levels, red is for NKCC1 and normal NH_4^+ levels, and green is for NKCC2 and low levels of NH_4^+. In panel C, solid lines are for apical fluxes and asterisks for paracellular fluxes with a positive flux being a reabsorptive flux.

TAL segment, often oscillates. Since our TAL model also tracks what is happening in the cytosol, we are also able to see the impact of the forcing on cytosolic composition.

Figure 3.17 shows the luminal and cytosolic concentration profiles along the tubule for tubular inflow given by the sinusoidal forcing described above with frequency $f = 1/(2t_{tt})$ Hz, and amplitude $\eta = 3$ nL/min at different times. The times are multiples of the sinusoidal period, so the depicted curves are at times $0p$, $0.25p$,$0.5p$, p where $p = 2t_{tt}$ (black, red, green, blue, and magenta, respectively). On the luminal side for Cl^- we observe what the authors in [42] pointed out. Low frequency $(1/(2t_{tt}))$ forcing induces large excursions in macula densa concentrations (end of TAL, $x = 0.6$ cm) as well as in other locations along the segment, but with monotonically decreasing profiles along the

TAL. The magnitude of the excursion, or spread of the concentration profile, is tied to the harmonic structure of the TAL (see below and [42]) but in general, as seen in the figure, the range depends on the solute's transit time to a given location. Also remarkable are the relatively small excursions, with respect to time, in the luminal concentrations of K^+ and NH_4^+ and in the cytosolic concentrations. The small luminal excursion of K^+ and NH_4^+ concentrations reflects the effects of apical membrane cycling. The small cytosolic variation is a consequence of the transcellular transport regulation mechanisms. Moreover, this underlines the ability of the cells to mantain homeostasis in spite of the composition changes in the lumen.

In Figure 3.18, the luminal and cytosolic concentration profiles at different times along the tubule are displayed for the same sinusoidal forcing but with frequency $f = 4/(t_{tt})$ Hz. As observed in [62], the range of the excursions of Cl^- concentration at the macula densa is smaller when compared with the low frequency forcing (Figure 3.17). This finding indicates that the TAL acts as a low pass filter. Likewise, the emergence of standing waves in Na^+ and Cl^- are unmistakable. Five nodes, located at $x = 0, 0.15, 0.3, 0.45, 0.6$, are visible for the luminal concentration profiles of Na^+ and Cl^-. The nodes are not so definitive for K^+ and NH_4^+, this being a consequence of apical membrane cycling (see below). Akin to what was observed for the low frequency case, the cytosolic concentration are not significantly perturbed by the oscillations in luminal concentrations.

Figure 3.19 shows the ranges of excursions in $[Cl^-]$ at the end of the tubule ($x = L$) as a function of the frequency of the sinusoidal forcing (after the oscillations are fully developed). Note that the magnitude of the excursion generally has a decreasing trend with

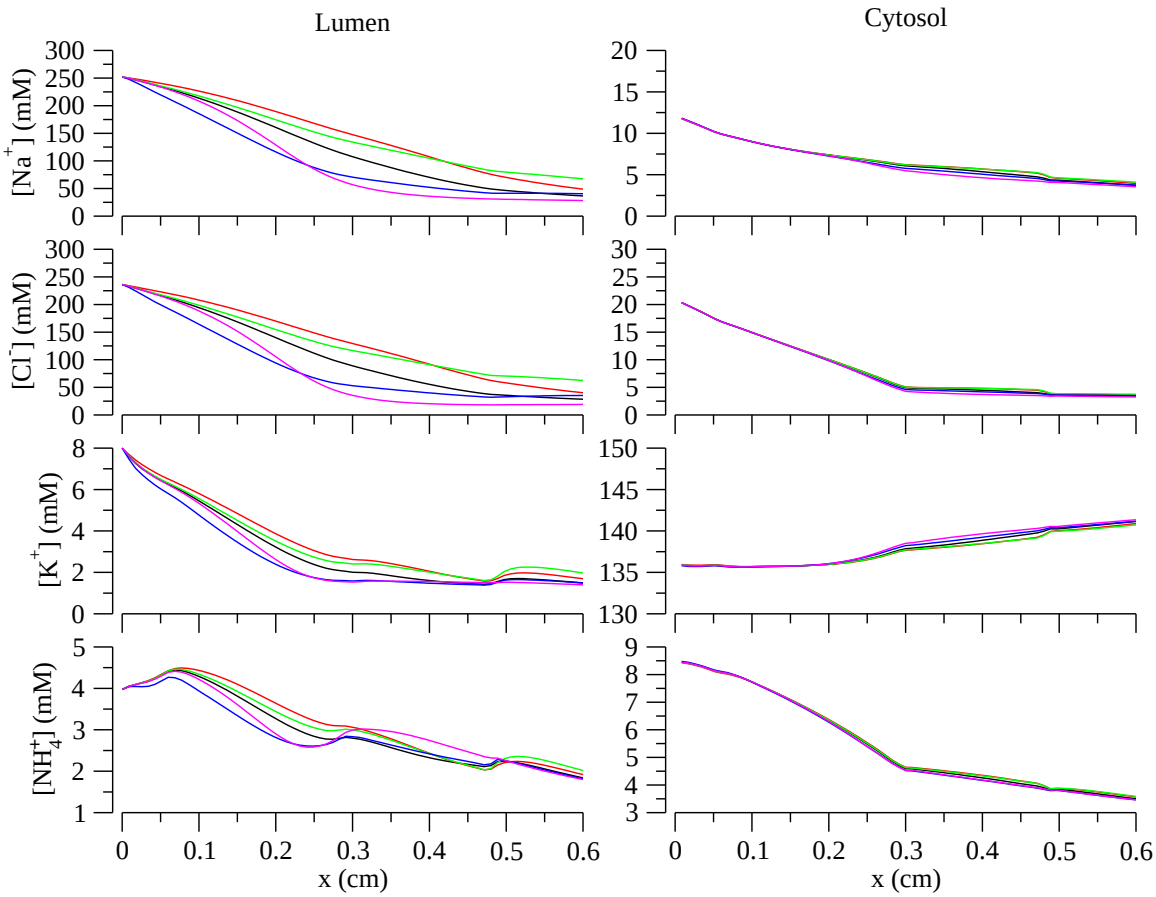

Figure 3.17: Luminal and cytosolic concentration profiles along the tubule when the sinusoidal forcing given by equation (2.19) with $f = 1/(2t_{tt})$ Hz, and $\eta = 3$ nL/min is the input flow. This is given at different times where the times are multiples of the sinusoidal period (p), so the colors of depicted curves which are black, red, green, blue, and magenta correspond to times $0p$, $0.25p$, $0.5p$, p respectively.

frequency. However, local optima appear in the magnitude of the range when the forcing has specific frequencies (see Table 3.3). In [62, 42] the frequencies at which the sinusoidal flow has a transit time close to the steady-state transit time (t_{tt}) are the frequencies that minimize the Cl^- concentration excursions at the macula densa. Those frequencies depend on t_{tt} and therefore provide an explaination for the harmonic structure of the Cl^- waveform in the TAL in terms of it. Also, in [62] the Cl^- backleak in the cortical region of the TAL was predicted to increase the magnitude of the Cl^- excursions at the macula densa. It is precisely this that makes the nodal structure less apparent for our model (cf. Figure

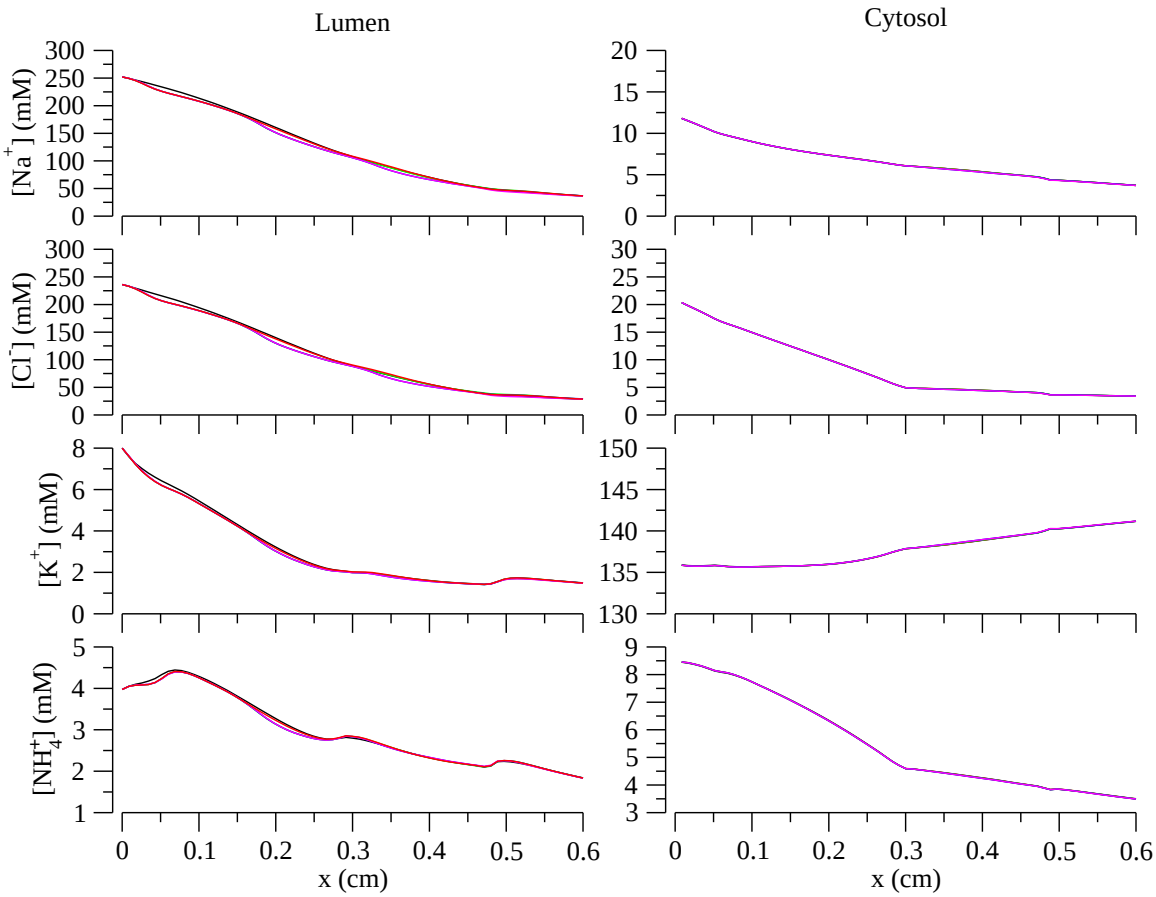

Figure 3.18: Luminal and cytosolic concentration profiles along the tubule when the sinusoidal forcing given by equation (2.19) with $f = 4/(t_{tt})$ Hz, and $\eta = 0.5(6)$ nL/min is the input flow. This is given at different times where the times are multiples of the sinusoidal period (p), so the colors of depicted curves which are black, red, green, blue, and magenta correspond to times $0p$, p, $2p$, $3p$ $4p$ respectively.

3.19 with Figure one in [62] and reproduced here as an inset of 3.19). It is also clear that compared with [62], the magnitude of the excursions at the macula densa is less symmetric. Specifically, at low frequencies the excursions shift toward higher Cl^- concentrations. This implies that the TAL distorts the Cl^- waveform introduced by oscillating tubular input water flow yielding an apparent excursion at higher flows longer than at lower flows. Square wave forcing is potentially more feasible to apply in an experimental setup. Therefore, for the sake of completeness, we show in Figure 3.20a the luminal and cytosolic profiles along the tubule for the open loop (no TGF) square wave forcing given by equation (2.20) with

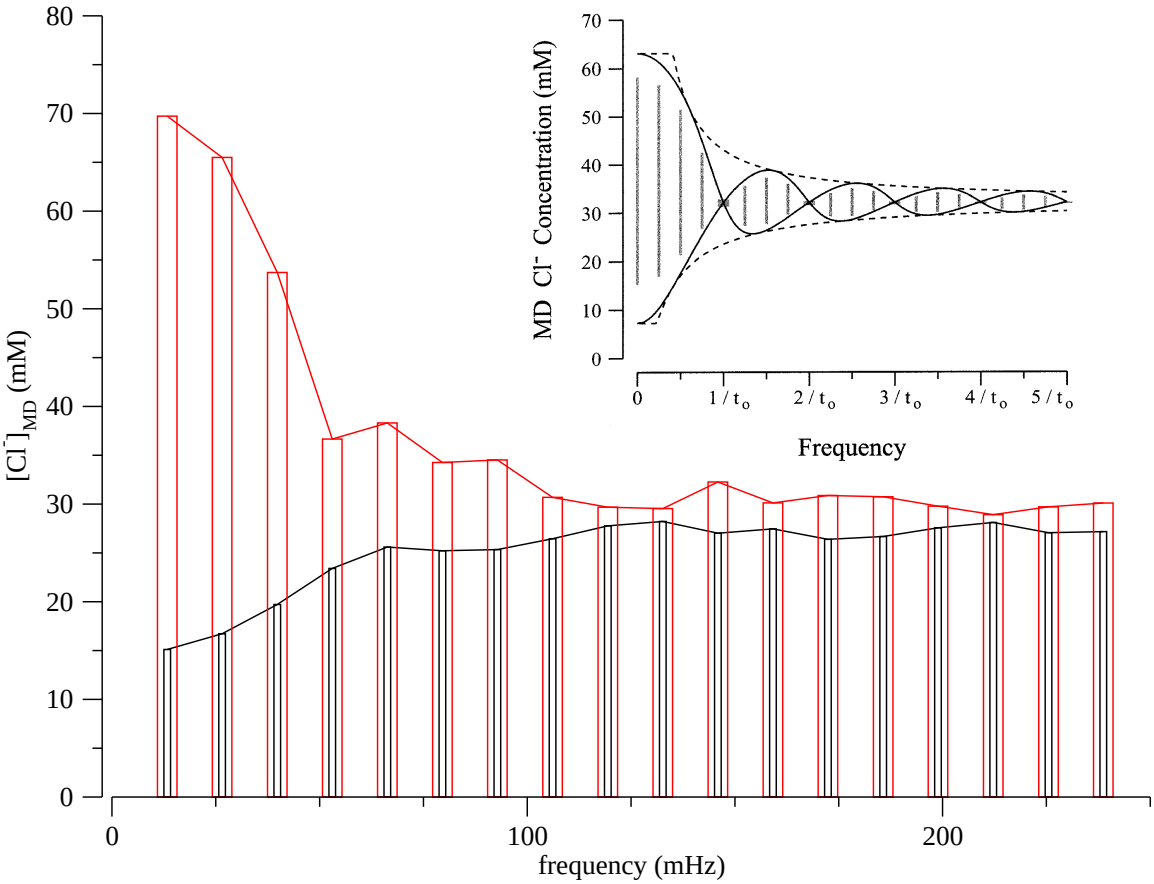

Figure 3.19: Range of luminal Cl^- excursions at the end of the TAL ($x = L$), as a function of the frequency of the sinusoidal forcing applied to the tubular inflow. The Figure inset is Figure one in [62] where t_o is the steady-state transit time ($\sim$15 s) for the model used in [62]. The inset is reproduced with permission of the American Physiological Society.

Table 3.3: Magnitude of Cl^- excursion range at MD.

factor of $1/t_{tt}$	frequency (mHz)	$\lvert\Delta C\rvert$ (mM)	is LO?[c]
0.25	13.3	54.6230	
0.5	26.525	47.7823	
0.75	39.8	33.993	
1	53.05	13.2436	
1.25	66.3	6.1702	$\star$
1.5	79.576	9.0385	
1.75	92.8	9.1847	$\star$
2	106.1	4.2334	
2.25	119.4	1.9125	
2.5	132.63	1.6649	$\star$
2.75	145.9	2.7363	
3	159.15	3.0449	
3.25	172.4	4.4926	$\star$
3.5	185.7	4.0659	
3.75	198.9	2.2205	
4	212.2	0.8032	$\star$
4.25	225.5	2.6547	
4.5	238.7	2.9368	

[a] Forcing frequencies are multiples of t_{tt}^{-1}.
[b] Magnitude of the range.
[c] Is the given frequency a local optimum (LO) for the range's magnitude?

$f = 0.5/t_{tt}$ Hz and $\eta = 0.6$ nL/min. The results turns out to be an amplification of the effects seen in Figure 3.17. The same holds for the forcing with frequency $f = 2/t_{tt}$, which is shown in Figure 3.20b, with respect of Figure 3.18.

We now move on to incorporating the TGF response into the TAL system, inasmuch as we have showed in our model that the ranges of solute excursions along the segment depend on the frequency of an oscillatory forcing and at a more fundamental level, on the solute transit time.

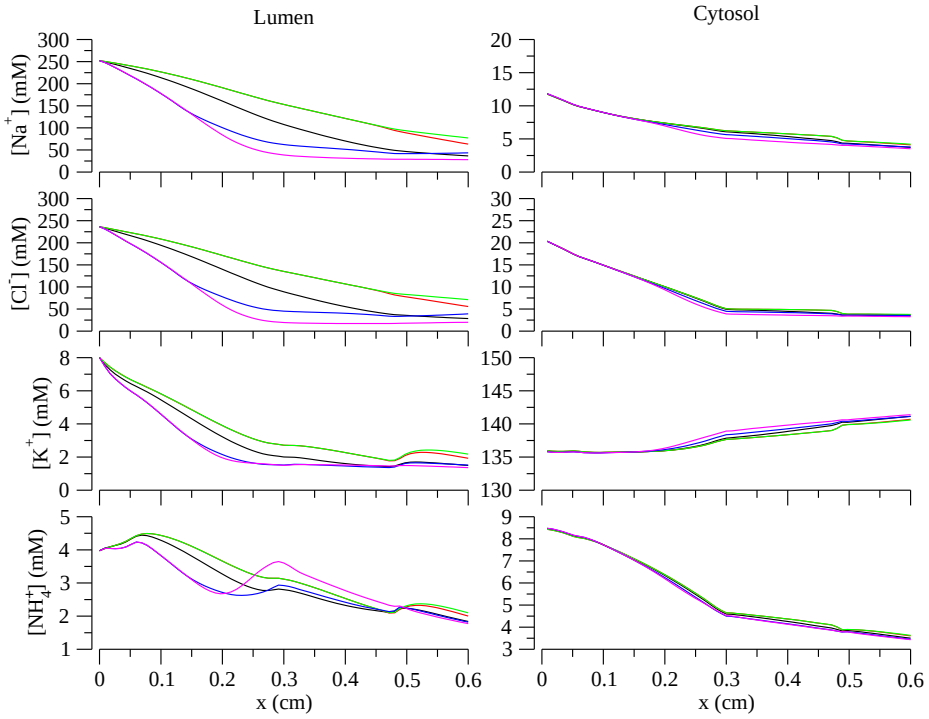

(a) Low frequency

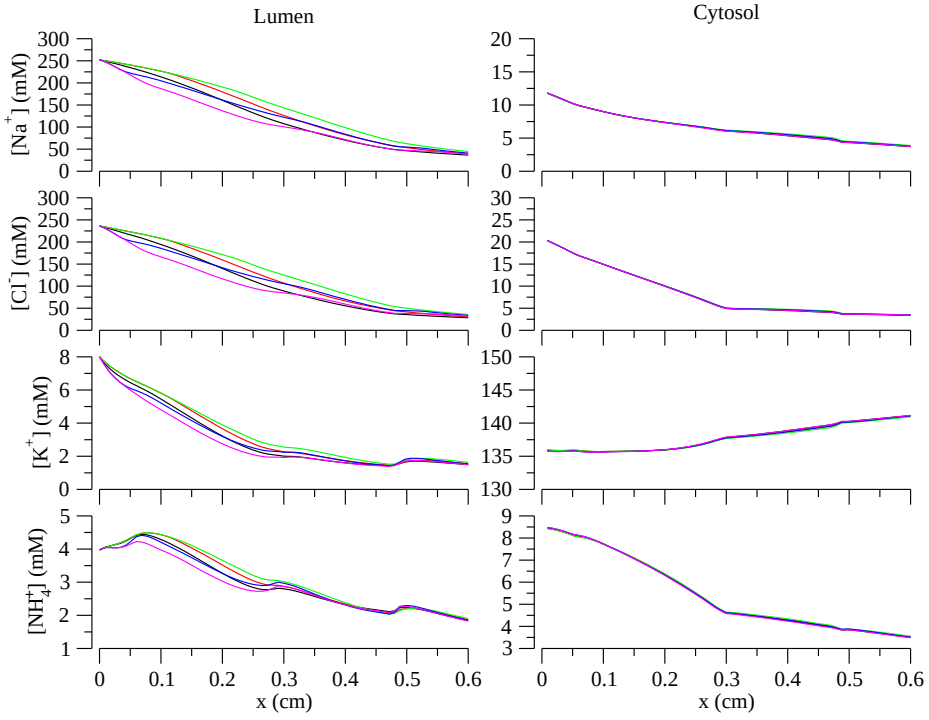

(b) High frequency

Figure 3.20: Luminal and cytosolic concentration profiles along the tubule when the square wave forcing given by equation (2.20) with $f = 1/(2t_{tt})$ Hz for Figure 3.20a and $f = 2/(t_{tt})$ Hz for Figure 3.20b and $\eta = 3$ nL/min is the input flow. This is given at different times where the times are multiples of the square wave period, so the colors of depicted curves which are black, red, green, blue, and magenta correspond to times $0p$, $0.25p$, $0.5p$, p respectively.

3.4 TAL tubule model with TGF system

3.4.1 TAL-TGF system: transport efficiency

In the previous section we showed (Figure 3.12) that cell volume regulation (CVR) responses are important in establishing an axial chloride gradient sufficient to generate TGF gain values similar to measurements in [59, 60, 61], and typical flow dependencies of TAL Na^+ transport (Figure 3.13). But we also show that, if the TAL is indeed a highly efficient solute transport system, then CVR has to act synergystically with other intracellular or intranephron control systems in order to raise the efficiency. Motivated by this, we decided to add the TGF loop, equations (2.22)-(2.24), to the TAL model, equations (2.1)-(2.4), and study the impact of this intranephron reflex in distribution of transport and efficiency along the length of the TAL. For the set of parameters for the TGF system in Table 2.4, Figure 3.21 panel A shows the tubular function, that is, the $[Cl^-]$ vs. single-nephron glomerular filtration rate (SNGFR) relationship, that generates the TGF error signal. Panel B shows the feedback function incarnated by equations (2.22)-(2.24).

Similar to the tubular function in [9] and shown in Figure 1.2 panel B of the present work, panel A shows that the TAL does not maximally reduce tubular fluid Cl^- concentration. Rather, at its operating point the TGF system regulates outflow to a level above the point at which the slope of the curve goes to to zero because of solute backleak. Furthermore, we observe for our model that at very low filtration rates the Cl^- concentration rises slightly. This is caused by marked backleak, serosa to lumen electrodiffusive flux, driven

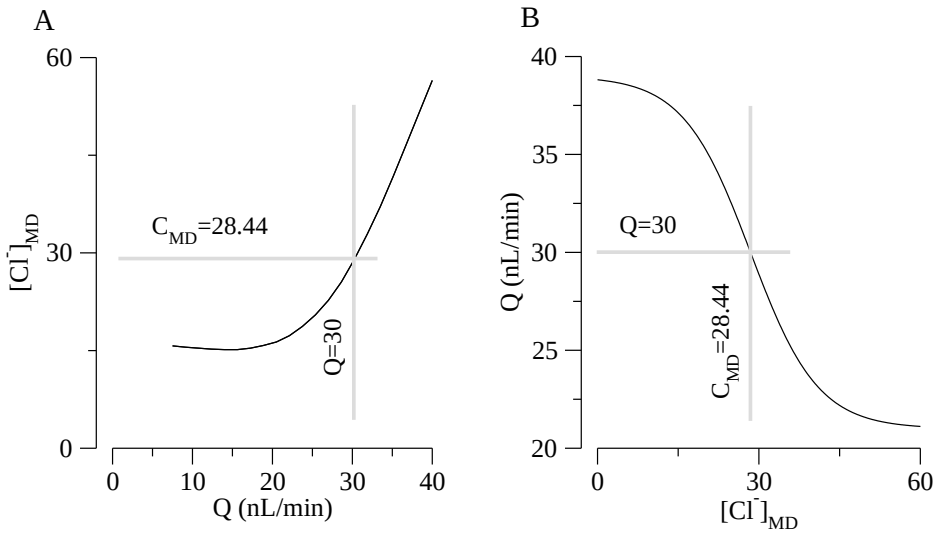

Figure 3.21: (A) Tubular function: this relationship generates the sensed error signal. (B) Feedback function: effect of MD [Cl^-] (C_{MD}) on nephron glomerular filtration rate (Q). The gray lines show values for a typical operating point. Curves are from our model (see chapter 2) and based on studies in [9].

by low luminal concentrations and large transepithelial concentration difference (luminal Cl^- 15 mM vis-à-vis serosal Cl^- of 100 mM).

One of the most fascinating characteristics of the TAL-TGF system is the presence of sustained oscillations in key variables like tubular fluid flow and early distal Cl^- concentration. This has been shown experimentally by Holstein-Rathlou [63] and has also been explained by modeling studies in [9], where the authors showed the existence of a Hopf bifurcation. Ergo, they demonstrated that the TAL-TGF system has a stationary state that bifurcates from steady-state or sink, to a limit cycle and a source after a small perturbation of the following key TGF parameters:

$$\tau = \tau_d + \tau_p \tag{3.3}$$

$$\gamma = \left(\frac{\Delta Q}{\alpha Q_{op}}\right)\left(\frac{kC_{bnd}}{2}\right)\left(\frac{L}{C_{bnd}}\right)\left(\frac{dC^a_{\mathrm{Cl}^-}}{dx}\Big|_{x=L}\right) \tag{3.4}$$

where $C_{bnd} = C^a_{Cl^-}(0,t)$, and the space derivative is time independent because it is the

steady-state value. This finding explained the spontaneous appearance of sustained oscillation that is observed experimentally. Moreover, these results are important for our work because, as seen on Figure 3.12 and 3.15, the efficiency of transport as well as the workload distribution exhibit a dependence on tubular flow rate (hence in transit time, t_{tt}).

Figure 3.22 shows the results from a simulation that mimics experiments that perturbed the SNGFR by introducing fluid in the tubule with a pipette. Simulations of that sort were done in [9] and consist of driving the system close to steady-state and doing a step-increase on tubular flow rate. The step flow is 1% of SNGFR (Q) and has a duration of t_{tt}. Panels A and C are what we call the low gain case while panels B and D are the high gain case. Mathematically, the distinction comes from the fact that the value of the TGF sensitivity, k, and therefore the composite parameter γ for the low gain case is less than for the high gain case.

Observe that in the low gain case (panels A and C in Figure 3.22) after the perturbation in tubular flow, the system oscillates but slowly returns to the steady-state (damped oscillations). On the other hand for the high gain case, the perturbation is followed by oscillations that are amplified until reaching a maximum amplitude and with a frequency of 30 mHz. These results are akin to the ones in [9] and are explained by their bifurcation analysis, albeit the values of k and γ for the bifurcation loci are not the same. The change in k and therefore in γ induces a sign change in the real part of a complex conjugate pair of eigenvalues that make the stable steady-state (panel A and C) bifurcate to a limit cycle and a unstable stationary point (panel B and D). The difference in our results and the results in [9] are in the values of γ that define the boundary between negative and positive real parts

of the conjugate eigenvalues. Such a difference is not surprising since the analytical bifurcation diagram in [9] was shown to be shifted when backleak was included in their model. Therefore, it is not surprising that the values of γ that, for a given delay τ, bifurcate the system are different for our model, which includes the backleak of several solutes. Also the differences stem from the fact that their transmural transport is modeled exclusively with a Michelis-Menten type of transport and diffusion, and that the length of their tubule is shorter (0.5 cm).

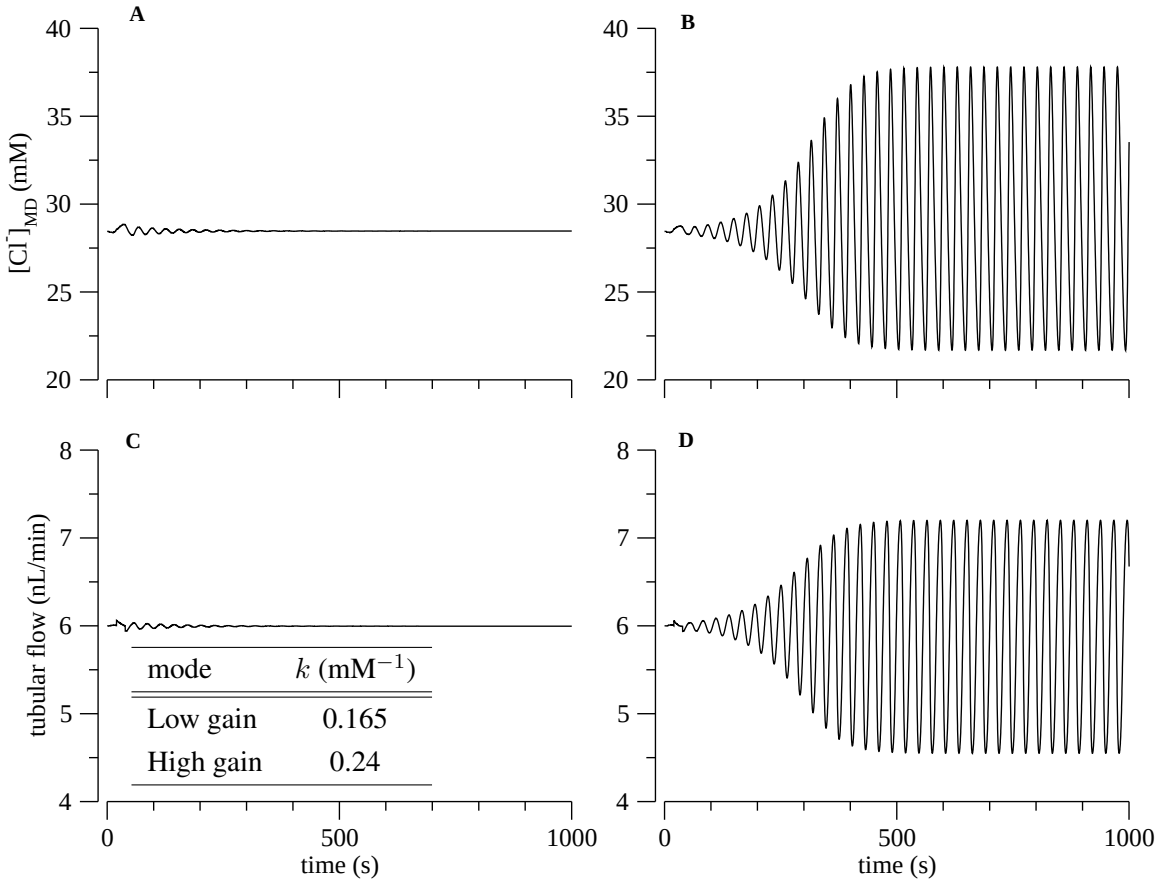

Figure 3.22: Inflow perturbation simulations. A step increase in flow rate of t_{tt} duration is introduced at time 60s. Panel A and B show the evolution of luminal [Cl^-] at macula densa ($x = 0.6$ cm). Panel C and D are tubular flow rate as given by the TGF function (equation 2.22). Panel A and C are the low-gain case in that after the perturbation the variables return to the steady-state (sink). Panel B and D are the high-gain case in that after the perturbation the sink (steady-state) transforms into a limit cycle (sustain periodic oscillations). The inset is a table that shows the TGF sensitivity values for the low-gain and high-gain cases.

At this point we can ask what happens to the efficiency of the TAL-TGF system when it is in either the low- or high-gain modes of operation. Figure 3.23 shows the efficiency along the tubule at different times after the above described step flow perturbation is made. We chose two time points for each mode: one time point corresponds when the Cl^- excursion peaked in its oscillatory excursion, and the other corresponds to the Cl^- excursion at its valley (see Figure 3.22 panel B). From panel A of the figure, we notice what was

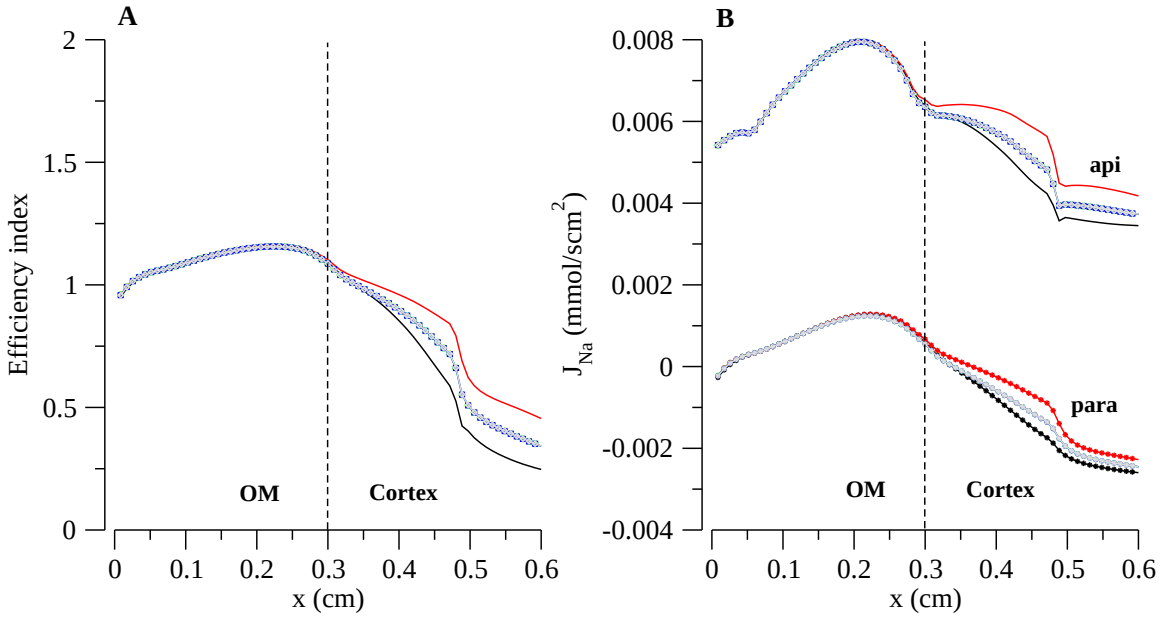

Figure 3.23: Efficiency index and fluxes along the TAL, after the pipette perturbation in Figure 3.22. In both panels: green (overlapped by gray and blue) regardless of the shape refer to the TAL with the TGF system loop open, while all other colors refer to when the the TGF loop is closed; black and blue is for when the Cl^- excursion in the outflow, which depends on the TGF system, is at a minimum; red and gray is for when the excursion in Cl^- concentration in the outflow is at maximum; low gain and high gain modes are denoted by the red and black pair, and the blue and gray pair respectively. In panel B the asterisked line is paracellular (para) flux and all others are for net apical (api) flux. Positive flux is reabsorptive flux.

foreshadowed in Figure 3.15: Since transport efficiency is influenced by flow rate, having a closed TGF loop affects the efficiency, in particular in the cortical region. In fact, Figure 3.23 panel A shows an increase in efficiency when the TAL-TGF system is in high gain

mode and the oscillatory flow rate is at its peak (red line). A lower efficiency is obtained also in high gain mode but when the flow is at a minimum. The cause for the increase in efficiency is seen on panel B. This panel shows greater transcellular reabsorption and slightly smaller backleak in the cortical regions. But the ultimate explanation for the efficiency increase comes from the transit time equation (3.2). A higher flow rate implies a shorter transit time, and as seen on Figure 3.12, a more even workload distribution. This simultaneously (seen in Figures 3.12 and 3.13) raises the concentration profiles along the TAL and yields a less diluted outflow. Hence, we must explore the impact on the luminal concentration profiles of the flow rate oscillations driven by the TGF system. Figure 3.24 shows the luminal profiles of the major solutes at different times once the oscillation are well established (no further increases in amplitude). The Na^+ profile, as expected, rises with the tubular flow rate, but is far from being undiluted (cf. figures 3.12 and 3.16). Nevertheless, these effects of TGF limit-cycle oscillations are very minor, in that the average efficiency over each cycle is essentially the same as the baseline steady-flow efficiency. This result is not surprising because the TGF parameters were set to yield TAL concentration profiles that were very similar to the open-loop profiles.

However, this dose not imply that TGF plays no role in regulating transport efficiency. At the segmental level, the TGF system acts synergistically with the CVR mechanism to increase transport efficiency by regulating tubular fluid inflow such that the outflow Na^+ and Cl^- concentrations are maintained well above the limiting static-head values where there is no net transport and zero efficiency. To see this, note that the low flow efficiency profile is lower than the baseline profile. The TGF system would respond to the low outflow Cl^-

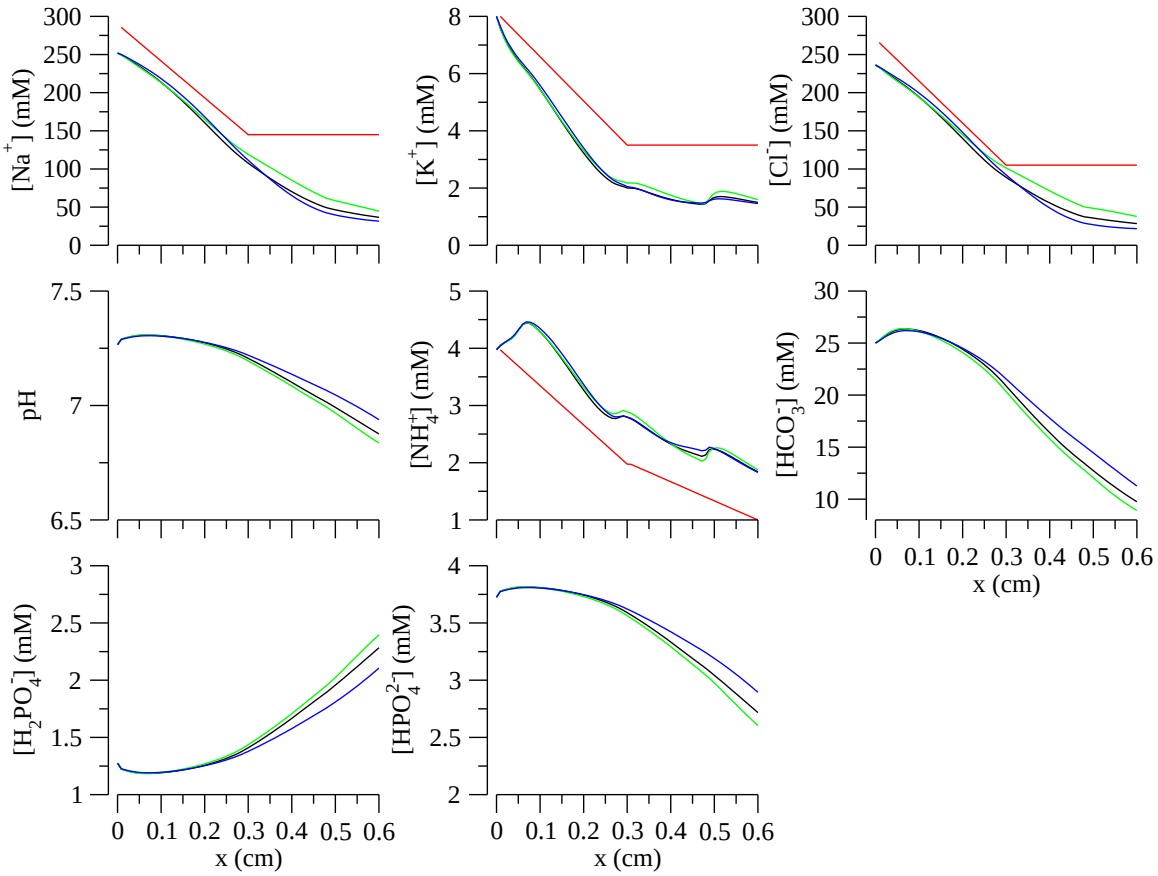

Figure 3.24: Steady-state luminal concentration for major solutes, computed by solving the TAL model (equations (2.1)-(2.4)) with flow given by the TGF system (equations (2.22)-(2.24)) with the limit cycle fully establish (TGF sensitivity 0.24 mM^{-1}). The black line is the steady-state value; the green line is at a time with Cl^- concentration in the outflow at its maximum; the blue line is for when the Cl^- in the outflow is at its minimum (see Figure 3.22); and the red line is the interstitial concentration profile.

concentration (see Figure 3.12) by raising inflow rate, which would then increase transport efficiency.

Together, the CVR responses and the regulation of TAL flow by TGF result in a quasi-uniform distribution of NaCl transport and an axial [Cl] gradient sufficiently steep to yield a TGF system gain consistent with experimental data. This suggests that TGF is a self-optimizing feedback system, in that it drives the TAL towards a state that ensures a high feedback gain. Further, TGF restrains tubular fluid inflow to levels that are consistent with

the reabsorptive capacity of the TAL, thereby ensuring that the effluent is adequately dilute for the operation of the urine concentrating mechanism.

3.4.2 TAL-TGF system: dynamic properties

Having established the role of cell volume regulation and the TGF system in workload distribution and efficiency of transport along the TAL, we shift gears and move on to elucidate some of the dynamic properties of the TAL-TGF system. The filtering properties, of the TAL and TGF system as a whole has been studied in [62, 42, 64]. But inasmuch as our TAL model, equations (2.1)-(2.4), (2.7), and the TGF equations (2.22)-(2.24), use a more detailed representation of the transmural fluxes and also track the cytosolic concentrations, we have the opportunity to zoom in to the cellular level to examine the dynamic properties of the cells when they are part of the tubule rather than in isolation.

External forcing at subcritical TGF system gain

Figure 3.25 shows what happens when the sinusoidal input forcing defined by equation (2.19) with amplitude (η) 50% of baseline flow (6 nL/min) and frequency (f) equal to $1/(2t_{tt})$ is applied to the system with and without the TGF loop closed. The first row shows the fluid input flow rate. In the open loop, or TGF disabled, case the first row shows the prescribed sinusoidal input flow. But when the loop is closed, or TGF system enabled, the distortion in waveform is evident. This distortion consists of an amplitude increase and in the destruction of the slope symmetry characteristic of the sine waves. The effect

of the TGF system delays for the first 5 s of simulation is also visible. The distortion in the input flow is not the same as the one observed in [42] since what they obtained was a slope symmetric wave, stretched on the time axis. This difference is explained by usage of different sensitivity values (k) for the TGF. For this simulation we chose a $k = 0.1650$ mM^{-1} that made the TGF system gain slightly less than the critical value where oscillations appear.

The second and third row show luminal [Cl^-] at the beginning (1% of the TAL) and at the MD (end of the TAL). In both cases, closing the loop essentially amplifies the changes in waveform produced by the TAL. Also, in contrast to the tubular inflow, the waveform for the concentration at the MD, for open and closed loop, is similar to the one obtained in [42]. This waveform distortion, as discussed in [62, 42], is caused by the nonlinear nature of the transport across the TAL tubule (see the flux equations in chapter 2). It is also noteworthy that the slope symmetry of the luminal Cl^- time record is lost as the fluid moves along the TAL. Thus the waveform distortion seen at the end of the tubule is a product of both the dependance of TAL NaCl transport on the transist time and the dynamics of the transporting elements (i.e. the cells) of the tubule.

The fourth and fifth row display the cytosolic Cl^- concentrations at the beginning and end of the TAL. It is noteworthy that regardless of whether the TGF system loop is open or closed, the transport processes in these cells, which are nonlinear, map the changes in Cl^- concentration in the lumen to changes in concentration in the cytosol almost just by a change in waveform amplitude and shift in concentration range. This type of transformation leaves the general shape of the waveform mostly unchanged. This might be an important

feature at the MD because the changes in luminal [Cl^-] are what initiate a cascade of biochemical events that ultimately lead to a change in tubular inflow by the TGF response.

The last two rows show normalized cell volume changes. As expected the smaller changes in cell volume correspond to cells located at beginning of the tubule where cell volume regulation is crucial to control apical solute uptake and, therefore, minimize swelling.

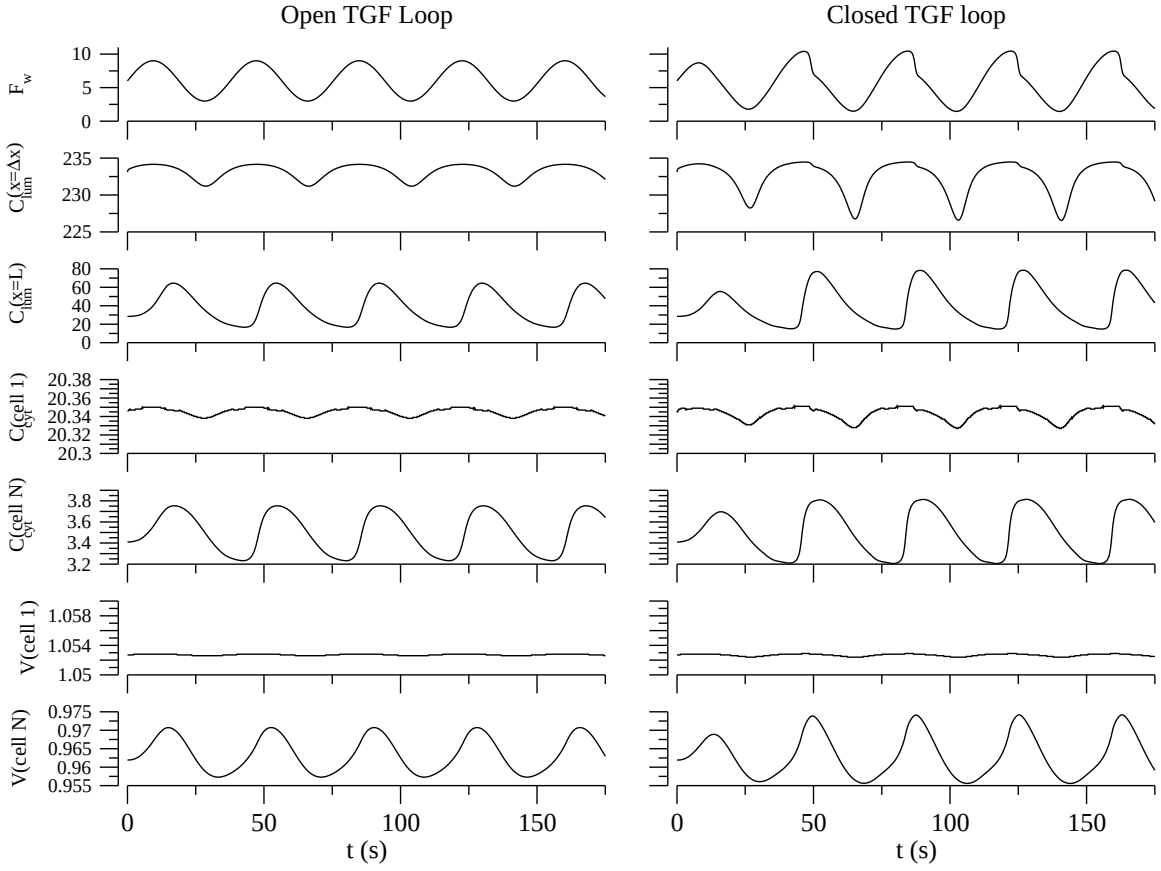

Figure 3.25: Time evolution for cytosolic and luminal Cl^- concentration (in mM) computed by solving the TAL model (equations (2.1)-(2.4)). Open TGF loop means a sinusoidal inflow forcing given by equation (2.19). Closed TGF loop means that the TGF inflow (equation (2.22)) and the sinusoidal forcing (2.19) were summed. The first row is the tubular inflow (nL/min); the second and third row are the luminal concentration (in mM) at the beginning and end of the tubule respectively; the fourth and fifth row are the cytosolic concentration (mM) at the beginning and end of the tubule respectively; and the sixth and seventh row are the normalized volume for the first and last cell of the tubule. The beginning of the tubule is defined to be at the deepest part of outer-medullary region.

Figure 3.26 shows the time course when a square wave forcing (see equation (2.20)) is applied to the system with and without the TGF loop closed. This type of forcing is potentially more feasible to realize in an experimental preparation, and simulate sequence of abrupt changes in tubular fluid inflow. On one hand, as with the sinusoidal forcing (Figure 3.26) when the loop is closed the tubular inflow waveform gets compressed; slope asymmetry appears for the luminal [Cl^-] at the MD; and the mapping of luminal to cytosolic concentration does not distort the waveform to a great extent (see below). On the other hand, the delaying effect of the TGF system is unequivocal, as demonstrated by the time shift seen when the luminal concentration drops at the beginning of the tubule ($x = \Delta x$) vis-à-vis the end of the tubule ($x = L$). It is important to point out that the moderate distortion introduced by the mapping of luminal to cytosolic concentrations seen in Figures 3.26 and 3.25 might not hold if the cell volume regulation is significantly delayed with a non linear delay mechanism.

Broad-band forcing at subcritical TGF gain

A broad-band forcing, in contrast to a pure sinusoidal forcing or even a square wave forcing, has many oscillatory components over a specified band of the frequency spectrum. This property makes this type of forcing a means to uncover the filtering properties of the TAL. Figure 3.27 shows the power spectral density functions (PSDs) when a broad-band forcing, as defined by equation (2.21), is applied to the system without the TGF loop closed and summed to a constant baseline flow of 6 nL/min (see equation 2.18). The frequencies of the forcing were prescribed up to the Nyquist frequency ($1/(2\Delta t) = 4642$ mHz) to avoid

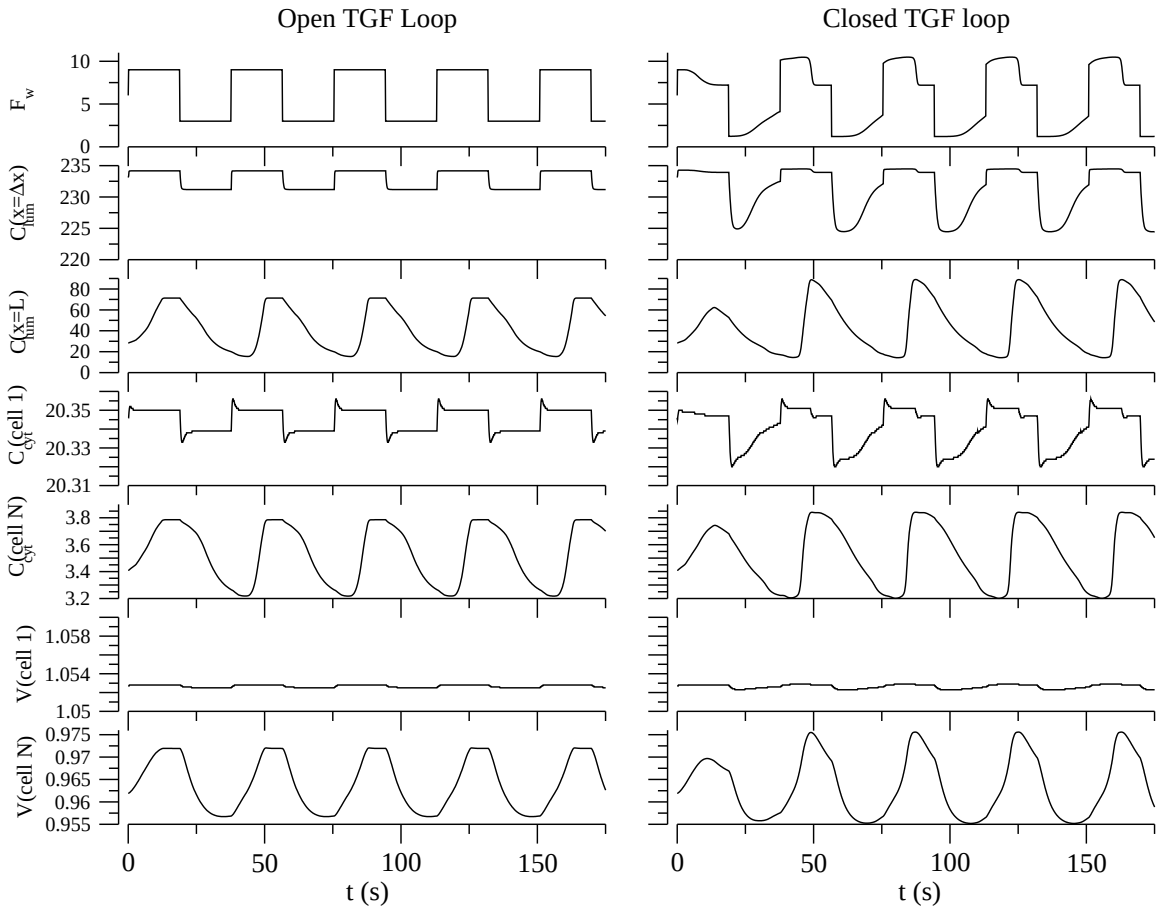

Figure 3.26: Time evolution for cytosolic and luminal Cl^- concentration (in mM) computed by solving the TAL model (equations (2.1)-(2.4)). Open TGF loop means a square wave inflow forcing given by equation (2.20). Closed TGF loop means that the TGF inflow (equation (2.22)) and the square wave forcing (2.20) were summed. The first row is the tubular inflow (nL/min); the second and third row are the luminal concentration (mM) at the beginning and end of the tubule respectively; the fourth and fifth row are the cytosolic concentration (mM) at the beginning and end of the tubule respectively; and the sixth and seventh row are the normalized volume for the first and last cell of the tubule. The beginning of the tubule is defined to be at the deepest part of the outer-medullary region.

aliasing. The power spectrum of the forcing is shown in the upper graph of the figure. The second plot shows the power spectrum of luminal [Cl^-] at the macula densa (MD), and the third plot shows the ratio of the PSDs functions on the second and first plots. We call this the output-to-input ratio where the output in this case is [Cl^-] at the MD and the input is the broad-band forcing plus the baseline flow. This normalization was chosen because it describes the dynamics of the TAL process that transduces fluctuations in the inflow into changes in MD Cl^- concentration which is the sensed variable of the TGF system.

As noted previously in [62, 42], we observe in the second and third plot of Figure 3.27 that the TAL behaves like a low-pass filter, since the higher the frequency the smaller the amplitude in the periodogram. Additionally, the spectrum for chloride reveals that there is some harmonic structure. The location, in terms of frequency, of the local minima or nodes in the PSD correspond to frequency at which the local minima for magnitude in macula densa excursions were observed in Figure 3.19. The same applies for the local maxima or antinodes in the PSD and the local maxima observed in Figure 3.19. The locations of the local minima or nodes in the PSD are given in the table inset on Figure 3.27; also shown are the results obtained by the authors of [62]. In general, this behavior and the actual node location is close to what was found in [62] even though there are subtle differences.

The power spectra when a broad-band forcing is applied but the TGF loop is closed can be seen in Figure 3.28. It is notable that the PSD of the inflow (first plot) now exhibits a peak at frequency of 35 mHz, but as observed in the PSD of [Cl^-] at the MD and in the input-output relationship, the harmonic structure as well as the filtering behavior of the TAL remains unchanged. Moreover, the output-to-input ratio (PSD on last plot), shows

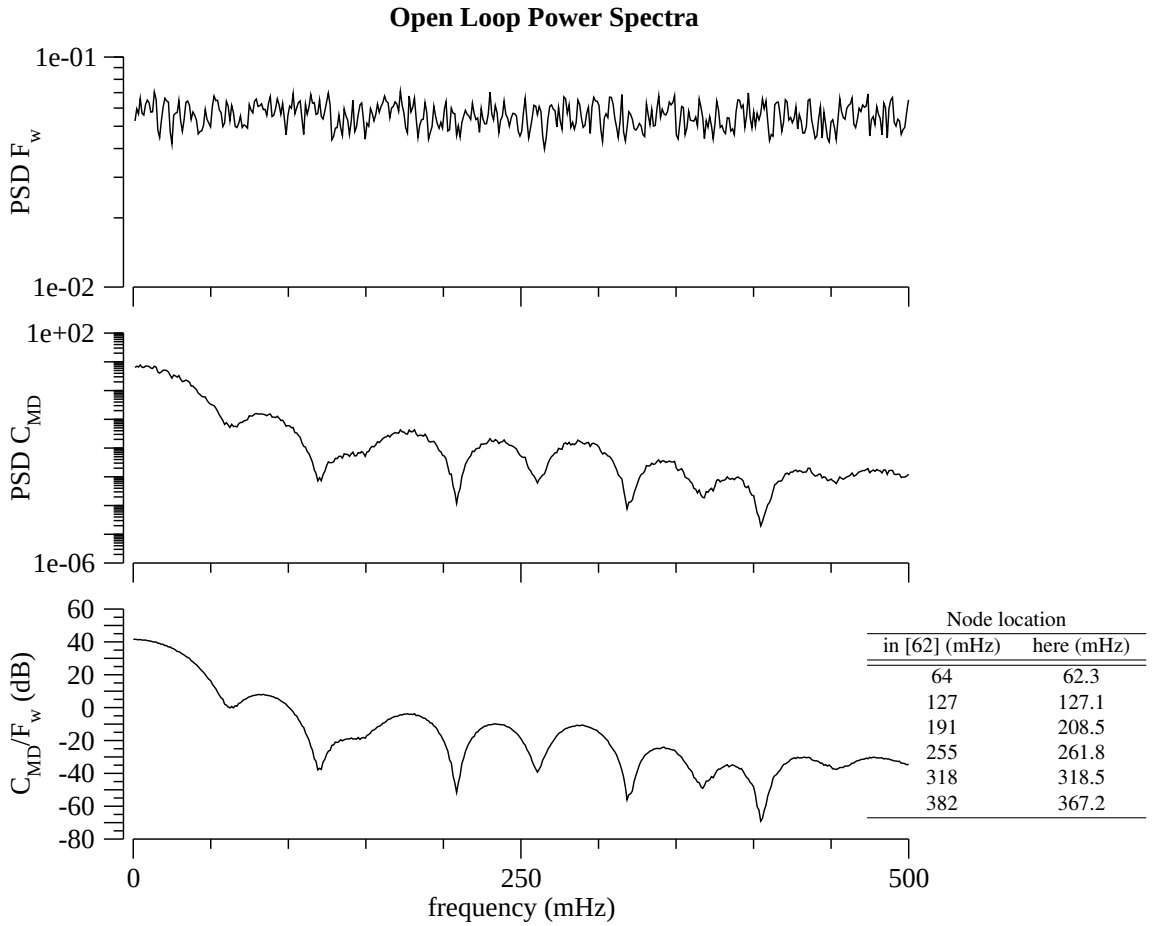

Figure 3.27: Power spectrum density (PSD) estimation computed via the methods described in [65, 66]. The frequency range shown is below the Nyquist frequency (4642 mHz). The first plot shows the power spectrum of the broad-band forcing in tubular water inflow (the nonuniform power spectrum comes from not choosing the frequencies of the forcing to be equal to the frequencies of the DFT used to compute the PSD). The second plot displays the PSD for the $[Cl^-]$ at the macula densa, and the third plot shows the ratio of output (PSD on second row) to input (PSD of first row). The table inset gives the location of the nodes.

that the peak at 35 mHz is a product of the TGF input flow. This 34 mHz oscillation was already noted in the pipette perturbation simulations when the high gain case was examined (see Figure 3.22), and is going to be present in all simulations involving the closing the TGF loop, because it is the resonant frequency of the TGF system. We can also point out that, in the open and closed loop cases (Figures 3.27 and 3.28), the input-to-output relation for frequencies below 100 mHz is somewhat amplified (ratio of output to input is positive on that interval of frequencies). This explains why the excursions in macula densa concentrations are higher for the low frequency oscillatory forcings that we saw in Figures 3.17 and 3.19 without TGF.

Global dynamics of the TAL cells

Having seen the importance of the transcellular pathway, or apical fluxes, for tubular fluid dilution in the previous sections, and since our model provides a detailed representation of that pathway, we now examine the dynamics of the apical fluxes when a broad-band forcing is applied. Figure 3.29 shows the ratio of apical fluxes PSD to broad-band forcing PSD with the TGF loop closed, for different locations along the TAL (columns) and for different solutes (rows). The figure can be interpreted as an output to input ratio where the input is the broad-band forcing plus the fluid flow prescribed by the TGF system and the output is the apical flux. From the figure we can infer the following: first, the frequency associated with the TGF system ($\sim$35 mHz) is where the global maximum of all spectra is located. This is not surprising since the tubular inflow should have a significant influence on all of the apical fluxes along the TAL. Second, the harmonic structure is not uniform

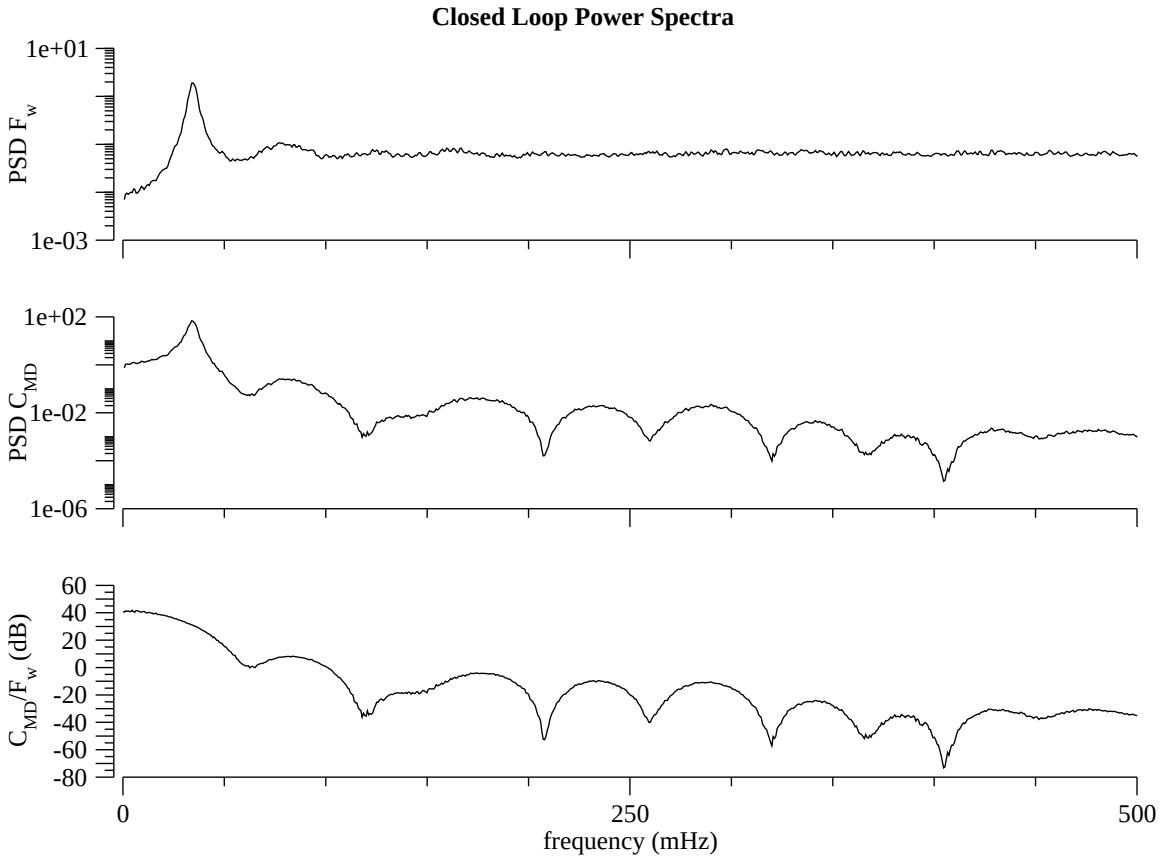

Figure 3.28: Power spectrum density (PSD) estimation computed via the methods described in [65, 66]. The frequency range shown is below the Nyquist frequency (5338.3 mHz). First row shows the power spectrum of the broad-band forcing in tubular water inflow with TGF loop closed. The second row display the PSD for the $[Cl^-]$ at the macula densa, and the third row shows the ratio of output (PSD on second row) to input (PSD of first row).

either along the length of the TAL or for each solute. As one moves from the OM to the late cortex, the oscillations of the apical fluxes are amplified with the exception of those for NH_4^+. The cause for the exception is that NH_4^+ and K^+ compete for uptake through NKCC and exclude one another from the transporter. This underlines the importance of NH_4^+ in the outer medullary region as a substitute for K^+ in order to avoid its depletion in the lumen. Additionally, the amplification of the oscillations as one moves from medullary to cortical regions of the TAL indicates that transcellular reabsorption becomes more important in the cortical regions where the paracellular transport is hampered by the transepithelial concen-

tration gradient, but transcellular transport capacity is not greatly impaired. Third, the noise from the broad-band forcing diminishes as one moves toward the cortex, again, with the exception of NH_4^+. In part, this is expected owing to the fact that the broad-band forcing was applied to the input water flow, but what is unexpected is that the NH_4^+ PSD exhibits nodal structure from the very beginning of the tubule. We attribute this phenomenon to the increased ammonium uptake in the OM. And fourth, the location of the optima in the spectra (with exception of the global maximum which is tied to the TGF frequency) correspond to the frequencies at which the maximum and minimum range in magnitude of excursions of solute concentration are located. This is noted by comparing the location of the peaks and valleys for Cl^- apical flux at the late cortex in Figure 3.29 with the optima location for the magnitude of range of excursion given in Figure 3.19. All of this underlines the dependency of the harmonic structure observed in the PSD on the steady-state transit time (t_{tt}). Also, as already noted in [62], change in location along the TAL implies changes in the harmonic structure, since the transit time is a function of tubule length (see equation 3.2). However, what is not self-evident is that the transit time is not going to be exactly the same for all solutes. That explains the variations in harmonic structure (optima location) that are seen in Figure 3.29 for each solute.

Besides transcellular transport, paracellular transport is the other pathway for dilution of the tubular fluid in the TAL. Figure 3.30 shows the PSDs of the output-to-input ratio where the output is the paracellular flux, and the input is the broad-band forcing plus the TGF system water inflow. The rows of the figure show different solutes, and the columns show different locations along the length of the TAL. It is important to recall that, while

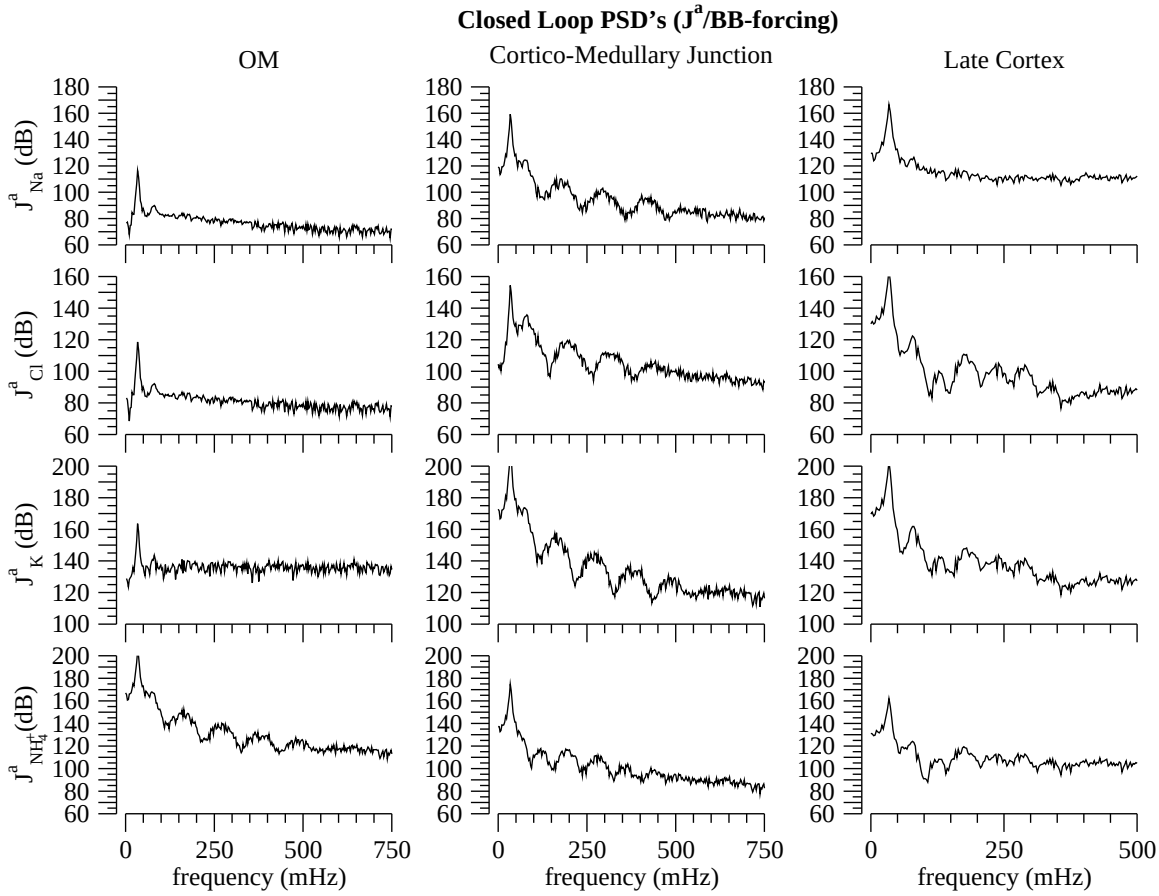

Figure 3.29: Power spectrum density (PSD) estimation computed via the methods described in [65, 66]. The frequency range shown is below the Nyquist frequency (5.338 Hz). Along the rows we have the PSD of the output-input ratio between apical flux (output) and broad-band forcing (input) for the major solutes. The columns refer to three different locations along the TAL.

the apical fluxes are a linear combination of electrodiffusive and carrier mediated fluxes, the paracellular fluxes are purely electrodiffusive. As with the apical fluxes, we observe that the amplitude of the oscillations is not uniform along the TAL. Even so, for Na^+, rather than an increase in amplitude like that seen with the apical fluxes (see Figure 3.29), we have a decrease. This results from the reduction of paracellular Na^+ transport in the cortical region, which we observed in previous sections, and which is one of the causes for the decrease of efficiency of Na^+ transport in this region. The node locations are close to the node locations for the apical fluxes, and the global maximum is caused by resonance

the TGF loop.

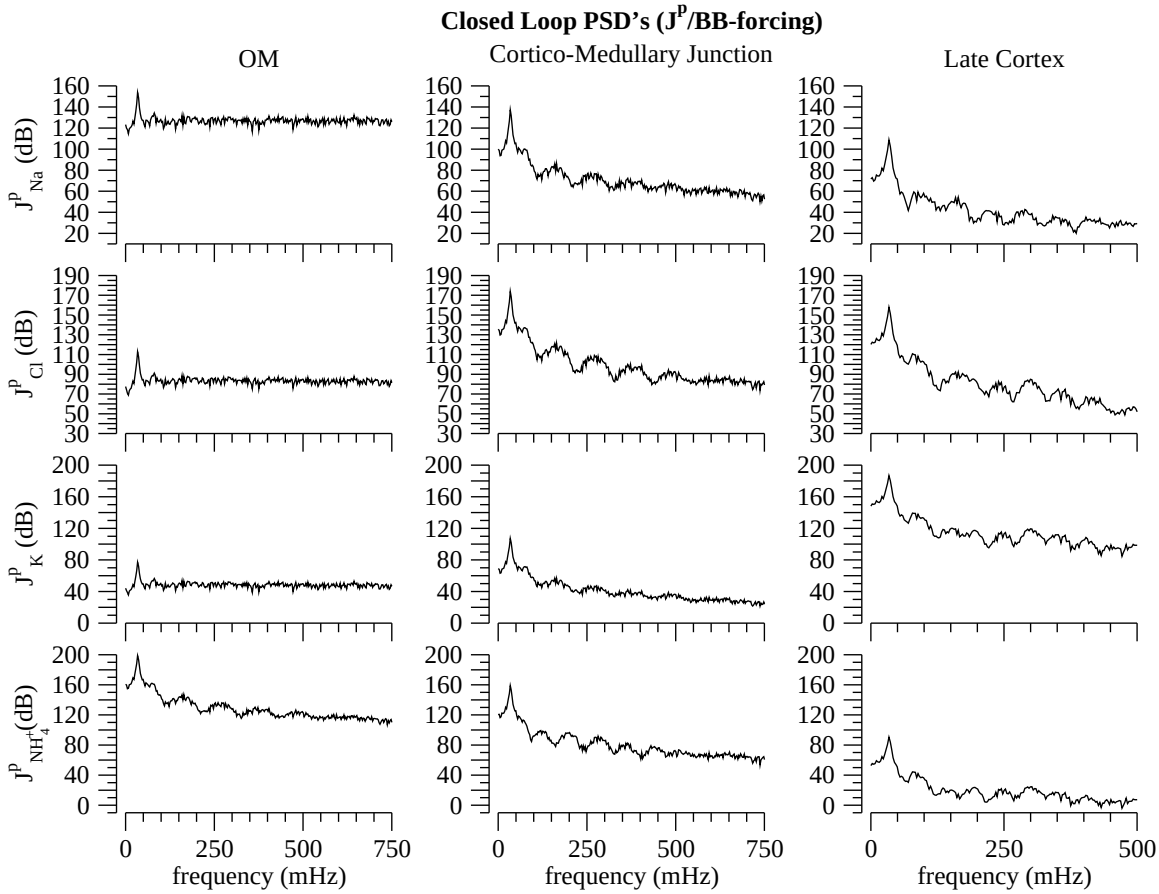

Figure 3.30: Power spectrum density (PSD) estimation computed via the methods as described in [65, 66]. The frequency range shown is below the Nyquist frequency (5.338 Hz). Along the rows we have the PSD of the output-input ratio between paracellular flux (output) and broad-band forcing (input) for the major solutes. The columns refer to three different locations along the TAL.

In general, Figures 3.29 and 3.30 reveal that the harmonic structure of the TAL, i.e. the location in terms of frequency of the nodes and antinodes in the power spectrum, is a local phenomenon. This means, that any cell reponse will depend on the luminal solute concentration at the location of the particular cell. This is explained by the observation, in [62] and in Figure 3.19, that the locations of the optima in the power spectra correspond to the frequencies where the oscillatory components have a transit time close to the steady-state transit time. Such dependency on transit time yields the variation by location along the

tubule, since by definition the transit time is a function of tubule length. Also we note that the harmonic structure will not be identical for all solutes, owing to the different transport pathways that the solutes go through. Finally, Figures 3.29 and 3.30 point out that for Na^+, the transcellular pathway gains importance as one moves from medullary to cortical regions of the TAL, while the opposite happens for the paracellular pathway. **?? Add text:** This follows the pattern of paracellular permeabilities.

Local dynamics of TAL cells

We have already established the dependence of the dynamic structure on location along the tubule, and we have seen in Figures 3.25 and 3.26 that the mapping from luminal Cl^- concentration waveform to cytosolic concentration does not greatly distort the waveform. Here, we proceed to studying the input/output relationships for cells when they are part of the segment model. Clearly, TAL cells are multi-input multi-output systems, and since the main task of these cells is to dilute the tubular fluid, we can assume that the luminal concentrations are the inputs while the cytosolic concentrations are the outputs. Moreover, as we have seen throughout the present work, the inputs are not independent of one another, making the cells a complicated system to analyze. Now, to keep things simple, let us treat the cell as a system of parallel single inputs/outputs rather than a fully multi-input/multi-output system. This means that the cell is assumed to be a collection of single input/output systems.

Figure 3.31 shows the ratio of power spectrum density functions of cytosolic (output) to luminal (input) concentrations for major solutes (one per row) at different locations along

the TAL (one per column). The broad-band forcing described above was added to the fluid inflow given by the TGF system (closed loop). Each panel in the figure can be interpreted as a plot of the gain factor of the system (cell) as a function of frequency. In general we observe that for all solutes, with the exception of NH_4^+ and partly Na^+, the gain tends to increase from the outer medullary toward cortical direction. In spite of that, the gain values are less than zero for Na^+, Cl^- at the three reported locations along the TAL. This means that we have input-to-output (I/O) attenuation rather than amplification. This explains the relatively low changes in cytosolic concentrations observed in the sinusoidal and square wave forcing simulations (see Figures 3.17 and 3.20a). For K^+ in the cortical region the gain is positive, meaning that the I/O relation is amplified.

Now, in the cortico-medullary junction we observe some interesting behavior. For the Na^+ and Cl^- pair, it is clear that they have a similar nodal structure. For K^+ and NH_4^+ their nodal structure is not as close to one another as in the previous case. This grouping is due to the transport pathways that take the solutes across the apical membrane. At the late cortex, we can group the nodal structure of the solutes in a similar fashion as we did for the cortico-medullary junction. It is noteworthy that the peaks and valleys for Na^+ and Cl^- are not as neatly defined as in the cortico-medullary region, but the locations of the peaks and valleys follow from the same principles explained for Figures 3.28, 3.29, and 3.30, and similarly the harmonic structure at the other locations along the tubule. Also, for K^+ and NH_4^+ at the late cortex, the amplitude of their respective gains seems to mirror one another. This behavior arises from their competition for entry through NKCC2.

The interpretation of the plots in Figure 3.31 as gains implicitly assumes an ideal linear

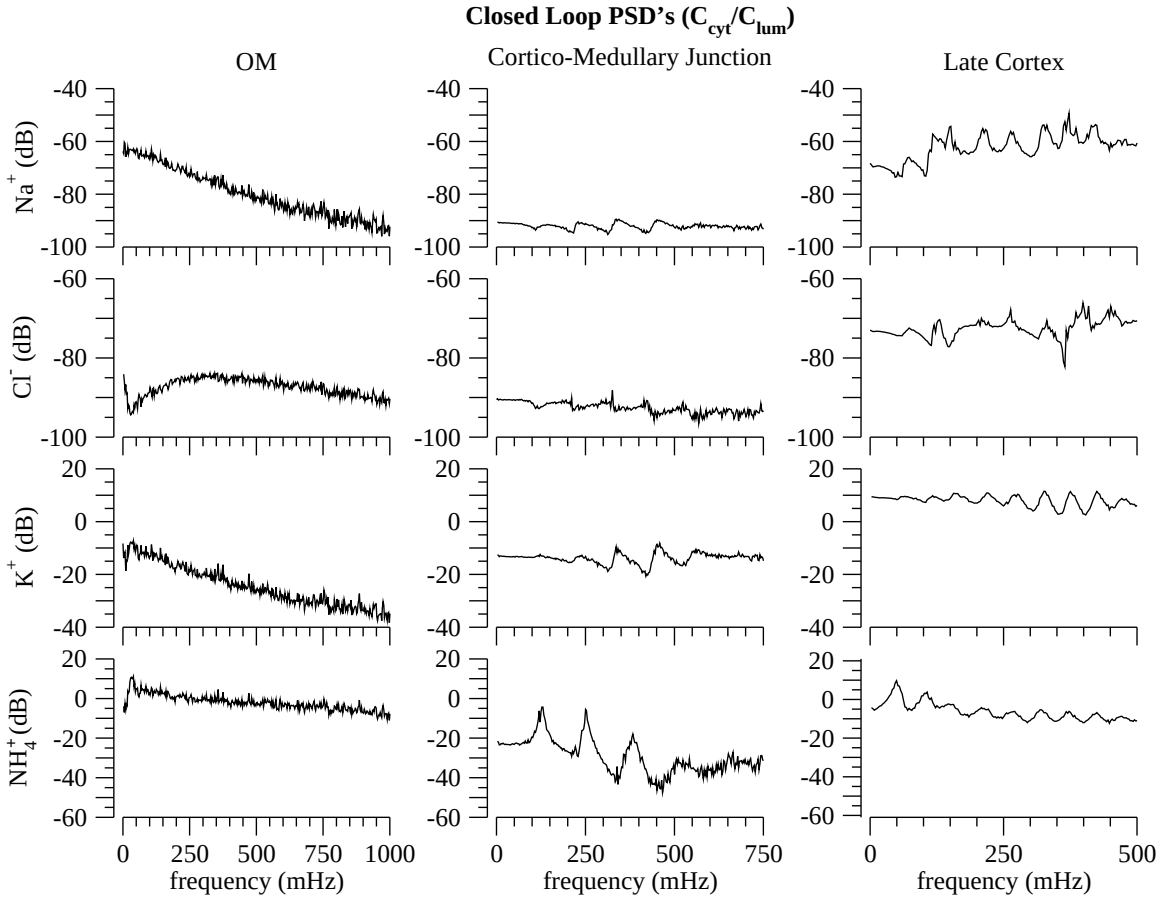

Figure 3.31: Power spectral density (PSD) estimation computed via method described in [65, 66]. The frequency range shown is below the Nyquist frequency (5.338 Hz). Along the rows we have the PSD of the output-input ratio between cytosolic (output) and luminal (input) concentrations for the major solutes. The columns refer to three different locations along the TAL.

relation between input and outputs. That is, the output is the convolution integral of the input and a weighting function called the input response function. From the model equations, in particular from the flux equations (see equations (2.1)-(2.4), (2.5) and the kinetic models for carrier-mediated transport) we know that that might not be the case. But besides this, the lack of waveform distortion seen in Figures 3.25 and 3.26 between luminal and cytosolic concentrations tells us otherwise. Nevertheless, by looking at the coherence function between the inputs and outputs we can determine by how far off base we are by considering the cell as idealized linear system. A coherence value of unity means that, at the given

frequency, the system behaves as the ideal linear system (output is convolution of input and unit impulse response). A coherence of zero means that output and input are unrelated, and a value between zero and one means that either noise is present, the input/output (I/O) relation is not linear or the output is influenced by the considered input as well as other inputs. A detailed description of the coherence function is given in [65].

Figure 3.32 shows the coherence function from the same set of inputs and outputs that we took for Figure 3.31 (Figure 3.32b is just a zoom in of Figure 3.32a). Given the nonlinearity and the interdependency of the transport process that link the cytosolic and luminal concentrations, we were flabbergasted to find that the coherence is closer, in the ∞-norm sense, to one than to zero. As seen in Figure 3.32a, for all solutes the coherence gets very close to zero only for a specific set of frequencies. Now, if we zoom into the 1 Hz range (Figure 3.32b), the space dependency as well as the solute dependency becomes clear. In the OM the coherence is diminished at frequencies that are multiples of 0.25 Hz, and this is more noticeable for K^+ than for the other solutes. This is caused by the fact that cytosolic K^+ is linked to luminal K^+ as well as to luminal and cytosolic NH_4^+, through the competition for a binding site on NKCC2. In the other parts of the tubule similar behavior is observed, but the weakening of the coherence is more apparent at very low frequencies (below 0.1 Hz). It is important not to forget that the TGF system is a nonlinear component with a low frequency component (35 mHz), and that will contribute to the loss of coherence seen at low frequencies in the distal parts of the TAL. Furthermore, the drops in coherence from one to values in the interval $(0, 1)$ at specific frequencies are certainly not caused by the underlying noise of the broad-band forcing, because the forcing contains a uniformly

distributed set of frequency components. Broadly, Figure 3.32 tell us that the assumptions made for the interpretation of Figure 3.31 are not unreasonable, and explains the lack of dramatic waveform distortion in the luminal-to-cytosolic concentration mapping depicted in Figure 3.25 and 3.26.

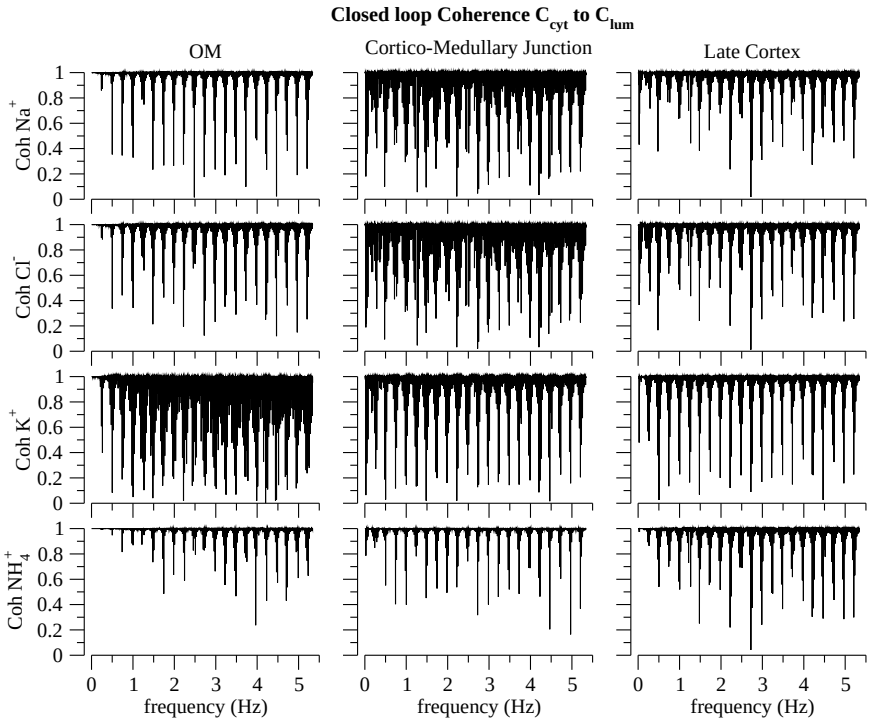

(a) Full range of frequencies.

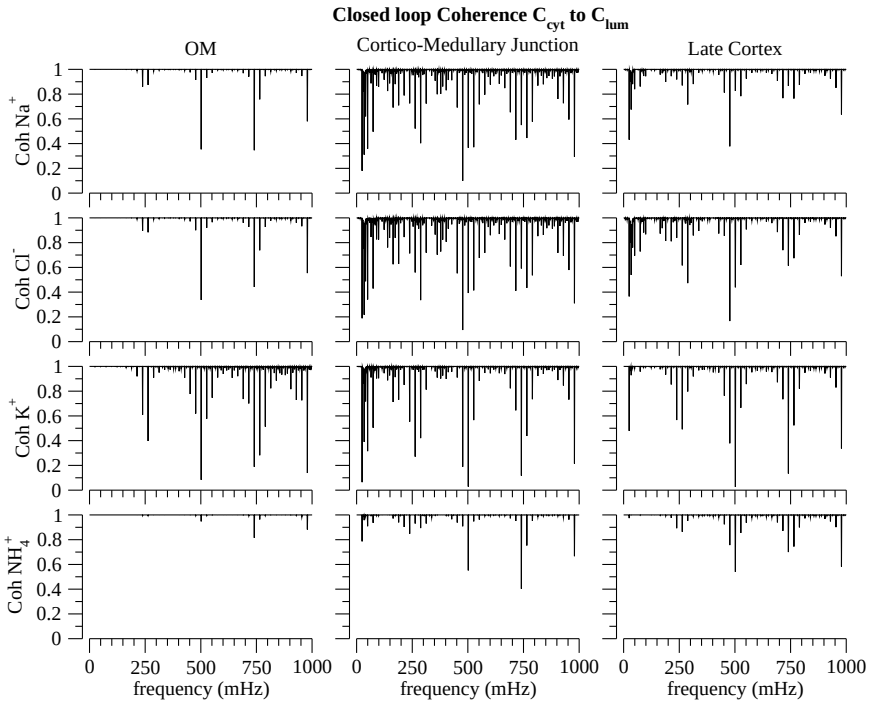

(b) Zoom in to frequencies below 1 Hz

Figure 3.32: Coherence function as defined in [65] for the input output relationship defined by luminal (input) to cytosolic (output) concentration at different locations along the TAL. The frequency range shown is below the Nyquist frequency (4642 mHz). Figure 3.32b is just a zoom-in of Figure 3.32b.

Chapter 4

Summary and discussion

The main function of the thick ascending limb (TAL) segment and of the cells that comprise it is to dilute the tubular fluid in order to build the interstitial osmolarity gradient that is necessary for passive water reabsorption in the collecting duct segment of the nephron. We used a cell-based multiscale model of the TAL to study the transport properties of this segment. The major results of this modeling study are:

- Because the function of the TAL segment is to generate dilute tubular fluid, the transepithelial [Na^+] gradient that is created substantially reduces transport efficiency. This factor calls into question the widely-held notion that a substantial fraction of TAL Na^+ reabsorption occurs by passive paracellular diffusion secondary to apical membrane K^+ cycling.

- CVR responses in individual autonomous TAL cells limits Na^+ transport by each cell such that the workload distribution along the TAL segment is sufficiently uniform to

result in more efficient transport. In essence, a self-organization process that raises transport efficiency emerges from the CVR responses in the ensemble of TAL cells.

- At the segmental level, the TGF system acts synergistically with the CVR mechanism to increase transport efficiency by regulating tubular fluid inflow such that the outflow Na^+ and Cl^- concentrations are maintained well above the limiting static-head values where there is no net transport and zero efficiency. Further, TGF restrains tubular fluid inflow to levels that are consistent with the reabsorptive capacity of the TAL, thereby ensuring that the effluent is adequately dilute for the operation of the urine concentrating mechanism.

- Together, the CVR responses and the regulation of TAL flow by TGF result in a quasi-uniform distribution of NaCl transport and an axial [Cl] gradient sufficiently steep to yield a TGF system gain consistent with experimental data. This suggests that TGF is a self-optimizing feedback system, in that it drives the TAL towards a state that ensures a high feedback gain.

- The apical membrane cycling of NH_4^+ through K^+ channels, the NKCC2 transporter, and the NHE exchanger prevents luminal potassium depletion and substantially increases Na^+ uptake into the TAL cells. Without NH_4^+ cycling, the TAL model predicts that the dilutional capacity of the TAL will be severely compromised.

- When TAL inflow oscillates, the TAL segment acts as a nonlinear low-pass filter with a characteristic harmonic structure that reflects the establishment of standing waves of Na^+ and Cl^- in the lumen of the TAL. This finding is consistent with both earlier

modeling efforts and experimental data. In addition, the TAL cells themselves are predicted to act as multi-input/multi-output nonlinear filters.

- When the TGF system is active and its gain exceeds a critical value, limit cycle oscillations in tubular fluid flow emerge, a behavior that is consistent with experimental observations.

Cell volume regulation responses have been observed by Komlosi [56] and are clearly reproduced by our cell model (equation (2.3)-(2.4)), see Figure 3.8. But to address the question of how important are CVR responses in controlling Na^+ transport across the TAL epithelium, we used the TAL cell model to simulate short-circuit current experiments [55]. The results not only stress the importance of NKCC2 as the main NaCl pathway, but also underline that a side-effect of CVR is the regulation of Na^+ reabsorption across the epithelium (see Figure 3.2, panel B). Moreover, the impact of CVR cannot be uniform along the TAL (see Figure 3.2, panel A) if short-circuit current values along the TAL are to be close to experimental observations. Simultaneously the results showed, as expected, that CVR responses minimized changes in cytosolic concentrations along the TAL when compared with non CVR case.

The significant presence of ammonium in the kidney and its role in Na^+ transport in the TAL led us to simulate NH_4^+ pulse experiments in [21]. In these simulations, the cell model was able to reproduce the experimentally observed drop in cytosolic pH when a luminal NH_4^+ perturbation is introduced. We observed the phenomenon of NH_4^+ cycling, that is, NH_4^+ uptake through NKCC2 and apical channels, causing the cytosolic pH to drop, and

apical extrusion via NH3. As also noted in [67], this phenomenon is important for more than one reason. Besides being a pH control system, the participation of NHE3 in the NH_4^+ cycling phenomenon stresses the importance of NHE3 as a Na^+ entry pathway. This implies that the exchanger (NHE3) is another non-neglectible component of the transcellular diluting machinery of the TAL.

Both the short-circuit current and the NH_4^+ perturbation simulation illustrate the difficulty of fitting the cell model, via solving a least-squares problem, to different sets of experimental data. Moreover, embedding the fitted-to-data cell model into the segment model (equations (2.1)-(2.4)) and expecting that it will work just fine is not true. The variability of the environment along the TAL makes it essentially impossible to find a parameter set for the cell model that will fit all possible locations . Therefore, much more in vivo electrophysiological data for cells along the TAL is needed to formally assess the values of all parameters of the cell model. Then, perhaps, one could construct cell models that will work at the segmental level without any further parameter adjustments.

TAL cells, specifically those in the outer medulla (OM), live in an environment with limited O_2 availability owing to low blood flow [16]. Hence, transport efficiency and workload distribution along the TAL are important issues. Furthermore, high efficiency in Na^+ transport by the TAL has been a standard assumption. The standard textbook model [18] consists of the TAL segment reabsorbing Na^+ efficiently because of increased paracellular electrodiffusive transport. Such transport is thought to be driven by the positive transepithelial potential established by K^+ cycling, that is, K^+ entering the cell via NKCC2 and leaking out through K^+ channels. But in reality, that scheme can be substantially more com-

plicated, since cell volume regulation (CVR) mechanisms adjust the transport rate through NKCC. Further, NH_4^+ has to be taken into account, and the transepithelial chemical gradient established by the dilution of the tubular fluid can be detrimental to the efficiency.

The complexity of the solute transport processes along the TAL and the shortcomings of the K^+ cycling scheme to raise efficiency were observed using the cell model. We showed in Figure 3.9 that the efficiency drops conspicuously as the luminal concentration decreases, and that not even a very positive transepithelial potential can stop the backleak in the distal TAL where the tubular fluid is very dilute with respect to the interstitium. Using the segment model (equations (2.1)-(2.4)), we reach the same conclusion. As seen in Figures 3.15, 3.16, and 3.23, the TAL segment is not as efficient as expected in terms of minimizing paracellular backleak and reabsorbing one Na^+ paracellularly per Na^+ reabsorbed transcellularly. In spite of that, it is important to notice the following: First, when cells regulate their volume or when the TGF system is enabled, the efficiency, albeit low (i.e. far from two), is still higher than when compared with non-CVR or non-TGF cases, in particular in the cortical region (see Figures 3.15 and 3.16). Second, CVR and the TGF system work synergistically toward increasing the efficiency. This opens the possibility of transport efficiency being high when all control systems in the TAL are taken into account. Although this would still undermine the idea of K^+ cycling as the only mechanism responsible for a highly efficient TAL. Third, "perfect" cycling of K^+ could raise the the transport efficiency substantially. By "perfect" we mean that all K^+ uptake by NKCC gets extruded by apical K^+ channels. If that is the case, a stronger transepithelial electrical potential would develop, and such potential could drive paracellular reabsorption. To achieve

that "perfect" cycling a spatial association between NKCC and the apical K^+ channel has to exist. In the model, this idea can be tested by creating a cytosolic subcompartment that delays well-mixing of K^+ in the cytosol. Experimentally, a protocol to measure the spatial distribution of NKCC and apical K^+ channels in the apical membrane would have to be used. And fourth, as shown in Figure 3.16, when NH_4^+ cycling is undermined, higher transport efficiency is obtained but at the expense of poor dilution of tubular fluid. This means that there might be an trade-off between a highly efficient TAL transport and proper tubular dilution.

It is also important to discriminate between the transport efficiency index and workload distribution, because one does not imply the other. A quasilinear workload distribution in terms of transport will generate a quasilinear concentration profile along the length of the TAL for Na^+ and Cl^+ in that all cells participate in the transmural transport and not only those in the OM where O_2 is more scarce and a more concentrated inflow is seen. And, whereas the increase in efficiency index because of CVR does not seem dramatic, its impact on workload distribution is significant. As seen in Figure 3.12, regardless of the flow rate, without the CVR mechanism more reabsorption is done by cells in the OM, and the workload is poorly distributed along the TAL. The issue of workload distribution along the TAL also turns out to be crucial for proper functioning of the tubuloglomerular feedback (TGF) system. A close-to-zero slope in $[Cl^-]$ at the end of the TAL will decrease the TGF gain and hamper its response. Therefore, as seen in Figure 3.12, CVR is important to generate a nonzero Cl^- slope necessary for the TGF to have a nonzero gain. Higher inflow rates also affect the workload distribution (see Figure 3.12) because a higher flow

rate implies a shorter transit time giving cells downstream a relatively undiluted luminal fluid to work on. That is why higher flow rates raise the concentration profile along the TAL. The trade-off is that the tubular fluid ends up being poorly diluted.

Driven by the definitive impact of the TGF system in tubular fluid dilution in the TAL, we used our multiscale TAL model to examine some of the well-known dynamical properties of the TAL, with and without the TGF loop closed. With the TGF loop open (i.e., flow not independent of the TGF system) we observed larger excursions in macula densa (MD) concentrations for low frequency sinusoidal and square-wave forcing of the tubular water inflow. As forcing frequency is increased, the excursions are smaller, and the appearance of minima (nodes) and maxima (antinodes) in the magnitude of the excursions at different locations along the TAL is unmistakable. This reflects the establishment of standing waves in the luminal concentration profiles. Now, regardless of the forcing frequency, the monotonic decreasing property of the luminal concentration profile is not lost, and the changes in cytosolic concentration for any cell along the tubule are small when compared with the luminal concentration changes. This underlines the homeostatic control of cellular composition in spite of the forcing applied by the environment.

The oscillatory forcing to the tubular inflow also reveals that, as the waveform travels along the TAL, it is nonlinearly distorted. This illustrates the nonlinear nature of the TAL as a whole. In contrast, the lack of distortion from luminal to cytosolic Cl^- concentration changes at different locations along the tubule is remarkable. This suggests that the nonlinear transformations in tubular composition accumulates along the TAL. With the sinusoidal forcing and the TGF loop closed, similar behavior is seen, although the delay

effects of the TGF system and its nonlinear nature is apparent. The nonlinear filtering property of the TAL was firmly established by applying broad-band forcing and observing that the amplitude of the computed power spectral density function for luminal Cl^- decays with increasing frequency, regardless of having the TGF loop closed or open. We also noted that the harmonic structure, or frequencies, at which the local minima and maxima in the power spectra are located, correspond to the frequencies of the oscillatory flow that have a transit time close to the steady-state transit time. When the TGF loop is closed, most of the observed dynamical properties remain valid although, the nonlinearity of the TGF system and its resonance peak at low frequencies becomes apparent. The harmonic structure, though similar to what has been observed by other investigators [42], especially for low frequencies (below 500 mHz), it is not uniform with solute nor location along the tubule. Such spatial dependency is tied to the steady-state transit time, and the solute dependency to the particulars of the transmural transport pathway for the solute under consideration.

The spatial dependency of the harmonic structure, as well as the lack of a dramatic waveform distortion when luminal concentrations are mapped (through transport processes) to cytosolic concentrations, motivated us to examine input/output (I/O) relationships for cells along the tubule. There the inputs are luminal concentrations, and outputs are cytosolic concentrations. This revealed that if cells are considered as ideal linear I/O systems, their gain increases as one moves from outer medulla (OM) to cortical TAL, and that for ammonium and potassium, the gain is larger than for the other solutes. We also showed that the linearity assumption holds better than expected, since the drops in coherence function occur at a discrete set of frequencies, some of them the very low frequencies for which the

TGF system exhibits a high gain while others are the ones that yield an oscillatory flow with transit time close to the steady-state transit time.

We also examined the dynamic behavior of the TAL at the segmental level and at the cellular level. We applied sinusoidal, square-wave, and broad-band forcing to the tubular inflow and examine the dynamics in the tubule and in the cytosol. Figures 3.25 and 3.26 verified the findings in [62] that the TAL is indeed a nonlinear component of TGF loop. The figures show that a pure sinusoidal forcing in the TAL inflow gets distorted beyond amplitude and phase changes into an oscillatory concentration waveform at the outflow, whose main characteristic is the loss of slope symmetry. This makes the outflow concentration waveform nonsinusoidal. It is also clear that this nonlinear transformation is caused by the tubule as a whole, so that as the cells dilute the tubular fluid the nonlinearities arising from the transit time dependency accumulate during the fluid's trip from outer medullary to cortical regions of the TAL. When the TGF loop is closed, the nonlinearities are accentuated and the waveform is time shifted because of the delay elements of the TGF loop. Nevertheless, we noticed that the waveform transformation between luminal and cytosolic concentrations although nonlinear, results in cytosolic concentration waveforms that are similar to those in the lumen. This might not happen if we were to add nonlinear delay elements to signaling processes that mediate CVR and other transport pathways.

We also applied a broad-band forcing and computed the power spectral density functions (PSD) for different variables (Figures 3.27, 3.28, 3.29, 3.30). The spectra revealed that indeed the TAL behaves as a low-pass nonlinear filter with a harmonic structure that depends on location along the tubule, as well as on the solute under consideration. The

location dependency can be tied to transit time, while the solute dependency reflects the different transport pathways that the solute utilizes. As noted in Figures 3.18 and 3.19, an oscillatory flow with a component whose transit time is close to the steady-state transit time will either minimize or maximize solute concentrations excursions at different locations along the tubule. The optima of the excursions yield the nodes (minima) and antinodes (maxima) of standing waves established in the TAL. This implies, as found in [62, 42], that the harmonic structure of the TAL can be explained in terms of the transit time dependency of Na^+ transport. This principle, applied to our model, explains the location the optima in the power spectra calculated for our model. This also explains the changes in PSD as function of distance, since the transit time is a function of tubule length, –i.e., the distance between the entry of the TAL and a given location along the tubule. Now, inasmuch our model tracks different solutes, we were able to pick up differences in the power spectra of different solutes as well as relationships between them. From the PSD's associated with K^+ and NH_4^+ we can infer that the transport pathways affect the harmonic structure. We say this because the fundamental difference between solutes in our model resides in how they are conserved, i.e. how they are transported to/from the different compartments. This implies that the steady-state transit time as a determinant of net transport, is not uniform for all solutes.

The lack of extensive waveform distortion in the luminal-to-cytosolic (input to output) relation hinted at by Figures 3.25 and 3.26, and the opportunity given by our model formulation to explore the dynamics inside the cell, motivate us to study the cellular I/O relations depicted in Figure 3.31. Figure 3.31 can be interpreted as plots of gain factors as function

of frequency. By comparing with Figure 3.29, the first thing to notice is that the harmonic structure follows from that of the apical fluxes. What is remarkable is that for some solutes, the gain tends to be augmented in the OM to Cortex direction, with the notable exception of ammonium. Additionally, the gain values (given in dB) for Na^+ and Cl^- are negative, which implies, an attenuation of the I/O relation. This explains the small changes in cytosolic Na^+ and Cl^- that we saw for both high and low frequency forcing, and underlines the importance of internal regulatory mechanisms like CVR to maintain cell homeostasis. Given the changes in steady-state cell volume that we saw in Figure 3.14 when no CVR is in effect, it is straight-forward to conclude that not having a CVR mechanism will increase the gains of the I/O relations and, as consequence, larger swings in cytosolic concentrations and cell volume would be observed for oscillatory tubular inflows. This is potentially harmful for a cell, especially, if it involves big swings in pH.

The computation of the coherence function in Figure 3.32 revealed four things. First, that cells can be studied as idealized linear systems, defined by equating the output (cytosolic concentrations) to the convolution of input (luminal concentrations), and some impulse response function, for a large set of frequencies and forcing of the same amplitude (or less) of the one used in this work. This is true because the coherence is one or closer to one than to zero for most frequencies. But this was also surprising given the nonlinear and interdependent nature of solute transport across the epithelium. Recall that even electrodiffusive transport of a solute, besides being nonlinear, depends on membrane potential, which in turns depends on the transport of all other charged solutes. Second, drops in coherence at specific frequencies are caused, in part, by the TGF system. Third, there is solute variation

for the coherence function. Such variation is caused by the interdependency between solutes established by the different transport processes. And fourth, the high coherence also explains the lack of a dramatic nonlinear transformation between the luminal (input) and cytosolic (output) concentrations when an oscillatory flow is applied. This results points to the possibility recasting the cell model as an idealized linear system that captures the important features of the cell model used in this work, but without all the details.

Chapter 5

Perspective and further work

The thick ascending limb (TAL) is an archetypical physiological system in that its components, TAL cells, by individually regulating their internal composition and volume, adopt behaviors that organize the ensemble of cells in a way that yields efficient dilution of the tubular fluid, which is the primary function of the segment. This self-organizing behavior acts synergistically with the tubuloglomerular feedback (TGF) system, which controls TAL inflow rate such that the outflow fluid Cl^- concentration is low, but above the level at which the cortical TAL cells exhibit futile transport cycling. In this way, these systems ensure that the dilution of the tubular fluid is adequate to drive osmotic water reabsorption from the collecting ducts.

Short-term cell volume regulation (CVR) responses of individual cells along the TAL via reciprocal regulation of the NKCC2 and KCC4 transporters increases workload balance along the segment. Such workload distribution prevents the scenario where TAL cells in the

outer medulla (OM), a region of low O_2 availability, reabsorb the bulk of the NaCl, while cells in the cortex waste energy by continuing to pump against a limiting transepithelial gradient. Likewise, CVR responses help establish the axial Cl^- concentration gradient that is necessary for proper function of the TGF system. Changes in tubular inflow rate also have an impact in workload distribution. On one hand, an increase in inflow rate decreases the fluid's transit time along the tubule, which consequently balances the workload, but with the side-effect of increasing the outflow Cl^- concentration. On the other hand, a decrease in inflow rate has the opposite effect. Together, the CVR responses and the regulation of TAL flow by TGF result in a quasi-uniform distribution of NaCl transport and an axial [Cl] gradient sufficiently steep to yield a TGF system gain consistent with experimental data. This suggests that TGF is a self-optimizing feedback system, in that it drives the TAL towards a state that ensures a high feedback gain. This is an intriguing hypothesis that merits further study.

The idea that the TAL dilutes the tubular fluid in a highly efficient fashion because of K^+ cycling between the luminal and cytosolic compartments (uptake by NKCC2 and leakage via membrane channels) is at best a gross oversimplification and, at worst, utterly wrong. The efficiency index, defined as the ratio of total epithelial to transcellular Na^+ transport, never gets close to its upper bound. The efficiency reaches its maximum just before the cortico-medullary junction and then decreases and to its lowest point at the end of the tubule (late cortex) as the transepithelial concentration gradient increases owing to tubular fluid dilution. In other words, the positive transepithelial electric potential that is indeed established by K^+ cycling is not strong enough to counteract the transepithelial chemical

gradient built by tubular dilution that favors Na^+ backleak into the lumen. Therefore, if the TAL were to carry out the dilution of the tubular fluid efficiently, it cannot be explained by K^+ cycling alone. Also, the presence of NH_4^+ has to be taken into account. Ammonium cycling between the luminal and cytosolic compartment (uptake via NKCC2 and extrusion by NHE3), not only prevents K^+ depletion from the lumen and diminishes changes in cytosolic pH, but also makes the NHE another important pathway for Na^+ uptake. This phenomenon adds a layer of complexity because it potentially ties together cell volume regulation, pH regulation, and tubular fluid dilution. In this regard, a natural extension of our model is to include representation of the regulation of the NHE transport by cell volume. Another would be to include in each cell a submodel of ATP production and usage, and linking this to both the phosphorylation of the NKCC and KCC transporters, and Na^+-K^+-ATPase activity. This would add more layers of complexity but might result in more even tighter regulation of TAL cell transport.

Another natural extension is to embed the current segment model into a model of the outer medulla. Such a model would include collecting ducts, a descending limb, capillary blood flow, and an interstitium whose composition is determined by the balance of solute and water reabsorption from all of the structures. Although this would be a big undertaking, the model would permit more direct study of the interaction between blood flow, oxygen availability, and TAL function.

The dynamic features of the TAL-TGF system loop has an impact in workload distribution and efficiency of transport. The oscillatory behavior of the TGF system uncovers a complex but tractable set of dynamic properties for the TAL. Indeed, the TAL segment as

a whole behaves as a nonlinear low-pass filter with an harmonic structure defined by the solute's transit time along the segment. Subtle differences in the harmonic structure for each solute reveals that the impact of transit time is somewhat solute dependent. The main distinction between solutes in our model arise from the way they are transported. The influence is strong for solutes that are subjected to net reabsorption, like sodium and chloride, but less so for solutes that cycle or are secreted, like K^+ and NH_4^+. Therefore, although the general principle can be applied to explain key aspects of the the dynamics of the TAL, subtle variation is expected owing to the intrinsic complexity of TAL transepithelial transport.

As mentioned above, the TAL behaves like a nonlinear low-pass filter, in that the effect of flow oscillations on the Cl^- concentration of the outflow is attenuated as frequency increases. The nonlinear distortion of an oscillatory luminal concentration profile is accumulative in space, which means that as a wave travels along the length of the tubule, that wave is gradually distorted as solute is transported by the cells lining the tubule walls. Also, regardless of the oscillatory forcing in the luminal compartment, the cytosolic concentrations exhibit oscillation of lesser magnitude, which is a reflection of the action of regulatory mechanisms in the cells to stabilize their internal environment.

The coherence function of the ratio of luminal to cytosolic concentration, which can be interpreted as an input to output ratio is closer to one for most frequencies, even though the transcellular transport processes are nonlinear and interdependent. This permit us to study the cells as idealized linear input/output systems. Moreover, this yields the possibility of using an idealized linear system as approximation to a cell model in a multinephron model

of the kidney.

The creation of the cell-based or multiscale model of the TAL presented here involved many choices about the level of detail that needed to be included. Our approach has been to begin with a minimal model, but even this, yielded a complicated model with complex behavior. In the end, the configuration chosen proved to be adequate for the goals of this study. Still, the model can be made more realistic without sacrificing tractability. Small changes like a nonuniform tubule radius or a volume dependent NHE can be implemented without much effort, and may add some insight to the dynamic and the efficiency aspects of the TAL. On the other hand, not so small changes like including detailed signaling schemes for CVR, and representation of oxygen delivery via vasa recta and ATP production and consumption could keep me busy for years.

Bibliography

[1] P. Guo, A.M. Weinstein, and S. Weinbaun. A hydrodynamic mechanosensory hypothesis for brush border microvilli. *Am. J. Physiol. Renal Physiol.*, 279:F698–F712, 2000.

[2] A.M. Weinstein. Glomerulotubular balance in a mathematical model of the proximal nephron. *Am. J. Physiol.*, 258:F612–F626, 1990.

[3] H. Chang and T. Fujita. A numerical model of the renal distal tubule. *Am. J. Physiol.*, 276:F931–F951, 1999.

[4] H. Chang and T. Fujita. A numerical model of acid-base transport in the rat distal tubule. *Am. J. Physiol. Renal Physiol.*, 281:F222–F243, 2000.

[5] A.M. Weinstein. A mathematical model of rat distal convoluted tubule. i. contransporter functions in early dct. *Am. J. Physiol. Renal Physiol.*, 289:F699–F720, 2005.

[6] A.M. Weinstein. A mathematical model of rat distal convoluted tubule. ii. potassium secretion along the connecting segment. *Am. J. Physiol. Renal Physiol.*, 289:F721–F741, 2005.

[7] P.L. Fernandes and H.G. Ferreira. A mathematical model of rabbit cortical thick ascending limb of the henle's loop. *Biochim. Biophys. Acta*, 1064:111–123, 1991.

[8] R. Greger and E. Schlatter. Properties of the basolateral membrane of the cortical thick ascending limb of henle's loop of the rabbit kidney. *Pflugers Archive*, 396:325–334, 1983.

[9] H.E. Layton, E.B. Pitman, and L. C. Moore. Bifurcation analysis of tgf-mediated oscillations in sngfr. *Am. J. Physiol. (Renal Fluid Electrolyte Physiol)*, 261:F904–F919, 1991.

[10] A.M. Weinstein and T. A. Krahn. A mathematical model of rat distal ascending henle limb. ii. epithelialfunction. *Am. J. Physiol. Renal Physiol.*, 298:F525–F542, 2010.

[11] A.M. Weinstein. A mathematical model of rat distal ascending henle limb. iii. tubular function. *Am. J. Physiol. Renal Physiol.*, 298:F543–F556, 2010.

[12] M. Naesens, P. Steels, R. Verberckmoes, Y. Vanrenterghem, and D. Kuypers D. Bartter's and gitelman's syndromes: from gene to clinic. *Nephron Physiol*, 96(3):65–78, 2004.

[13] J.P. Briggs and J. Schnermann. The tubuloglomerular feedback mechanism: functional and biochemical aspects. *Annu. Rev. Physiol.*, 49:251–273, 1987.

[14] D. Casellas and L.C. Moore. Autoregulation and tubuloglomerular feedback in juxtamedullary glomerular arterioles. *Am. J. Physiol.*, 258:F660–F669, 1990.

[15] D. Sun. Mediation of tubuloglomerular feedback by adenosine: evidence from mice lacking adenosine 1 receptors. *Proc. Natl. Acad. Sci. U S A*, 98:9983–9988, 2001.

[16] J. Green. Acute renal failure; clinical and pathophysiologic aspects. In *The Kidney: Physiology and Pathophysiology*, volume 98, pages 2329–2373. Lippincott Williams & Wilkins, Philadelphia, USA, 2000.

[17] H.E. Layton, E.B. Pitman, and L.C. Moore. Instantaneous and steady-state gains in the tubuloglomerular feedback system. *Am. J. Physiol.*, 268:F163–F174, 1995.

[18] W.F. Boron and E. L. Boulpaep. *Medical Physiology*. Saunders, New York, USA, first edition, 2003.

[19] D. Kikeri, A. Sun, M. L. Zeidel, and S. C. Hebert. Cell membranes impermeable to nh3. *Nature*, 339:478–480, 1989.

[20] D. Kikeri, A. Sun, M. L. Zeidel, and S. C. Hebert. Cellular ammonium/potassium transport pathways in mouse medullary thick limb of henle. *Journal of General Physiology*, 99:435–461, 1992.

[21] B.A. Watts and D.W. Good. Effects of ammonium on the intracellular ph in rat mtal: mechanisms of apical membrane ammonium transport. *J. Gen. Physiol.*, 103:917–936, 1994.

[22] J. L. Kinsella and P.S. Aronson. Interaction of ammonium abd lithium with renal microvillus membrane na-h exchanger. *Am. J. Physiol. (Cell Physiol.)*, 241:C220–C226, 1981.

[23] A.M. Weinstein. A kinetically defined na+/h+ antiporter within a mathematical model of the rat proximal tubule. *J. Gen. Physiol.*, 105:617–641, 1995.

[24] J.P. Briggs, J. Schnermann, and G. Schubert. In situ studies of the distal convoluted tubule inthe rat. i. evidence for nacl secretion. *Am. J. Physiol. (Renal Fluid Electrolyte Physiol.)*, 243:F160–F166, 1982.

[25] J. Schnermann, B. Steipe, and J.P. Briggs. In situ studies of distal convoluted tubule in rat. ii. k secretion. *Am. J. Physiol. 252 (Renal Fluid Electrolyte Physiol.)*, 252:F970–F976, 1987.

[26] V. Vallon, H. Osswald, R.C. Blantz, and S. Thomson. Potential role for luminal potassium in tubuloglomerular feedback. *JASN*, 8:1831–37, 1997.

[27] K.T. Kahle, I. Gimenez, H. Hassan, F.H. Wilson, R.D. Wong, B. Forbush, P.S. Aronson, and Lifton. Wnk4 regulates apical and basolateral cl- flux in extrarenal epithelia. *P NAS*, 101:2064–2069, 2004.

[28] K.T. Kahle, J. Rinehart, A. Ring, I. Gimenez, G. Gamba, S.C. Hebert, and R. P. Lifton. Wnk protein kinases modulate cellular cl- flux by altering the phosphorylation state of the na-k-cl and k-cl cotransporters. *Physiology (Bethesda)*, 21:326–335, 2006.

[29] J. Rinehart and et al. Wnk3 kinase is a positive regulator of nkcc2 and ncc, renal cation-cl- cotransporters required for normal blood pressure homeostasis. *Proc. Natl. Acad. Sci. USA*, 102:16777–16782, 2005.

[30] I. Giménez, P. Isenring, and B. Forbush. Spatially distributed alternative splice variants of the renal na-k-clcotransporter exhibit dramatically different affinities for the transported ions. *J. Biol. Chem.*, 277:8767–8770, 2002.

[31] C. Plata and et al. Functional properties of the apical na+-k+-2cl- cotransporter isoforms. *J. Biol. Chem.*, 277:11004–11012, 2002.

[32] D.B. Mount and et al. Isoforms of the na-k-2cl cotransporter in murine tal i. molecular characterization and intrarenal localization. *Am. J. Physiol.*, 276:F347–358, 1999.

[33] C. Plata and et al. Isoforms of the na-k-2cl cotransporter in murine tal ii. functional characterization and activation by camp. *Am. J. Physiol.*, 276:F359–F366, 1999.

[34] C. Plata and et al. Alternatively spliced isoform of apical na-k-cl cotransporter gene encodes a furosemide-sensitive nacl cotransporter. *Am. J. Physiol. Renal Physiol.*, 280:F574–F582, 2001.

[35] H.E. Layton. Mathematical models of the mammalian urine concentrating mechanism. In H.E. Layton and A.M. Weinstein, editors, *Membrane Transport and Renal Physiology*, pages 233–272. Springer, New York USA, 2002.

[36] R. Latta, C. Clausen, and L. C. Moore. General method for the derivation and numerical solution of epithelial transport models. *J. Membrane Biol.*, 82:67–82, 1984.

[37] M. Marcano, H. Yang, A. Nieves-Gonzalez, C. Clausen, and L.C. Moore. Parameter estimation for mathematical models of nkcc2 cotransporter isoforms. *Am. J. Physiol*, 296:F369–F381, 2009.

[38] M. Marcano, H. Yang, A. Nieves-Gonzalez, M.A. Nadal, C. Clausen, and L.C. Moore. Parameter estimation for models of ammonium transport by the renal na-k-2cl and k-cl cotransporters. Submitted for publication to Am. J. Physiol, 2010.

[39] A. Mercado, L. Song, N. Vazquez, D.B. Mount, and G. Gamba. Functional comparison of k+-cl- cotransporters kcc1 and kcc4. *J. Biol. Chem.*, 277:11004–11012, 2002.

[40] H. Chang and T. Fujita. A numerical model of acid-base transport in rat distal tubule. *Am. J. Physiol. Renal*, 281:F222–F243, 2001.

[41] C.H. Luo and Y. Rudy. A dynamic model of the cardiac ventricular action potential. i. simulations of ionic currents and concentration changes. *Circ Res*, 74:1071–1096, 1994.

[42] H.E. Layton, E.B. Pitman, and L.C. Moore. Spectral properties of tubuloglomerular feedback system. *Am. J. Physiol. Renal Physiol*, 273:F635–F649, 1997.

[43] R.J. LeVeque and H.C. Yee. A study of numerical methods for hyperbolic conservation laws with stiff source terms. *Journal of Computational Physics*, 86:187–210, 1990.

[44] J.W. Thomas. *Numerical Partial Differential Equations: Finite Difference Methods*. Springer, New York, USA, first edition, 1995.

[45] A.V. Wouwer, Ph. Saucez, and W.E. Schiesser. Introduction to the method of lines. In A.V. Wouwer, Ph. Saucez, and W.E. Schiesser, editors, *Adaptive Method of Lines*, pages 10–14. Chapman & Hall, New York, USA, first edition, 2001.

[46] M.A. Knepper, R.A. Danielson, G.M. Saidel, and R.S. Post. Quantitative analysis of renal medullary anatomy in rats and rabbits. *Kidney International*, 12:313–323, 1977.

[47] B.C. Kone, K.M. Madsen, and C.C. Tisher. Ultrastructure of the thick ascending limb of henle in the rat kidney. *Am. J. Anatomy*, 171:217–226, 1984.

[48] L.C Moore, J. Schnermann, and S. Yarimizu. Feedback mediation of sngfr autoregulation in hydropenic and doca- and salt-loaded rats. *Am. J. Physiol. (Renal Fluid Electrolyte Physiol.)*, 237:F63–F74, 1979.

[49] C. de Rouffignac and J.P. Bonlavet. Variations in glomerular filtration rate of single superficial and deep nephrons under various conditions of sodium intake in the rat. *Pflugers Archive*, 317:141–156, 1970.

[50] W.M. Haynes, editor. *Handbook of chemistry and physics*. CRC, New York, USA, 91st edition, 2010.

[51] T.D. DuBose Jr., L.R. Pucacco, M.S.Lucci, and N.W.Carter. Micropuncture determination of ph, pco2, and total co2 concentration in accessible structures of the rat renal cortex. *J. Clin. Invest.*, 64:476–482, 1979.

[52] R. Greger. Ion transport mechanisms in thick ascending limb of henle's loop of mammalian nephron. *Physiol. Rev.*, 65:760–797, 1985.

[53] R. Greger and E. Schlatter. Properties of the lumen membrane of the cortical thick ascending limb of henle's loop of the rabbit kidney. *Pflugers Archive*, 396:315–324, 1983.

[54] J. Schnermann and J. Briggs. Function of the juxtaglomerular apparatus: local control of glomerular hemodynamics. In D.W. Seldin and G. Giebish, editors, *The Kidney: Physiology and Pathology*, pages 669–697. Raven, New York USA, 1985.

[55] R. Greger, E. Schlatter, and F. Lang. Evidence of electroneutral sodium chloride cotransport in the cortical thick ascending limb of henle's loop of rabbit kidney. *Pflugers Archive*, 396:308–314, 1983.

[56] P. Komlosi, A. Fintha, and P. Bell. Unraveling the relationship between macula densa cell volume and luminal solute concentration/osmolality. *Kidney Int.*, 70:865–871, 2006.

[57] J.E. Dennis and R.B. Schnabel. *Numerical Methods for Unconstrained Optimization and Nonlinear Equations*. Prentice-Hall, New Jersey, USA, 1983.

[58] E.B. Pitman and H.E. Layton. Tubuloglomerular feedback in a dynamic nephron. *Communications in Pure and Applied Mathematics*, 42:759–787, 1989.

[59] L.C. Moore and J. Mason. Perturbation analysis of tubuloglomerular feedback in hydropenic and hemorrhaged rats. *Am. J. Physiol. (Renal Fluid Electrolyte Physiol.)*, 245:F554–F563, 1983.

[60] N.-H. Holstein-Rathlou. A closed-loop analysis of the tubuloglomerular feedback mechanism. *Am. J. Physiol. (Renal Fluid Electrolyte Physiol.)*, 245:F554–F563, 1991.

[61] S.C. Thomson and R.C. Blantz. Homeostatic efficiency of tubuloglomerular feedback in hydropenia, euvolemia, and acute volume expansion. *Am. J. Physiol. (Renal Fluid Electrolyte Physiol.)*, 264:F554–F563, 1993.

[62] H.E. Layton, E.B. Pitman, and L.C. Moore. Nonlinear filter properties of the thick ascending limb. *Am. J. Physiol. Renal Physiol*, 273:F625–634, 1997.

[63] N.H. Holstein-Rathlou and D.J. Marsh. Oscillations in tubular pressure, flow, and distal chloride concentration. *Am. J. Physiol. (Renal Fluid Electrolyte Physiol.)*, 256:F1007–F1014, 1989.

[64] A.T. Layton, L.C. Moore, and H.E. Layton. Multistability in tubuloglomerular feedback and spectral complexity in spontaneously hypertensive rats. *Am. J. Physiol. Renal Physiol*, 291:79–97, 2005.

[65] J.S. Bendat and A.G. Piersol. *Random Data: Analysis and Measurements Procedures*. Wiley-Interscience, New York, USA, second edition, 1986.

[66] W. H. Press, B.P. Flannery, S.A. Teukolsky, and W. T. Vetterling. Fourier transform spectral methods. In W. H. Press, B.P. Flannery, S.A. Teukolsky, and W. T. Vetterling, editors, *Numerical Recepies: The Art of Scientific Computing*. Cambridge University Press, New York, USA, first edition, 1986.

[67] A.M. Weinstein. A mathematical model of rat distal ascending henle limb. i. contransporter function. *Am. J. Physiol. Renal Physiol.*, 298:F512–F524, 2010.

Appendix A

Carrier mediated transport

A.1 NKCC2 and KCC4

Here we show the kinetic model for the Na^+-K^+/NH_4^+-$2Cl^-$ (NKCC2) cotransporter, and for the K^+/NH_4^+-Cl^- (KCC4) cotransporter. In both cases from the kinetic model we apply mass action to derive a system of ordinary differential equations (ODE), but since translocation is faster than binding we can assume the ODE system is in steady-state. This lead us to linear system of equations in the enzymatic densities (E_i's) that we solve to then compute the fluxes for each solute. Figures A.1 and A.2 depict the kinetic models for the NKCC2 and KCC4 cotransporters.

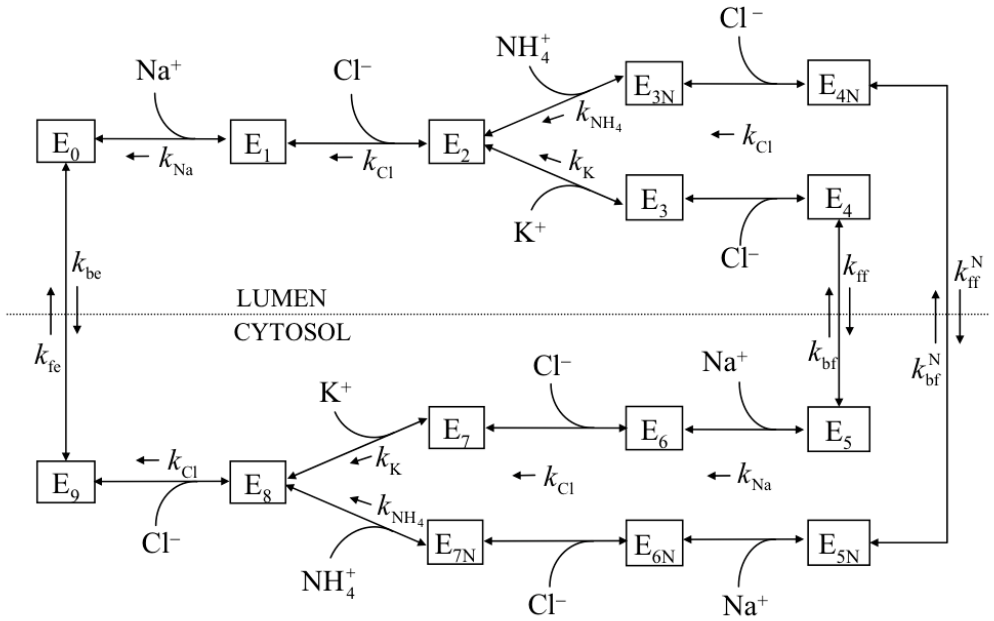

Figure A.1: Kinetic model for the NKCC2 cotransporter.

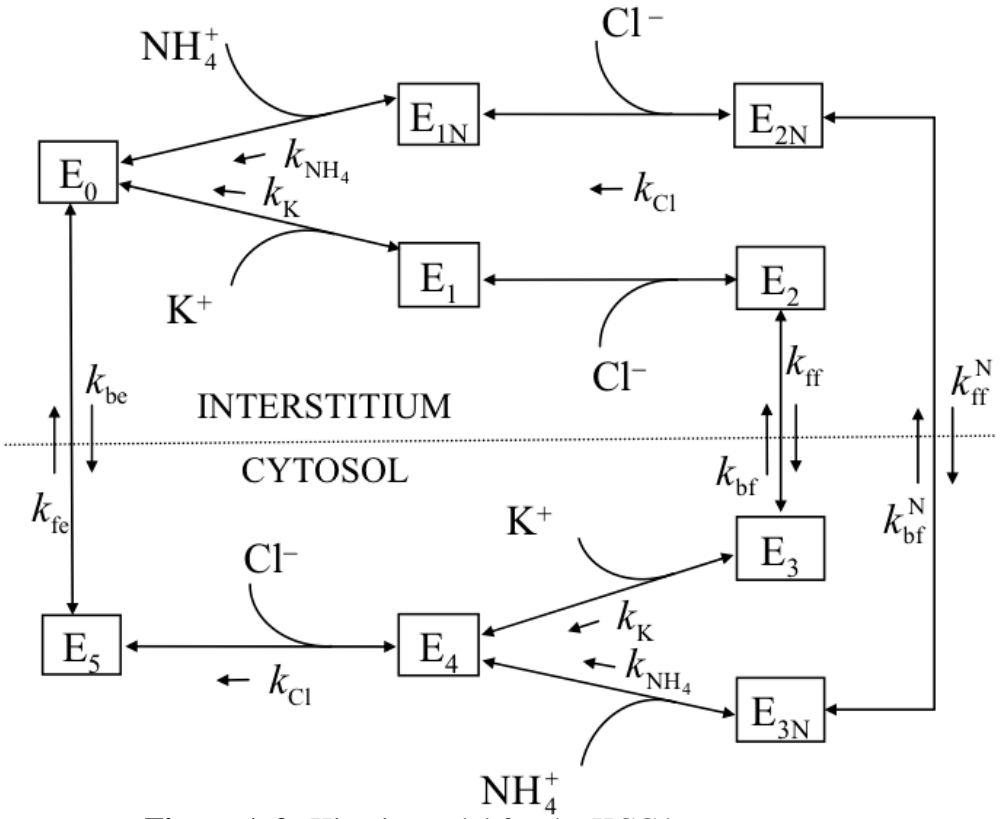

Figure A.2: Kinetic model for the KCC4 cotransporter.

A.2 Na^+-K^+-ATPase

The formulation for the Na^+-K^+-ATPase that we used in this work was that of Luo and Rudy [41], a formulation that depends on the basolateral membrane potential. But a noteworthy addition was also made. Similar to what Weinstein did in [10], we added a pathway for NH_4^+ through the pump. In terms of the implementation the addition can be summarized as follows:

- Use Lou and Rudy's Na^+-K^+ pump to compute the total current through the pump I.
- Compute the Na^+ and the combined K^+ and NH_4^+ flux using the well-known stoichiometry 3:2, hence $J_{Na^+} = 3I/F$ and $J_{K^+-NH_4^+} = -2I/F$ where F is Faraday's constant and

  $$J_{K^+-NH_4^+} = J_{K^+} + J_{NH_4^+}$$

  is the combined ammonium and potassium flux.
- Use the ratio of equilibrium constants $r = K_{K^+}/K_{NH_4^+} = 0.2$ (from [10]) and set $r = J_{K^+}/J_{NH_4^+}$. Therefore K^+ and NH_4^+ fluxes are,

  $$J_{K^+} = \frac{J_{K^+-NH_4^+}}{(1+r)} \quad \text{and} \quad J_{NH_4^+} = J_{K^+-NH_4^+} - J_{K^+}.$$

Appendix B

Cell model's Jacobian Matrix

B.1 Jacobian matrix of the right-hand side of the cell model

Solving for the steady-state of the TAL model involves either solving a system of differential-algebraic equations (DAE) in the case of the full segmental model or a non-linear system of equations in the case of the cell model. In any case, the algebraic part of the DAE as well as the nonlinear system of equations is the same system, that is, the right-hand side of equations (2.3)-(2.4).

Let $\mathbf{F}$ be the right-hand-side of the TAL cell model, i.e. equations (2.3)-(2.4), assume that luminal and serosal concentrations are fixed for the kth cell (infinite bath assumption), and define $\mathbf{y} = (y_1, \ldots, y_n, y_{n+1})^T = (\mathbf{C}_k^c, V_k)^T$ and $\mathbf{y}^*$ as a solution of

$$\mathbf{F}(\mathbf{y}) = 0.$$

The Jacobian matrix of f is defined as:

$$J_{\mathbf{F}}(\mathbf{y}) = \left[\frac{\partial F_i}{\partial y_j}\right].$$

Now, consider the column of $J_{\mathbf{F}}(\mathbf{y})$ that takes the derivative with respect of volume ($y_{n+1} = V_k$), that is

$$\frac{\partial F_i}{\partial y_{n+1}} = \begin{cases} -y_{n+1}^{-2}\left(-(A^a J_i^a(\mathbf{y}) + A^b J_i^b(\mathbf{y})) - y_i F_{n+1}(bfy)\right) - y_{n+1}^{-1}\frac{\partial}{\partial y_{n+1}}(A^a J_i^a(\mathbf{y}) + A^b J_i^b(\mathbf{y})) \\ \qquad\qquad \text{if} \quad i = 1, \ldots, n \\ 0 \quad \text{if} \quad i = n+1 \end{cases}$$

$$\Rightarrow \left.\frac{\partial F_i}{\partial y_{n+1}}\right|_{\mathbf{y}=\mathbf{y}^*} = \begin{cases} -y_{n+1}^{-1}\frac{\partial}{\partial y_{n+1}}(A^a J_i^a(\mathbf{y}) + A^b J_i^b(\mathbf{y})) & \text{if} \quad i = 1, \ldots, n \\ 0 & \text{if} \quad i = n+1 \end{cases}$$

and if there is no dependency of the solute fluxes on the volume variable y_{n+1}, that is, if there is not any sort of volume regulatory mechanism then we have

$$\left.\frac{\partial F_i}{\partial y_{n+1}}\right|_{\mathbf{y}=\mathbf{y}^*} = 0$$

Then, in the worst case we have a Jacobian matrix with a zero column and therefore singular, and in the best case a possibly ill-conditioned matrix if $-y_{n+1}^{-1}\frac{\partial}{\partial y_{n+1}}(A^a J_i^a(\mathbf{y}) + A^b J_i^b(\mathbf{y}))$ happens to be small in magnitude. In practice what is observed is an ill-conditioned Jacobian matrix. This presents a rather big problem to Newton's and secant-like methods, which are the standard way of solving nonlinear systems of equations, but presents an opportunity to apply derivative-free methods or try to reformulate the problem as a least squares problem. For DAE's, it is more difficult to work around the ill-conditioning.